Emil Rosqvist

Nanostructured Polymeric Surfaces for Biological Interfaces

Åbo Akademi University

Nanostructured polymeric surfaces for biological interfaces

Emil Rosqvist

Physical Chemistry
Laboratory of Molecular Science and Engineering
Faculty of Science and Engineering
Åbo Akademi University
Åbo, Finland, 2021

Supervised by

Professor Jouko Peltonen
Physical Chemistry
Molecular Science and Engineering
Åbo Akademi University, Åbo, Finland

Co-supervised by

Dr. Petri Ihalainen
Physical Chemistry
Molecular Science and Engineering
Åbo Akademi University, Åbo, Finland

Pre-examined by

Professor Per M. Claesson
Division of Surface Chemistry and Corrosion Science
Kungliga Tekniska Högskolan, Stockholm, Sweden

and

Professor Tapani Viitala
Division of Pharmaceutical Chemistry and Technology
University of Helsinki and Åbo Akademi University

Opponent

Professor Elena Martínez Fraiz
Department of Electronics and Biomedical Engineering
Universitat de Barcelona, Barcelona, Spain

ISBN 978-952-12-4122-2 (PRINT)
ISBN 978-952-12-4123-9 (PDF)
Painosalama Oy, Åbo, Finland, 2021

Table of contents

Abstract

In order to manufacture novel synthetic materials for use in biological applications, the continuous interactions over the materials interface must be thoroughly understood. It is difficult to develop all-encompassing descriptions of the multifaceted and dynamic character of these interactions and such conclusions elude scientists to date. Mammalian and bacterial cells react to physico-chemical properties of their surroundings. Such properties include a.o. surface energy, wetting, topography, and stiffness. Using materials with a controlled physico-chemical character, cells can be influenced through controlled interactions. Disparate responses driven by different materials have been observed — such as changes in adhesion, spreading, viability, morphology, division, and phenotype.

In this work different latex polymers were used to produce nanostructured surfaces with a controllable physico-chemical character, which was profoundly parameterised. The intent was to investigate how the character of the surfaces would influence *Staphylococcus aureus* bacterial biofilms as well as mammalian cells, specifically human dermal fibroblasts (HDF) and cervical cancer cells (HeLa). Cellular viability as well as the content and structure of the extracellular matrix or the biomatrix were used as measures of biological responsivity. In the bacterial studies, the responses of *S. aureus* to the surfaces were also compared in two different assays.

Surface properties, such as the peak and valley structures, influenced the viability of *S. aureus* and the polysaccharide contents of the bacterial biomatrix. Furthermore, these biofilms were influenced differently by the surface properties in the different assays. Another novel finding was that surface properties (and assay) can influence the *S. aureus* surface proteome. The amount of several virulence-associated proteins on the bacterial surface could for the first time be correlated with surface roughness parameters.

Mammalian HDF and HeLa cells responded differently to the surface nanotopography and surface chemistry. The viability of HeLa cells was influenced by e.g. the surface chemical character of the surfaces, but the viability of HDF cells was not influenced. An increasing amplitude of topographical peaks and valleys both increased the HDF viability, but the viability of HeLa cells was primarily benefited by a valley-dominated surface topography.

These surfaces were applied in an affordable, tailorable, paper-based planar diagnostics platform. The processability of the platform was demonstrated by using it both in a materials study and a drug screening study. In the studies, both the material and the drug were applied onto the platform with up-scalable methods. The analysis was done colorimetrically with an office scanner and a custom software. The results proved to be of comparable reliability with studies done in commercial well-plates and analysed with advanced plate readers.

This work shows that by using an extensive selection of surface parameters their individual influence on cells can be decoupled. Further, it shows that significant variations in different bioresponses can be observed when cells are grown on surfaces with nanoscale topographical differences. Such surfaces can be used to develop accessible, reliable and low-cost diagnostics platforms. The knowledge obtained can be used to develop novel materials for bio-applications, e.g. biomedical surfaces, where bacterial and cellular interactions with or via the material, e.g. fomite transmission, must be controlled.

Svensk sammanfattning

För att tillverka nya syntetiska material för användning i biologiska tillämpningar måste de evinnerliga interaktionerna över det biologisk-syntetiska gränssnittet förstås i grunden. Denna mångfacetterade och dynamiska samverkan gör detaljstudierna svåra att tillämpas i alla situationer, och allmänna slutledningar om samverkan mellan cell och material svåra att dra. Mammalie- och bakterieceller reagerar på omgivningens alla fysikalisk-kemiska egenskaper, så som ytenergi, vätning, topografi och styvhet, osv. Genom att tillverka material där dessa egenskaper justeras kan man kontrollera eller påverka celler. Mångskiftande materialdrivna responser har mätts hos celler — allt från ändringar i adhesion, spridning och viabilitet till morfologi-, förökning- och fenotypsförändringar.

I detta arbete har olika latexpolymerer använts för att tillverka nanostrukturerade ytor med intressant och kontrollerbar fysikalisk-kemiska karaktär, vilken parametriserades ingående. Målet var att undersöka hur variationer i ytornas fysikalisk-kemiska ytegenskaper påverkar *Staphylococcus aureus* biofilmer, mammalie- och bakterieceller, specifikt mänskliga hudfibroblastceller (HDF) och livmodercancerceller (HeLa) respektive. Som biologiska mått på cellernas respons användes viabilitet, samt den extracellulära matrisens eller biomatrisens struktur och innehåll. I bakteriestudierna jämfördes också *S. aureus*' responser till ytorna i två olika bakterieodlingsmetoder.

Ytegenskaper som t.ex. topp- och dalstrukturer påverkade *S. aureus*-biofilmernas viabilitet och biomatrisens polysackaridinnehåll. Den inverkan som ytegenskaperna hade på biofilmerna visades även variera beroende på odlingsmetod. En ny upptäckt var också att bakteriernas ytproteininnehåll påverkades av både ytegenskaper och odlingsmetod. Mängderna av flera av dessa virulensassocierade proteiner kunde för första gången korreleras med ytråhetsparametrar.

HDF- och HeLa-cellerna påverkades på sinsemellan olika sätt av ytornas nanotopografi och ytkemiska egenskaper. Exempelvis påverkades HeLa-cellernas viabilitet noterbart av ytornas kemiska karaktär, medan HDF-cellernas viabilitet påverkades ej. För de erhållna ytnanostrukturerna verkade HDF-cellerna gynnas av både dominerande topp- och dalstrukturer med högre amplitud. Dominerande dalar med ökande avstånd mellan ytstrukturer verkade däremot främst gynna HeLa-cellerna.

Dessa ytor tillämpades i en förmånlig och anpassningsbar planär pappersbaserad diagnostikplattform. Plattformens processerbarhet

demonstrerades genom att använda den i en materialstudie och en läkemedelsutvärderingsstudie. I bägge applicerades material och läkemedel i plattformen med metoder som lämpar sig för storskalig produktion. Analys skedde kolorimetriskt med en kontorsscanner och skräddarsydd mjukvara. När resultaten jämfördes med parallellstudier från en kommersiell plastbrunnsplatta som analyserats med konventionella, avancerade plattläsare visade sig resultaten ha jämförbar tillförlitlighet.

Detta arbete visar att ett omfattande urval ytparametrar kan användas för att frikoppla olika ytegenskapers påverkan på celler. Ytterligare visas att redan topografiska skillnader på nanoskala kan driva signifikanta variationer i olika bioresponser. Dessa ytor kan användas för mycket processerbara diagnostikplattformer, som trots enkla metoder kan ge tillförlitliga resultat. Resultaten från dessa studier kan utnyttjas för att utveckla nya material för biotillämpningar, t.ex. biomedicinska ytor där bakterie- och cellinteraktioner med eller via materialet måste kontrolleras.

Publications

Main publications

Paper I **Human dermal fibroblast proliferation controlled by surface roughness of two-component nanostructured latex polymer coatings**
E. Rosqvist, E. Niemelä, A. P. Venu, R. Kummala, P. Ihalainen, M. Toivakka, J. E. Eriksson, J. Peltonen
Colloids and Surfaces B: Biointerfaces, 2019, 17, 136–144

Paper II **Modulation of virulence factors of *Staphylococcus aureus* by nanostructured surfaces**
P. San-Martin-Galindo, E. Rosqvist, S. Tolvanen, I. Miettinen, K. Savijoki, T. Nyman, A. Fallarero, J. Peltonen
Materials & Design, 2021, 208, 109879

Paper III **A low-cost paper-based platform for fast and reliable screening of cellular interactions with materials**
E. Rosqvist, E. Niemelä, J. Frisk, H. Öblom, R. Koppolu, H. Abdelkader, D. Soto Véliz, M. Mennillo, A. P. Venu, P. Ihalainen, M. Aubert, N. Sandler, C.-E. Wilén, M. Toivakka, J. E. Eriksson, R. Österbacka, J. Peltonen
Journal of Materials Chemistry B, 2020, 8, 1146–1156

Authorship contribution statement

Paper I

The author was responsible for the conceptualisation of the study, its methodology, the formal analysis, investigation, data curation, visualisation, and writing (the original draft and the reviewing and editing process). **Niemelä and Venu**, under the supervision of **Prof. Eriksson**, performed the cell studies and cell imaging, the interpretation of these results. **Kummala**, under supervision of **Prof. Toivakka**, performed the force volume measurements of the surfaces. **Ihalainen and Prof. Peltonen** supervised the work and contributed to the conceptualisation and methodology. **Prof. Eriksson, Prof. Toivakka** and **Prof. Peltonen** were responsible for the funding acquisition for the study. All authors contributed to the manuscript reviewing and editing process.

Paper II

The author was responsible for the conceptualisation of the study, its methodology, the formal analysis, investigation, data curation, visualisation, and writing (the original draft and the reviewing and editing process)**. Paola San Martin Galindo**, contributed equally from a microbiological and proteomics point of view. **Tolvanen** contributed with methodology, in particular sample surface preparation and characterisation. **Miettinen** aided the proteomics analysis and data curation as well as microbiological data visualisation. **Savijoki** contributed to the protein extraction and identification. **Nyman** performed the protein identification in MS/MS and contributed to the proteomics data analysis. **Fallarero** and **Prof. Peltonen** supervised the work and helped to develop the research concepts and methodologies. All authors contributed to the manuscript reviewing and editing process.

Paper III **The author** was responsible for the conceptualisation of the study, its methodology, the formal analysis, investigation, data curation, visualisation, and writing (the original draft and the reviewing and editing process). **Niemelä** contributed equally from the perspective of cell biological methods. **Frisk** designed and developed the analysis software, **Öblom** was responsible for the drug printing, **Koppolu** performed the curtain coatings of polymers on paper, **Abdelkader** and **Venu** contributed to the cell studies, **Soto Véliz** performed the barrier coating tests, **Mennillo** synthesised the non-commercial latices. **Prof. Sandler, Prof. Wilén, Prof. Toivakka, Prof. Eriksson, Prof. Österbacka** and **Prof. Peltonen** stood for the funding acquisition for the study and supervised it. **Ihalainen, Prof. Eriksson, Prof. Österbacka** and **Prof. Peltonen** contributed to the development of methodologies and the conceptualisation of the study. All authors contributed to revising and editing the manuscript.

Supporting publications

S. Paper I **Protein and bacterial interactions with nanostructured polymer coatings**
H. Juvonen, T. Oja, A. Määttänen, J. Sarfraz, E. Rosqvist, T. A. Riihimäki, M. Toivakka, M. Kulomaa, P. Vuorela, A. Fallarero, J. Peltonen, P. Ihalainen
Colloids and Surfaces B: Biointerfaces, 2015, 136, 527–535

S. Paper II **Hierarchically structured self-supported latex films for flexible and semi-transparent electronics**
A. Määttänen, P. Ihalainen, B. Törngren, E. Rosqvist, M. Pesonen, J. Peltonen
Applied Surface Science, 2016, 364, 37–44

In these publications the author contributed to materials characterisation, sample preparation and manuscript revision and editing.

1. Introduction

The cell is a basic building block of life. In fact, bacteria, autonomously functional prokaryotic cells, were among the first living organisms on this planet ('prokaryotic' indicating them lacking a nucleus, contrary to the eukaryotic cells) [1]. Today bacteria can be found almost everywhere. Fortunately, they are mostly harmless, and some have even formed a mutualistic relationship with us humans. Unfortunately, some other bacteria are rather pathogenic and can cause infectious, potentially terminal, diseases. [2]. In these cases, the bacteria are transmitted from a reservoir, fomites (inanimate intermediate transmission points), animal carriers (in the case of zoonoses) or food to the host [2]. Bacterial infections are cured by bactericidal or bacteriostatic antibacterial pharmaceutics, the former outright killing the infecting bacteria and the latter merely inhibiting their reproduction [2]. A global healthcare issue is the ever-growing presence of bacterial strains resistant to available antibiotics. Novel antibiotic agents that can evade the resistance are thus highly sought for. One way to alleviate the situation could be to prevent infections where possible, by reducing cofactors (e.g., pollution), eliminating the source of infection, or by stopping the chain of transmission, for instance with antibacterial materials [2]. Such materials could be used e.g. in implant materials, medical surfaces or food packaging.

Eukaryotic cells are more advanced than bacteria. They sense and adapt to their surroundings, as well as communicate with each other, and ultimately form the functional, cooperative groups that are our living tissues and organs. A key component in this sensing and communication is the extracellular matrix (ECM), which is a complex arrangement of gathered and excreted biomolecules [3]. Through the ECM, biomechanical cues are transformed into biochemical signals and vice versa. These cues and signals stir the clockwork of the biological system into motion and regulates activities on the cellular and organ level — driving physiological functions and tissue regeneration. Injury or disease might disable or limit this function. In such a case benefits can be gained with the aid of biomaterials and -devices to support the regenerative process or bodily functions in lieu of a damaged organ [3].

Materials designed to interplay with bacterial and mammalian cells make use of the cellular nature to sense and react to their surroundings. This response has been observed to occur on the molecular level and it depends on the physico-chemical character of the surroundings of the cells, including material surface chemistry, topography and stiffness. Even singular functional groups in the material can influence the cells. As varied as the drivers of the biological responses are, so are the different responses. The material interface does not only influence the initial adhesion, but the complete cellular lifecycle, including reproduction and migration, and can even induce apoptosis.

Proteins are key players in the adsorption process of both microbial and mammalian cells. These macromolecules can facilitate transport in and out of the cells, drive changes, as well as transmit and transduce information, i.e., regulate. Proteins accumulate on the surface before the cells, and thus the cells encounter a protein-modified surface. The protein adsorption process is also dependent on the physico-chemical properties of the surface. In fact, the surface character and its heterogeneities can influence the amount and conformation of proteins being adsorbed onto the surface, as well as their activity, i.e., how their presence contributes to cell adsorption [4]. Protein adsorption is ultimately dependent on the physico-chemical properties of both the surface and the adsorbate proteins.

The large number of proteins together with specific characteristics of different cells has made wider and general conclusions elusive. Further, the response may vary between stages of cellular attachment, e.g., from initial cell adhesion to the stage where a biofilm (groups of bacteria that protect themselves and communicate with the ECM) or a confluent layer of cells (a complete monolayer of mammalian cells) has formed.

Decoupling the response at biological interfaces requires a set of materials with systematically varied and controlled surface character. Of utmost importance is the versatile description of the surfaces, since a detailed parametrisation of the system would enable universal comparisons between results from various studies [3].

2. The objectives of the work

In this work, a set of nanostructured polymeric surfaces was developed for use as a growth substrate for cells and bacteria, and their functionality as such was studied. In particular, the dependence of the biological response on surface topography and surface energy was studied. The work focused on the response of mammalian cells (specifically Human Dermal Fibroblast cells, HDF, and HeLa cervical cancer cells, HeLa) and bacterial biofilms (*Staphylococcus aureus*).

The main research objectives were the following:

- To regulate the biofunctionality of cells and microbial biofilms with surfaces with a controllable nanotopography.
- To decouple the influence of surface chemistry and surface roughness on the biological response.
- To use a detailed surface parametrisation for improving the understanding of cell-surface interactions.

HDF and HeLa cell viability as well as *S. aureus* biofilm formation, biofilm poly-N-acetylglucosamine abundance and surface proteome composition were correlated with surface properties of the growth substrate (Paper I, Paper II). The base substrate for the latex coatings in these studies was borosilicate glass coverslips.

In Paper III, the utility of the biofunctional films was demonstrated by deploying them in a sustainable paper-based screening platform, which was used for a basic cell study as well as for proof-of-concept drug screening. The used cell-lines were again HDF cells and HeLa cells. The model drug was the anti-cancer drug doxorubicin.

3. The conceptual background of adhesion

The adhesion of particle to a surface begins with it, the adsorbate, approaching the sorbate. As the adsorbate moves closer to the surface the interaction force increases, reflecting the chemical and physical character, such as surface energy and topography, of both the adsorbate and the surface. For particulate materials, the interactions have been described by theories such as the DLVO theory and the extended DLVO theory.

While much effort has been put into trying to model and control cell-material interactions, and much data has been obtained, a complete understanding of this complex process remains elusive [5]. Ironing out the physico-chemical mechanisms driving the relationship between surface character and biological response would be immensely valuable and would expedite the development of novel materials for a broad variety of applications such as implants, biosensors, protein fermentation, food packaging and cell-studies.

In this literature overview the use of physico-chemical theories for describing the foundations of adhesion and, finally, interactions between biological entities and surfaces are reviewed. Furthermore, the influence of surface properties, in particular surface chemistry and topography, on protein adsorption, microbial adhesion, and biofilm formation as well as mammalian cell responses to surfaces is discussed.

3.1 Surface topography

Ideal surfaces are homogeneous in all aspects, which for surface topography means perfectly flat. Real surfaces, however, always have some heterogeneity, regardless of the production technique [6]. Surface topography can affect adhesion, and it also influences the surface energy. These relations will be discussed separately later.

Surface topography affects the performance of the surface. For example, in tribology it relates to friction and wear, in printing it relates to ink setting and print quality, and in bioactive surfaces topography affects the interaction between the biological components and the surface. Topographical textures can be divided into form or lay, which are results of material processing, waviness and roughness, ordered from larger features to smaller [6]–[8]. Even surface flaws can be considered as a separate texture [6]. Form usually has little impact on wetting, while roughness can significantly alter it and is used as a driver for super-hydrophilicity and -hydrophobicity. The exact boundaries between form and roughness are not well defined. Especially from the perspective of tribology, waviness has been considered a feature caused by errors in processing and possibly the imaging technique, whereas roughness is a property of the material, which also can relate to manufacturing. How exactly waviness and roughness can be distinguished from each other is also up for discussion [6]–[8].

3.1.1 Measuring surface roughness

Typically, roughness is analysed by means of a profilometer. This can be a stylus instrument, to which scanning probe microscopes belong, or an optical instrument. Atomic force microscopy (AFM), a scanning probe microscope, is a focal point for this thesis in respect to surface imaging and roughness analysis. AFM is based on a pointed probe attached to a pliable cantilever, which is continuously probing the surface along a sweep line of a surface, while simultaneously recording its height position when in contact with the surface. A change in height position causes a change in the deflection of the cantilever, which is measured by monitoring changes in reflection of a laser beam from the cantilever with a photodiode (Figure 1). The instrument then adjusts the height position of the sample surface with the piezo unit of the scanner, so that the laser reflection becomes re-centred on the photodiode. A 3-dimensional image of the surface is obtained as the controller collects these height adjustments (z-direction) for each position in the xy-raster.

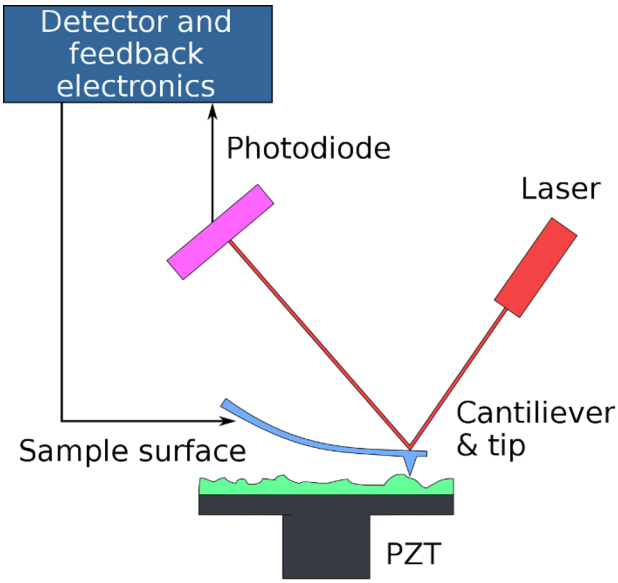

Figure 1 — A basic schematic of the AFM instrument, showing the laser being reflected from the cantilever to a photodiode. The signal is interpreted by the detector of the controller unit, which can adjust the sample position with the piezo of the scanner (PZT) as needed, based on the feedback. Figure from the public domain [9].

A captured image consists of discrete measurement points at intervals over the measurement length scale, the raster. Obviously, the raster size determines the image resolution [10]–[12]. The tip shape and size also affect the resolution (Figure 2) [13]. This is called tip convolution, which is especially influential when measuring high aspect ratio features [14]. Also, the instrument can poorly resolve cavities and overhangs of a surface (Figure 2B). The superimposed length scales of roughness that together form the topography of the surface can also cause a resolution dependence of some parameters [6]. As such, the length scale, the resolution, and the probe should be critically considered when comparing results from different sources.

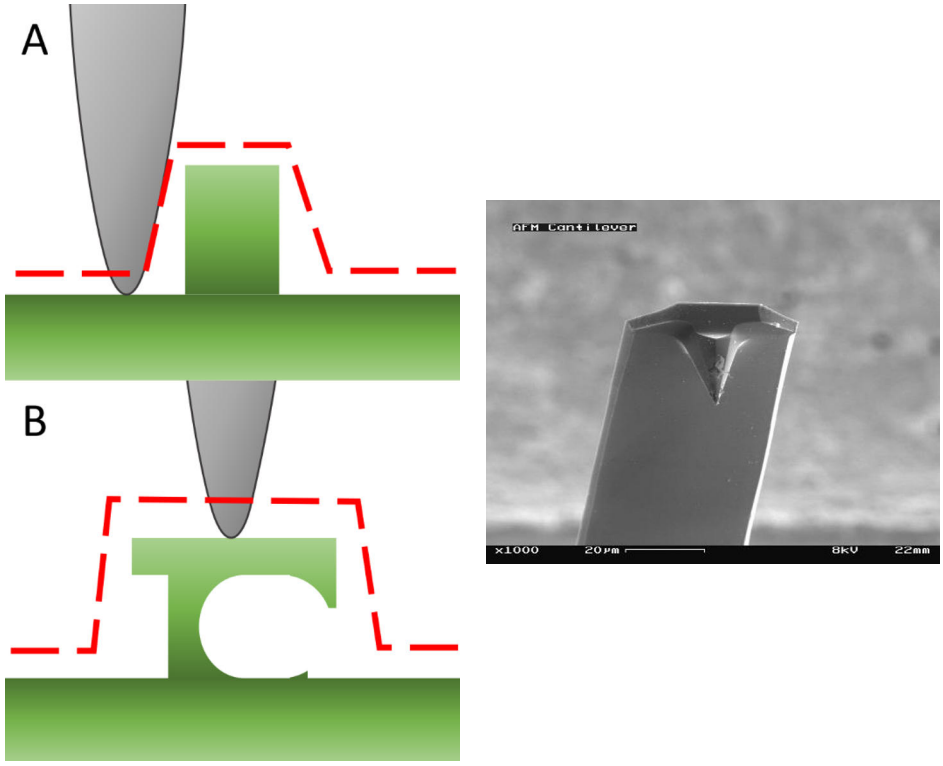

Figure 2 — (Right) A scanning electron microscope image of a typical, cylindrical, AFM tip in 1000x magnification, (CC BY-SA 3.0) [15], [16]. (Left) Illustration of how surface features (green) are misinterpreted (dashed line) relating to (A) the tip geometry and (B) surface overhang and cavities.

Despite these limits, AFM-based techniques provide a utility by not only imaging the topography but also being capable of measuring tip-surface interactions. The quintessential AFM mode images the surface by maintaining constant contact with the surface (contact mode). This is usually done at constant force, with the risk of deforming a sensitive or soft sample. In the intermittent-contact mode (colloquially 'tapping mode') the tip is oscillated at near-resonant frequency of the cantilever, and the tip 'taps' the surface once per oscillation cycle. This practically eliminates the lateral tip-sample interaction (friction) during the measurement, and more fragile samples can be imaged [17], [18]. In this case, also the phase angle of the oscillating cantilever interacting with the surface can be recorded, resulting in a phase-shift map, attributed to variations in tip-material interaction properties such as adhesion, stiffness and viscoelasticity [17].

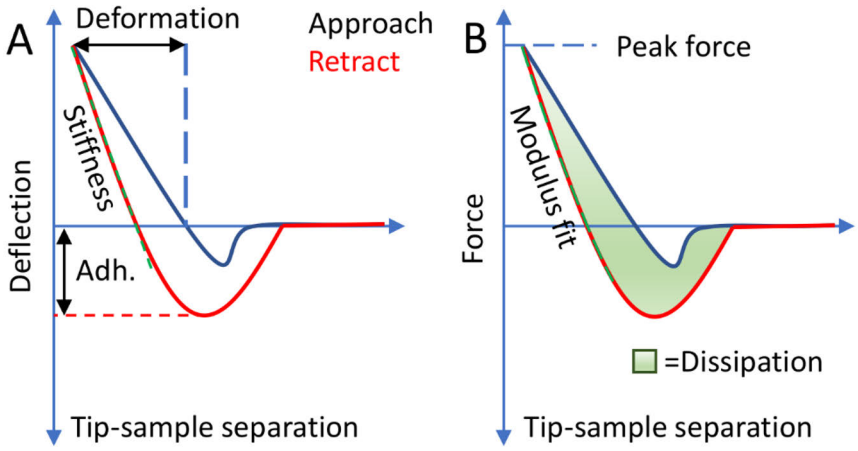

Figure 3 — Illustration of the force-separation plot and the material data that can be obtained from it, like the A. stiffness and adhesion as well as B. modulus and energy dissipation, the energy lost during the tip-sample interaction.

Investigating force-distance plots (Figure 3), which show the deflection of the tip as it is brought into contact with the sample and then retracted, can give more information about the surface. If the spring constant and deflection properties of the tip are known the stiffness of the sample (the slope of force-separation plot in the contact region) and the adhesion between sample and probe (maximum negative force during retraction) can be determined (Figure 3A). In case the contact geometry and elasticity are properly accounted for (see Section 3.5 for such models) even the elastic modulus can be obtained (Figure 3B) [19]. Current state-of-the-art operation modes utilise Peak Force QNM™ (Quantitative Nanomechanical Mapping) and can determine these parameters during imaging at high speeds [20]. Peak Force QNM™ can control the force down to a pN level, even in liquid [19]. The utility of the Peak Force QNM™ mode is well illustrated by its appearance in over 4000 peer-reviewed scientific publications during its first 10 years of use [21].

In addition to mechanical and rheological properties of a sample, also electrical and chemical properties can be investigated with the same instrument in a single or multiple pass. Examples include Kelvin probe force microscopy (KPFM) for surface potential [22] and conductive atomic force microscopy (C-AFM) [23], which provide useful tools for e.g. photovoltaics research. Recently AFM has been combined with high-resolution spectrometers and microscopes combining complementary techniques to serve scientific fields from palaeontology to molecular cell biology [24], [25].

3.1.2 Surface roughness parameters

Surface roughness is typically determined as height variations relative to a reference plane and is usually divided into groups of parameters that describe a similar character, like spatial or statistical distributions of data. These groups include height, hybrid, functional, and spatial parameters. Some also include functional volume parameters. Height parameters describe the height properties of a surface, such as the extreme heights and height distributions of it. Hybrid parameters describe the slope, curvature, and area of a surface. Functional parameters stem from the bearing area curve (also called the Firestone-Abbott curve). A general rule to consider when choosing parameters to describe any investigated surface is that parameters using mean values rather than extreme properties (i.e., maxima/minima) have the benefit of converging towards, rather than diverging from, a certain value and are therefore preferred as standard parameters for quality control [7].

Of the multifarious roughness parameters available some are commonly used while some are used more seldom. The parameters used and described in this thesis are chosen so that they provide a thorough description of the surfaces used. Next, these parameters are described group by group. Thorough mathematical descriptions can be found, for instance, through the International Organisation of Standardisation [26], in publications by e.g. Bhushan [6] and Whitehouse [7], as well as in analysis software manuals.

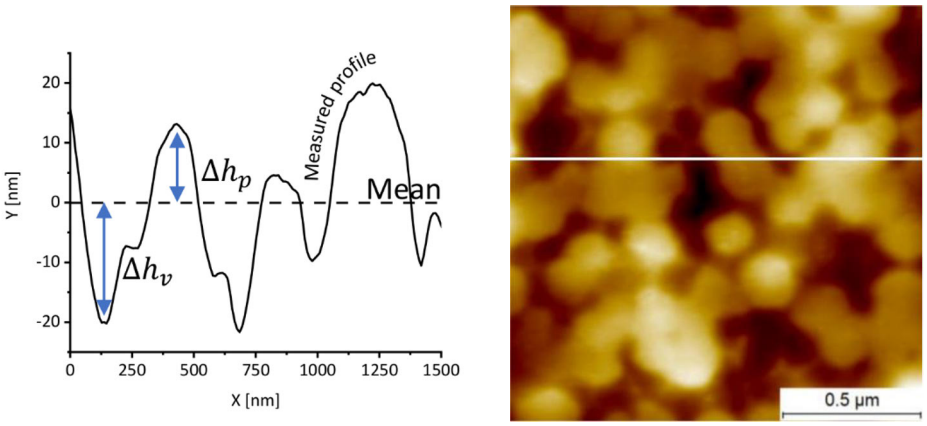

Figure 4 — An example line profile (left) from a 1.5 µm × 1.5 µm AFM topograph (right) of a latex surface. The profile position is marked in white. The height differences of two points — one in a valley, Δh_v, and one on a peak, Δh_p — to the mean height of the surface are marked in the profile.

The average roughness, S_a, is one of the most used roughness parameters. It describes the average (arithmetic mean) height variations of a surface to the mean height line (Figure 4). This parameter is often seen in definitions of

standards or in standard tests, such as roughness grading [6]. The root-mean-square roughness, S_q, is another very common roughness parameter that describes height. In essence this is the standard deviation of the height values from the mean level. This parameter is also occasionally used for normalising other parameters, such as S_{bi} (bearing area index) and S_q/S_{cl37} (see below). S_q is statistically more robust and reliable than S_a, but since S_a was more readily obtainable when surface metrological methods and standards were being developed it has established a firm place in surface characterisation [7]. Other common amplitude parameters are S_p and S_v, which describe the maximum peak height and valley depth of an image, determined relative to the mean line. Also the ten-point-height, S_{10z}, the average difference between the five highest peaks and five lowest valleys, can be used as a height parameter [7], [27].

Other height parameters are skewness, S_{sk}, and kurtosis, S_{ku}. These both relate to the distribution of heights. If skewness is 0, the distribution is symmetrical around the average height, like in the case of a Gaussian distribution. Values below 0 indicate a valley-dominated roughness, while values above 0 indicate a peak-dominated roughness. The kurtosis, in turn, describes the width of height distribution; a Gaussian distribution in this case has a value of 3 while broader and narrower distributions have smaller, or respectively larger S_{ku} values [7], [28]. This can be exemplified with AFM images of three different latex blends that were used in this study. Figure 5A shows a histogram of a bicomponent latex blend with 20% of polystyrene (PS) and 80% acrylonitrile butadiene styrene (ABS). This blend forms a rather smooth film with some peaks, measured over a range of 60.8 nm. This surface appears to be dominated by peaks arising from the high glass-transition temperature, T_g, PS particles sticking out of the mostly flat surface. This is supported by the value of S_{sk}, which is 0.31 for this surface. The distribution is almost Gaussian, as the S_{ku} is only slightly below 3 (2.9). A surface with more PS (40%) is shown in Figure 5D. There are more height variations on this surface, the height range being 107.6 nm, but from the image it is hard to evaluate if it is dominated by peaks or valleys. The S_{sk} parameter enables to define the surface as being slightly valley dominated with a negative S_{sk} -0.4. Even if the span of heights is higher, kurtosis is almost the same as for the 20% PS, being 3.0 — a quite Gaussian distribution. A final example is a 70% PS surface, which appears quite different (Figure 5E–F). This surface appears flat with valleys here and there, and the height span is wider. This surface is indeed much more dominated by valleys than the 40% PS, as can be seen also from the negative S_{sk} of -2.18. In this case the quite high kurtosis value, S_{ku}=10.3, shows that the height range is very wide. This is also clearly seen in the histogram image (Figure 5E). Hansson and Hansson have described how kurtosis and skewness can be used for the characterisation of biomaterials used in dental implants [29].

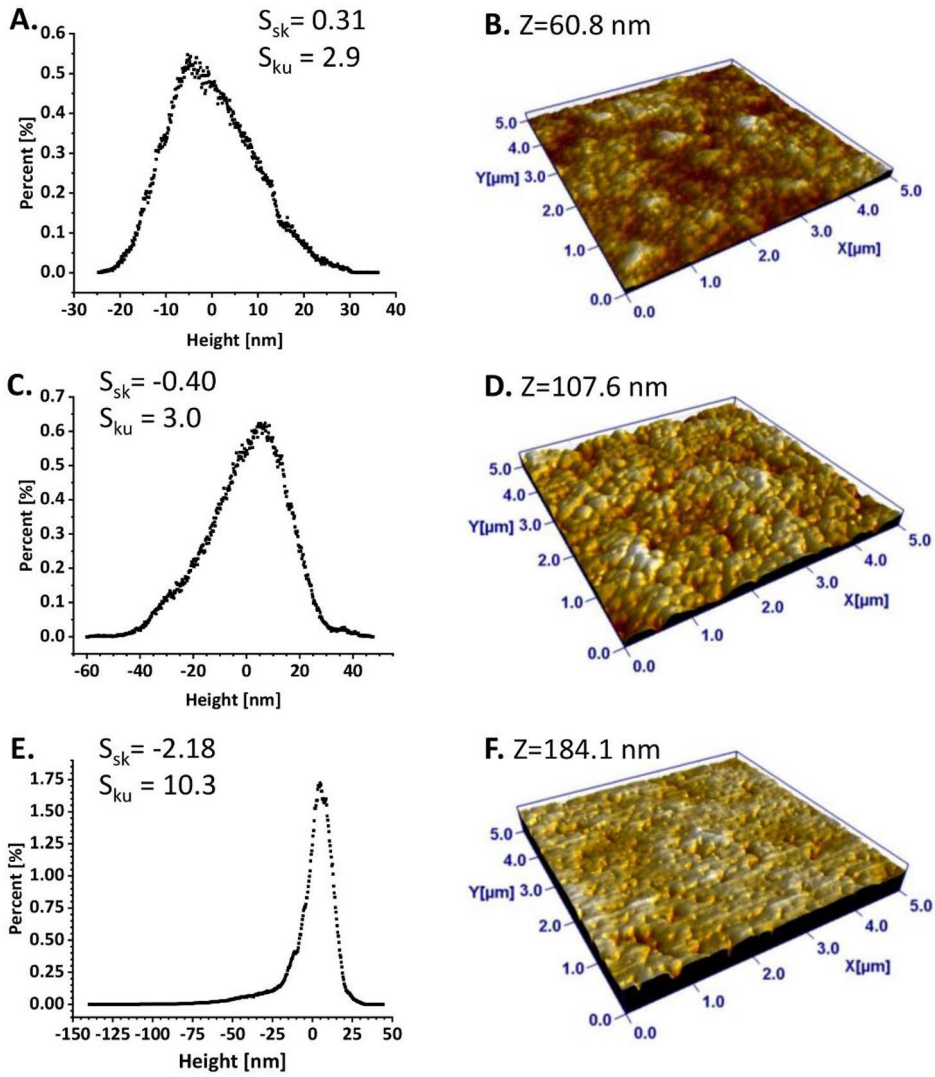

Figure 5 — An example of how skewness and kurtosis describe a surface's height distribution. Histograms (left column) corresponding to AFM topographs of three different bimodal latex blends (right column) with 20% PS (A. and B.), 40% PS (C. and D.) and 70% PS (E. and F.) and their corresponding skewness and kurtosis values. Images have a resolution of 512 by 512 pixels.

The use of the autocorrelation function (ACF), a spatial roughness parameter, and Fourier transformation have provided new means to investigate surfaces. The autocorrelation function relates to the probability with which two measurements of, e.g., height, self-correlate or how probable it is for the positions of two measurement points to deviate significantly from each other. For the purposes of these studies the autocorrelation length, assigned S_{cl37} or S_{al}, has been most thoroughly used. This describes the lateral distance for

which the areal autocorrelation function decays to a certain fraction of its original value, in the range 10–50 % [7]. In the studies in this thesis, this value was set to e^{-1}, i.e., 37%. The S_{al} parameter is a measure of the lateral distance at which two points are significantly different, but in some cases also as randomness of a surface [6]. The ACF relates to the randomness and isotropy of a surface. In biology, the ACF of a surface of a cell can also relate to its pathological processes [30]. Further, the normalised roughness, S_q/S_{cl37}, is the ratio of height to lateral roughness. This could be compared to the areal autocorrelation function, which normalises the ACF with S_q^2, the height variance.

In the group of hybrid parameters, the surface area ratio, S_{dr}, describes the relative increase in surface area caused by roughness compared to the area of an ideally smooth surface. A measure of the fine texture is the density of summits, S_{ds}, which measures the areal density of local maxima, which are points higher than their 8 neighbours. This relationship of this parameter with the density of peaks, S_{dp}, can be approximated as $S_{ds} = 1.2 \cdot \left(S_{dp}\right)^2$ [7]. The surface fractal dimension, S_{fd}, is a parameter determined from the Fourier amplitude spectrum of the surface. The fractal dimension for a direction is based on the slope of the logarithmic frequency and amplitude coordinate plot. In the SPIP software, which was used for roughness analysis, the value is determined as the average for all directions [28].

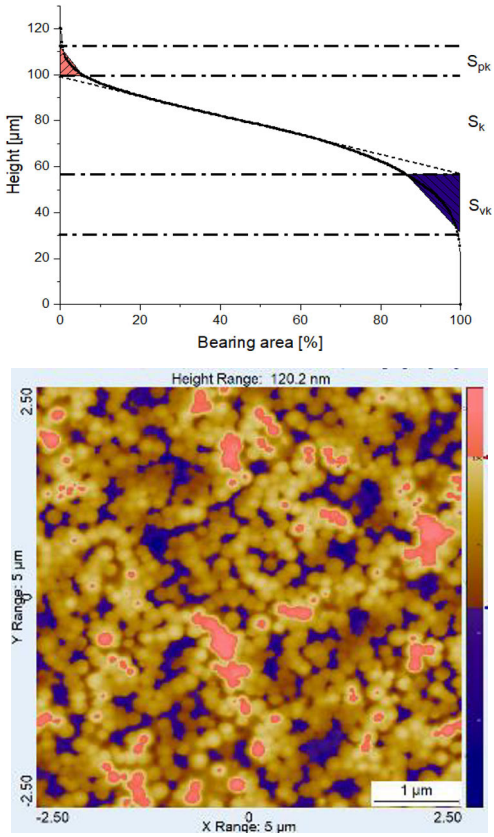

Figure 6 — (Top) The material ratio curve of an example latex surface obtained with AFM with corresponding S_k, S_{pk}, and S_{vk} levels (Bottom). The S_k (yellowish), S_{pk} (red) and S_{vk} (blue) height regions marked in the actual AFM topograph.

From the material ratio curve, also called the bearing ratio curve or Firestone-Abbott curve, several descriptive surface parameters can be obtained (Figure 6). The material ratio curve is a plot of the sum of the ratio of material intercept through a bearing plane, a plane parallel with the mean plane, determined at each height as it passes through a measured surface plot. This ratio is usually given as the material ratio at a certain height (Figure 6). From this plot three parameters relevant to this thesis are obtained: core roughness, S_k, reduced peak height, S_{pk}, and reduced valley depth, S_{vk}. They are determined as follows. The least mean squares (LMS) line is fitted to a 40% area of the curve so that the LMS line gets the lowest decline. When extrapolated to 0% and 100% material area ratios, and horizontal lines are drawn at both heights, the height difference between these two is the core roughness. If a further line is drawn from the horizontal line at the lower height, starting from the intersection point of the material ratio curve and the horizontal line, towards the 100% bearing ratio, so that the area of the formed

triangle is equal to the area between the horizontal line and the bearing area ratio curve, the height of this triangle is S_{vk}. A similar line is drawn to obtain S_{pk} as the height of the drawn triangle, when the line is starting from the upper horizontal line and forming a triangle with an area equal to that of the area of the bearing area curve above the horizontal line [8]. These parameters can be further normalised with each other to obtain parameters that describe the surface texture: S_{vk}/S_k, S_{pk}/S_k, and S_{vk}/S_{pk} [31].

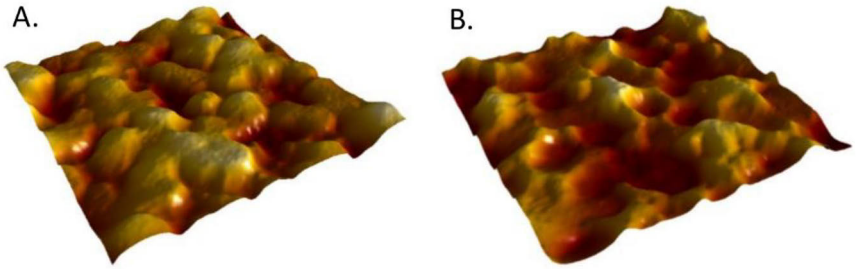

Figure 7 — A 3D render of the 1.5 µm × 1.5 µm image (height range 59.8 nm) shown in Figure 4 (A.) and its inverse (B.). Both surfaces have identical height variations from their means (S_a = 8.7 nm and S_q = 10.8 nm) and surface area (S_{dr} = 2.3%) even though they appear very different.

While a bland use of singular amplitude parameters is very common, they are not enough to describe a surface alone [6]. Only in the special case of a random and isotropic surface with a Gaussian distribution of heights two parameters are enough to statistically characterise it — a height distribution (which is described by, e.g., S_q) and the autocorrelation length, S_{al} [6]. Topographically very different surfaces can appear similar or even identical from the perspective of a certain parameter, which means that several different parameters should be combined to aptly describe a surface (see Figure 7). In practise this would mean not only using amplitude or 'height' parameters, but also hybrid (e.g., S_{dr} and S_{ds}) and functional parameters (e.g., S_{pk} and S_{vk}) [6], [8], [32]. In Figure 7 the surfaces could be distinguished using parameters reflecting their height distribution (e.g., S_{sk}) or the prevalence of peaks and valleys (e.g., S_p and S_v). Using a broad set of parameters not only allows researchers to get into more details in their analysis, but also allows for reuse of the data in advanced meta-studies, such as computer analysis of cell-surface interactions.

3.2 Surface energy

While the topography relates to the physical properties of a surface, the chemical character relates to its surface energy. This is another parameter relevant to material-material interactions.

The surface energy of a material, γ, can be considered the free energy excess of a surface compared to the free energy of the bulk, the change in free energy when transferring a unit of a material to the surface or the available free energy to create new bonds on the surface, or create a new surface altogether [33]. It is expressed in thermodynamic terms in relation to Gibbs free energy and the interfacial area as

$$\gamma = \left(\frac{\delta G}{\delta A}\right)_{\mathrm{T,\,P,\,N}}. \tag{1}$$

A surface with a low surface energy, and thus a low potential to create new bonds, is driven to limit its interaction with another material, such as a liquid, since there is little energetic benefit for forming new bonds with another material. Fowkes developed the concept by proposing that surface tension is a sum of all contributions of different intermolecular interactions, accounting for dispersive interaction forces (London forces), dipole-dipole interactions (Keesom), permanent-induced dipole interactions (Debye), hydrogen bonds etc. [34]. This led to the description of the interfacial interaction between two non-polar systems, γ_{12}, through mainly dispersive interactions as

$$\gamma_{12} = \gamma_1 + \gamma_2 - 2[\gamma_1^d \gamma_2^d]^{1/2}. \tag{2}$$

Here, γ_1 and γ_2 are the interfacial tensions of material 1 respectively material 2 and γ_1^d as well as γ_2^d denote the dispersive components of the interactions of the two materials. This equation was the result of interpreting the surface tension via a geometric mean of the two components, assuming similar contributions from both.

Van Oss, Chaudhury and Good suggested another approach to the surface energy. Their approach was to express it as contributions from Lifshitz-van der Waals interactions and acid-base interactions[35], [36]:

$$\gamma_{\mathrm{i}} = \gamma_i^{\mathrm{LW}} + \gamma_i^{\mathrm{AB}}. \tag{3}$$

The Lifshitz-van der Waals term, γ_i^{LW}, accounts for London, Keesom and Debye forces while the acid-base interactions, γ_i^{AB}, account for polar interactions including hydrogen bonding as well as donor-acceptor pair and electrophile-nucleophile interactions. The long range Lifshitz-van der Waals

forces are symmetric and additive, while the short-range components are not. The acid-base component was therefore expanded as

$$\gamma_i^{AB} = 2(\gamma_i^+ \gamma_i^-)^{1/2}, \quad (4)$$

thus separating the acid, γ_i^+, and base, γ_i^-, contributions, i.e. the polar negative and positive character of the surface energy [35]. These surface energy properties, the dispersive and both polar components, are those often considered in cell-surface interactions.

3.2.1 Wetting on ideal surfaces

The shape of a droplet wetting a surface and how it is defined by the corresponding surface energy components was a special case that was first described by Young [37]. The shape of a droplet can be described by the angle of the tangent of a droplet at its contact point with the solid plane and the vapour phase, i.e., at the three-phase contact line, under the assumption that it spreads evenly in all directions (Figure 8). This angle is the contact angle and measuring it is one of the most common approaches to determine the surface energy of materials [38].

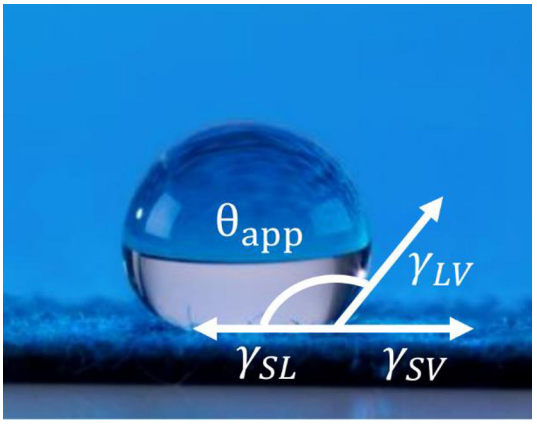

Figure 8 — The contact angle of a droplet on a surface is measured as the tangent of the droplets silhouette, measured at its contact point between the solid and the vapour phase. This represents a pseudo-equilibrium between the components of interfacial tension of each interface. Droplet photograph used with permission from the copyright holder, P2i Labs.

The contact angle is typically measured macroscopically, for instance using goniometry, which effectively measures the average contact angle, i.e., an average with respect to the chemical and topographical heterogeneities, of the

underlying surface. Different approaches for determining the contact angle are available, with static measurements of sessile droplets as well as dynamic measurements of advancing and receding contact angles being the two most common methods.

For an immobile droplet on a surface, three different contact angles have been described, according to definitions by Marmur [39]. These are θ_Y, Young's contact angle or the intrinsic contact angle for an ideally flat and chemically homogeneous surface, θ_{ac} the actual contact angle of the droplet on a real surface with some chemical heterogeneity and roughness, and θ_{app}, the apparent contact angle that is observed from measurements, which typically cannot account for small scale roughness. A droplet in equilibrium on a completely smooth surface has equal values for the actual and the apparent contact angles [40].

The apparent contact angle of a liquid is determined when the dynamic spreading of a droplet on the surface stops, and any detectable changes in droplet volume is due to liquid penetration or evaporation. This corresponds to a pseudo-equilibrium state [40], which represents an energy minimum concerning the interfacial tensions of the three-component system. The apparent contact angle that is measured is the angle between the tangent of the droplet front on the projected surface (Figure 8). In this case three components of interfacial tension act upon the system: that between the solid and the liquid droplet placed on the solid surface (γ_{SL}), that between the liquid droplet and the surrounding vapour (γ_{LV}) and that between the solid surface and the surrounding vapour (γ_{SV}). Young's equation for the intrinsic contact angle (also called the Young's contact angle) relates the contact angle to the components of interfacial tension [41]:

$$\cos\theta_Y = \frac{\gamma_{SV} - \gamma_{SL}}{\gamma_{LV}}. \tag{5}$$

In the case of an ideally smooth, inert, and chemically homogenous surface, the observed contact angle is also Young's contact angle. For any real surface, the observed apparent contact angle θ_{app} deviates from θ_Y because of roughness or chemical heterogeneity. Adding these factors to the equation, literally and proverbially, to relate to real surfaces makes matters slightly more complicated.

Depending on which form the droplet takes, surfaces are designated as being hydrophobic or hydrophilic, if the probe liquid is water. The prior refers to surfaces that are non-wetting, which have an equilibrium water contact angle θ_E larger than 90°, while partial wetting results in contact angles $90° \geq \theta_E > 0°$ [42]. Other definitions of hydrophilicity are also encountered in literature [43].

3.2.2 Wetting on real surfaces

The effect of surface topology on wetting has been described by Wenzel [44]. Wenzel related the θ_{app} and θ_Y with a roughness factor, r, which describes the increase in surface area due to surface roughness (Figure 9B). This roughness factor was defined as

$$r = \frac{actual\ surface\ area}{geometric\ surface\ area} \tag{6}$$

This way the θ_Y can be determined from θ_{app} as:

$$\mathrm{r}\cos\theta_Y = \cos\theta_{\mathrm{app}}. \tag{7}$$

The correction accounts for the roughness-increased contact area between the droplet and the surface. This, however, assumes a homogeneous wetting over the surface where the droplet completely fills any valleys of the investigated surface. The effect of roughness by the Wenzel equation emphasises the measured apparent hydrophilicity or hydrophobicity, with little effect on measured contact angles around 90°. A similar alternative form, based on the Young-Dupré equation has been suggested,

$$\left(1 + \cos\theta_{app}\right) = r(1 + \cos\theta_Y), \tag{8}$$

in order to account for this oddity [41].

A measure of the roughness factor r can be obtained by AFM through the roughness parameter $S_{dr,}$ [45].

$$r = (1 + \tfrac{S_{dr}}{100}). \tag{9}$$

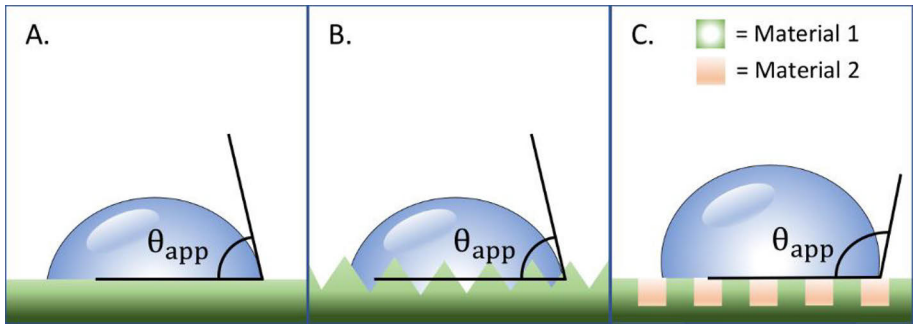

Figure 9 — The apparent contact angle of a droplet on A) an ideal surface, where $\theta_{app} = \theta_Y$, B) a topographically heterogenous surface, as described by Wenzel, and C) a chemically heterogenous, bicomponent surface, as described by Cassie.

Cassie developed a model describing wetting on chemically heterogeneous but perfectly smooth surfaces [46]. This accounts for several different wetting behaviours under the droplet, each with its own surface fraction, e.g., f_1 and f_2 for material 1 and 2, in the case of a bicomponent system, with corresponding individual contact angles (Figure 9C). The overall contact angle for the contact area of the droplet is then:

$$\cos\theta = f_1\cos\theta_1 + f_2\cos\theta_2 \tag{10}$$

If the physical heterogeneity results in chemical heterogeneity due to, e.g., microscopic air pockets, the situation is resolved by the Cassie-Baxter equation. This is a special case, which is important in superhydrophobic and superoleophobic phenomena and their applications [47].

Both Wenzel's and Cassie's equations, and their validity have been debated over the last decades, e.g. in [48]–[53]. A recent thermodynamic analysis by Shardt and Elliot, introduces a 'line-roughness Wenzel equation' as the most general form of the Wenzel equation. They also show that the original, areal-roughness Wenzel equation is a special case of the general equation [51].

3.2.3 Determining the surface energy of a surface

Several approaches to determine the surface energy of materials from contact angles have been developed since Young's essay. A critical discussion on the subject still rages on, in regard to both theoretical and practical approaches of the models connecting the theoretical surface energy character and measured contact angles [54]–[57]. One line of approach is based on the equation of state and is utilised by e.g., Kwok and Neumann [56]. Their method is one of

the few that has the benefit of being able to determine the surface energy using only one probe liquid. The multicomponent approach was developed from Fowkes' discussions (see Equation 2) by Owens and Wendt [58], and independently by Kaelble and Rabel [59], [60]. Combined with Young's equation this yields the OWRK method which relates the dispersive and polar properties of two liquids and the sample surface as

$$0.5\,\gamma_{LV}(\cos\theta_{SL}+1)=\left(\sqrt{\gamma_{SV}^{d}\gamma_{LV}^{d}}+\sqrt{\gamma_{SV}^{p}\gamma_{LV}^{p}}\right). \qquad (11)$$

This theory accounts for the contributions of different components as their geometric means. In a similar approach, Wu accounted for material interactions instead as their harmonic means [61], giving

$$0.25\,\gamma_{LV}(\cos\theta_{SL}+1)=\left(\frac{\gamma_{SV}^{d}\gamma_{LV}^{d}}{\gamma_{SV}^{d}+\gamma_{LV}^{d}}+\frac{\gamma_{SV}^{p}\gamma_{LV}^{p}}{\gamma_{SV}^{p}+\gamma_{LV}^{p}}\right). \qquad (12)$$

Wu noted that using the harmonic mean gave more reliable results than the geometric mean for materials with low surface energies, below approx. 30-40 mJ m^{-2} [62], [63]. With contact angles from two liquids — one polar, such as water, and one non-polar such as diiodomethane — the dispersive and polar surface energies of a solid can be determined using the OWRK and Wu method.

The polar, or acid-base, surface energy components were considered in the van Oss, Chaudhury's and Good's expansion of Fowkes' equation [35]. Combined with the Young's equation this resulted in

$$0.5\,\gamma_{LV}(\cos\theta_{SL}+1)=\left(\sqrt{\gamma_{SV}^{d}\gamma_{LV}^{d}}+\sqrt{\gamma_{SV}^{+}\gamma_{LV}^{-}}+\sqrt{\gamma_{SV}^{-}\gamma_{LV}^{+}}\right). \qquad (13)$$

With three unknowns, contact angles from three liquids are required to solve the equation for each surface energy component of the investigated surface.

Since these models are all pseudo-empirical and are still being critically discussed, it is exceptionally important to define what models have been used as well as the values for the surface tensions of the probe liquids that have been utilised in each study.

3.3 Particle-surface interactions

Many biological objects such as lipids, proteins, and nucleic acids can be considered as macromolecules. A convenient way to approach biological adhesion is therefore by approximating it as a particle adhering to a surface, even in the case of a cell.

A particle encountering a surface results in interactions that depend on the physico-chemical properties of the interacting objects. The type of interaction can be dispersive, polar (acid-base) and/or electrostatic [64], [65]. The surface topography of either entity also influences the interaction [66], [67]. One way to approach these interactions is through thermodynamics, but DLVO theory provides another perspective. Both can provide some insight into cell-surface interactions [64], [65], [68], [69].

A process is **thermodynamically** favourable if there is a net reduction in free energy. For an adhesion process where a particle, p, approaches a surface, s, when in a liquid media, l, the energy change can be expressed in terms of the interfacial energies of the components:

$$\Delta G_{adh} = \gamma_{PS} - \gamma_{PL} - \gamma_{SL}, \tag{14}$$

or, more generally,

$$\Delta \mathrm{G}_{adh} = \Delta G_{adh}^{LW} - \Delta G_{adh}^{AB}. \tag{15}$$

This approach allows for an estimation of the particle-surface interaction if the surface energies are obtainable. Determining the surface tension of the three components of the system — the growth medium, the surface and the biological particle — can indicate the basic thermodynamics of the adhesion mechanism between two equilibrium states.

Another model for interpreting and measuring interaction between entities is the **DLVO theory**, after Derjaugin, Landau, Verwey and Overbeek. This is the fundamental theory on which contemporary surface and colloid science stands [70]. The DLVO theory approaches the particle-surface interaction as the balance of the electrostatic double-layer and dispersive forces (Figure 10) [71], [72]. Dispersive and polar interactions were introduced briefly in the previous section, whereas the electrical double layer is elaborated in the following.

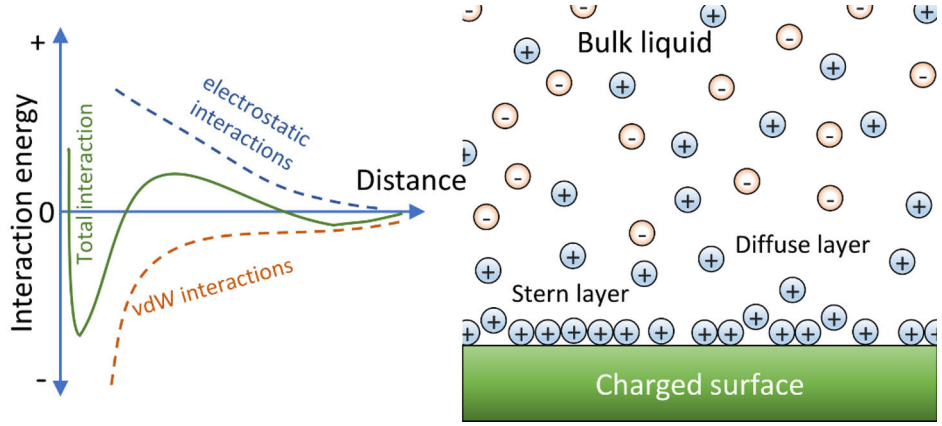

Figure 10 — (Left) Illustration of how the total interaction energy (green) changes with distance. Contributions come from the vdW interactions (orange, typically attractive) and electrostatic interactions (blue, typically repulsive). The result is often a primary minimum in proximity of a surface, and a secondary minimum at some short distance from the surface. These are separated by an energy barrier. Based on [73].

(Right) The electrical double layer is formed as a counterbalance to a charged surface. Ions of opposite charge (in this case positive ions to an apparently negative surface) organise at the interface (the Stern layer). As the closest layers counteract the surface potential, the interaction decreases rapidly with distance. The outer layer is a pseudo-organised "diffuse layer". Based on [74].

The electrical double layer (EDL) is formed at an interface in a polar medium, where a charge is built up on the surface (Figure 10). This can be due to ion adsorption or the ionization of a surface group. The overall effect is the alignment of counter ions near the interface according to the surface polarity. Since this is present on both a particle and the surface it approaches, their EDLs overlap and interact as electrostatic fields through interaction potentials. The strength of the EDL can be measured through the zeta potential, ζ, and it is dependent on different factors such as the valence and concentration of the counter ions, due to ionic shielding, etc. — the geometry of the interface not left unmentioned [71].

The DLVO theory can be condensed to a sum of the distance dependent interaction potentials [72],

$$G^{TOT}(d) = G^{LW}(d) + G^{EL}(d). \qquad (16)$$

In general, dispersive forces are attractive and electrostatic forces repulsive [71], [75]. For an interaction between a particle and a surface, descriptive of a (cellular or microbial) particle adhering to a surface, the following equations for $G^{LW}(d)$ respectively $G^{EL}(d)$ could be used [72]:

$$G^{LW(d)} = -\frac{A}{6}\left[\frac{a}{d} + \frac{a}{d+2a} + \ln\left(\frac{d}{d+2a}\right)\right] \quad (17)$$

and

$$G^{EL}(d) = \pi\epsilon a(\zeta_1^2 + \zeta_2^2)\left[\frac{2\zeta_1\zeta_2}{\zeta_1^{2'}+\zeta_2^2}\ln\frac{1+\exp(-\kappa d)}{1-\exp(-\kappa d)} + \ln\{1-\exp(-2\kappa d)\}\right]. \quad (18)$$

In Equation 17, a is the radius of the adherent particle that is assumed to be spherical, and the particle and the surface are separated by a distance d. The Hamaker constant, A, is a material constant that represents the van der Waals (vdW) interaction between two objects through a medium. The Hamaker constant has been related to surface energy and refraction index, which provide means to determine this character of a material [72], [76]. In Equation 18, the permittivity of the medium, ϵ, as well as the zeta potentials of the surface and particle, ζ_1 respectively ζ_2 are accounted for, as well as the "thickness" of the double layer, κ^{-1}, which is dependent on all the available ionic species in the medium — both their concentration and valency. The distance described by κ^{-1} is the distance over which the electrostatic interaction is reduced to 1/e [71].

The DLVO theory was extended (**xDLVO**) by van Oss, Chaudhury and Good who included some contributions, including acid-base interactions [36], [72]. While having a short range (<5nm) the acid-base interactions are strong compared to dispersive and electrostatic forces [72]. Since the Hamaker constant can be determined from the Lifshitz-van der Waals energy component, ΔG^{LW}, Equation 17, the xDLVO theory can be connected to both the thermodynamic and the DLVO description of particle-surface interactions.

The above models do not account for surface roughness of either the particle or the surface. This provides another parameter to consider. For an ideally smooth particle adhering to an ideal (smooth) surface the interaction between the two bodies is independent of the lateral position. The same is true for a rough particle adhering onto a smooth surface. In other cases, where the surface is rough and the particle may or may not be rough, the interactions are position dependent [67]. Some models account for physical heterogeneities. For instance, one approach using RMS roughness and distance between asperities instead of asperity radius, as done by Rumpf, was developed by Rabinovich from the Hamaker theory [67], [77]:

$$F_{Rabinovich} = \frac{AD}{12a^2}\left[\frac{1}{1+\left(\frac{16Dk_1RMS}{\lambda}\right)} + \frac{1}{1+\frac{k_1RMS}{a}}\right] \quad (19)$$

The adhesion force, F, has in this case contributions from RMS roughness, RMS, and an asperity distance, λ. $k_1$is a coefficient of proportionality relating the

maximum height and RMS roughness. These topographical properties could be compared to S_q and S_{cl37} or S_{ds} parameters. In another study, Götzinger and Peukert accounted for the heterogeneity of modelled Hamaker constants of the surfaces and asperity radii as being logarithmically normally distributed [67].

3.4 Other interaction models

Other numerical and analytical methods like surface element integration (SEI) and Derjaguin's integration have been used to incorporate topographical effects to surface-colloid interactions. These have found that textured surfaces have a lower interaction energy compared to smooth counterparts, possibly due to an increased distance to the core surface [78]. It was observed that asperity was the most influential parameter on total interaction energy for surfaces with pits, cylindrical and hemispherical pillars with diameters in the range 20–200 nm and feature heights of 20–150 nm at an aspect ratio of ca 1 [79].

In biological interactions both the surface and the particle, i.e. the cell (whether eukaryotic or prokaryotic), are rough. The features of the cell that confer the roughness are e.g. pili, in the case of bacteria, or focal adhesions, in the case of cells. In addition, they are also reactive. Further, the complex nature of physiological liquids, which can include thousands of different protein species at varying concentrations, makes the previously described interaction theories are more difficult to apply to biological interactions.

All interfacial phenomena are not covered by the DLVO theory. These include for instance hydration, hydrophobic and capillary forces etc. [80]. Further, when depicting adhesion of real particles, including biological, it might also be necessary to account for elasticity. In such cases any deformation will alter the interaction area. Such interactions are accounted for by theories such as JKR (Johnson, Kendall and Roberts), DMT (Derjaguin, Muller and Toporov) and others [67], [81]. Parsons et al. developed a model that distributed the non-contact DLVO force over a roughness profile based on the RMS roughness or the histogram of a surface. Roughness caused the short-range vdW forces to be amplified, and some mid-range repulsive regimes diminished [39].

4. Biological adhesion

In biological adhesion, adhesion of proteins onto the material surface occurs chronologically first, and subsequently microbial and/or mammalian cell adhesion takes place (Figure 11). Cells on the surface can adapt to the features of it and, if it is a suitable environment, proliferate or, on the contrary, decrease the cellular viability. In this chapter, the driving factors for cell-surface interactions are discussed, as well as the different ways cells can respond to different surfaces. Furthermore, the question is addressed regarding whether theoretical models of adhesion and colloidal interactions can be deployed with any success for these biological species.

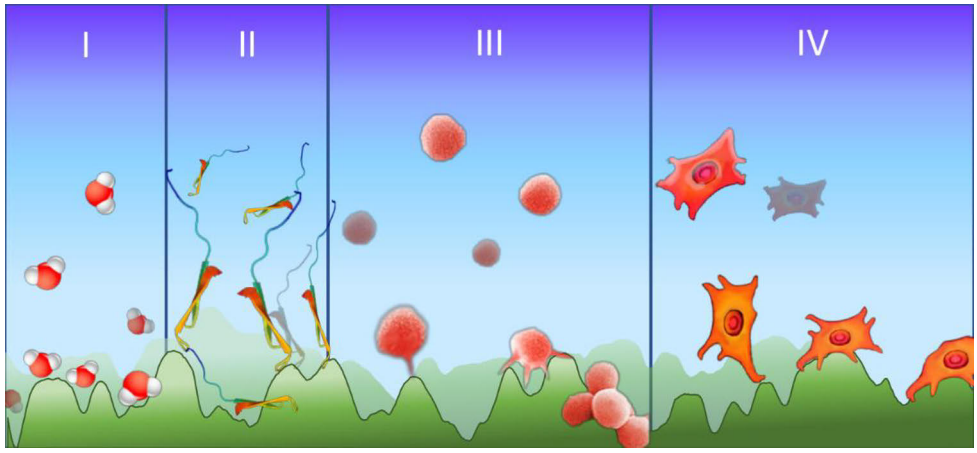

Figure 11 — Biological adhesion in four steps. When immersed in a biological solution a surface is immediately hydrated (I), in brief succession proteins adsorb onto the surface replacing the hydration layer (II). The microbes (III) and cells (IV) encounter a protein-conditioned surface.

4.1 Protein adsorption

Any material, synthetic or natural, placed in a biological environment faces an environment abounding with various proteins and other biomolecules. As different proteins reach the material surface they adsorb onto its hydrated surface within seconds, through physisorption, interactions being dominated by vdW forces, or chemisorption, which results in ionic or covalent bonds [82]. The adsorbed proteins can undergo conformational changes [83]. Thus, the interface that cells encounter is a protein-modified surface. These adsorbed proteins act as catalysts or mediators of the biological response to a material [43], [84].

However, since a myriad of different proteins are present in the biological media, predicting and controlling protein adsorption is all but simple. Such knowledge would be invaluable for manufacturing a tailored surface for controlled biomaterial adsorption. The low selectivity of adsorption, competing adsorption between protein components, conformational changes during the process and low adsorption energy further complicate the matter [5]. The literature even reports contradictory observations on e.g. reversibility, energetics and multilayer adsorption. This could be due to diverging opinions on the definition of adsorption — specifically the boundary between reversible and irreversible adsorption [43].

Both physical and chemical surface properties have been shown to affect protein adsorption (Figure 12). Roughness and hydrophobicity are two surface properties that have been connected to increased protein adsorption [43]. This can be explained by an adsorption-dehydration process. Adsorbing proteins must first dislodge the hydration layer bound with transitory hydrogen bonds, which requires energy. On a hydrophobic adsorbate surface the process results in a decrease of net free energy. To anionic and hydrophilic surfaces, especially with contact angles $\theta < 65°$, the hydrated layer has been reported to bind more strongly via hydrogen bonding. The net gain in free energy of the process thus decreases as the surface turns more hydrophilic, and proteins do not adsorb onto surfaces with $\theta < 65°$ [43].

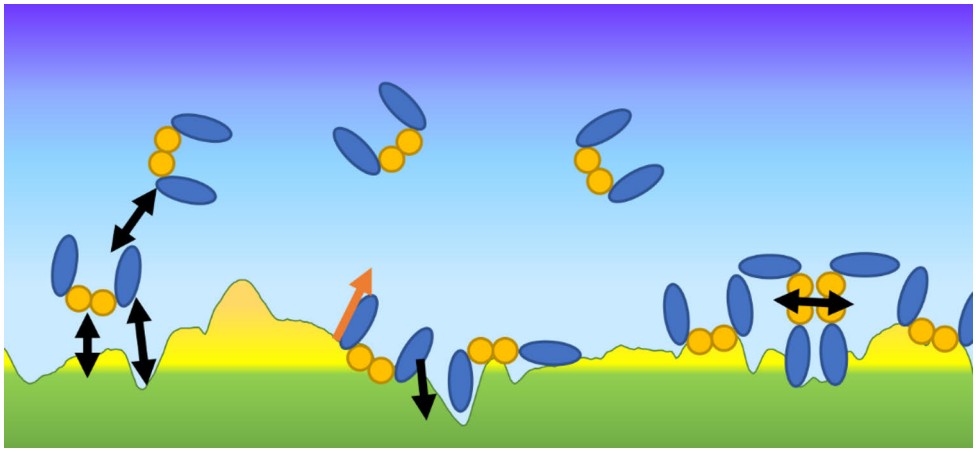

Figure 12 — Proteins are dynamically influenced by surface chemistry and topography as well as the presence of other proteins as they approach and adsorb to a surface (left). Having reached the surface, the protein might be driven to a reconfiguration due to the influence of the local interactions (centre). Previously adsorbed proteins might influence their neighbours (right). A physically heterogeneous (indicated by height variations in the image) or chemically heterogeneous surface (in this case a yellow coating deposited on the green substrate) can result in several different protein configurations.

Surface properties can also induce structural and conformational changes in the proteins, thereby influencing their activity [83]–[86] (Figure 12, centre). These are also dependent on protein properties, e.g., how prone they are to conformational changes. Further, a larger surface area has been connected to the amount of adsorbed proteins [83]. Some studies have shown that accounting for this surface character during quantification mitigates the observed effect [84]. However, surface chemistry can also influence for instance the occupied surface area, and thus the adsorption density [86]. This effect might be related to surface energy changes with roughness [84]. Protein-protein interactions can have a stabilising effect on protein layers, especially when these layers are thick [43] (Figure 12, right).

Adsorption of fibronectin and vitronectin is vital for migration and association of cells with the material surface of implant materials [84]. Polystyrene surfaces of cell culture plates may be chemically conditioned with sulfhydryl and polylysine to have improved protein interactions, and by extension, biocompatibility. On the other hand, pre-adsorbed avidin, a biotin binding protein, has been shown to inhibit bacterial adhesion through specific interactions [43], [87].

4.2 Microbial interactions with surfaces

Bacterial attachment and biofilm formation are of importance when understanding and counteracting bacterial fouling and infections, e.g., of implants, water purification membranes and food packaging. For bacteria, attaching or remaining motile is a strategic response to environmental conditions including surface properties, nutrient density etc. [88], [89]. While nutrient-poor conditions might favour energy-saving adhesion, attachment followed by biofilm formation increases the resistance of bacterial colonies to environmental stress, chemical disturbances and antimicrobial agents [89]–[91].

4.2.1 Microbial attachment

Approaching a surface that is hydrated and conditioned by tissue fluids, the bacteria can adopt different sensing mechanisms to detect beneficial areas to which to adhere (Figure 13 I–II). This sensing does not only occur in respect to surface properties, including their physical and chemical character such as surface charge, stiffness and topography, but also nutrients etc. [92], [93]. This might lead to an adaptation of the microbe itself (e.g. its surface charge), or to interactions with the surface other than adhesion (e.g. ion and/or molecule trapping) [78] (Figure 13 III–IV). Surface sensing may also trigger an upregulation of virulence factors [94].

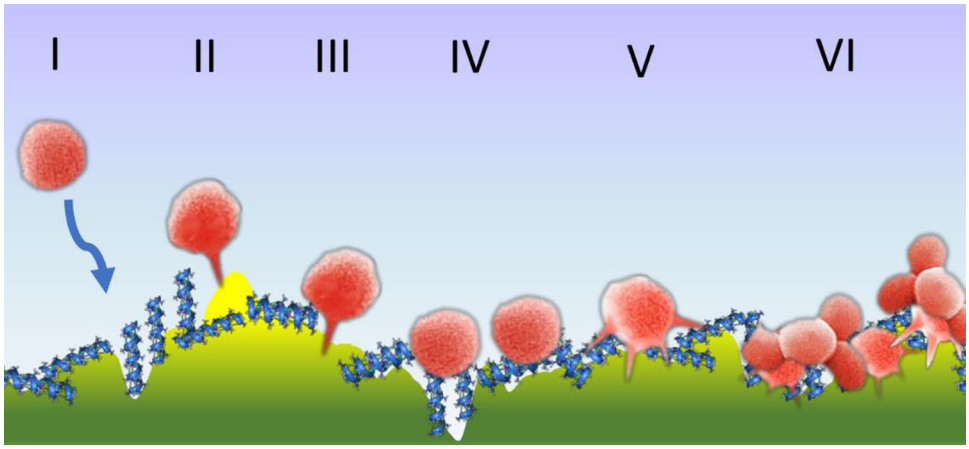

Figure 13 — Steps of microbial adhesion. The bacterium (red) first approaches and senses the surface to find beneficial sites of adhesion (I and II). This can lead to bacterial adaptation or molecule trapping (III and IV). The bacterium adheres by producing, a.o., polysaccharides and proteins which form the ECM and the biofilm matrix (V). As the bacteria gain numbers and associate themselves with a protective layer of PNAG, they can ultimately form a biofilm (VI).

The initial, reversible, attachment of microbes onto surfaces occurs on the scale of minutes while irreversible attachment occurs over hours. The reversible character is because of the overlap of the EDLs of the surface and the attaching microbe [95], [96]. Reversible adhesion becomes irreversible over time as the bacteria respond to being in proximity with the surface by producing nanofibrous structures, such as flagella, or excreting polysaccharides, proteins, extracellular DNA, a.o. (Figure 13 V). These are constituents of the biofilm matrix [72], [88], [89], [96]. A major component of this is the exopolysaccharide poly-N-acetyl-β-(1-6)-glucosamine (PNAG), a positively charged carbohydrate. Cell-cell adhesion is a factor that is enabled by PNAG, and this expression eventually leads to biofilm formation [91]. Finally, the bacteria adapt their shape to the surface, begin secreting extracellular matrix and associate themselves to form a biofilm [88], [89] (Figure 13 VI).

4.2.2 The biofilm

Biofilm formation is a dynamic process preferred by the bacteria which allow them tolerance to antibiotics, disinfectants and other environmental hazards. It can also enhance the invasion of the host immune system, therefore causing numerous chronic infections, the majority of which are associated with medical devices [97]–[99]. Due to its important role for keeping the integrity of bacterial biofilm, it is considered an attractive target for prevention of implant-based infections [100].

When a biofilm — a multi-cellular community — has formed, the bacteria may also specialise and show different motilities, susceptibilities to antimicrobial agents and adhesive behaviour. Intercellular communication in the biofilm is also complex, and bacteria adapt to different roles or move into different states in different regions of the community [91]. This contributes to the endurance of the biofilm, since some cells might be passivated, consume less and are thus less likely to encounter toxic substances [101]. The population near the biofilm surface is more likely to show so called swarming behaviour with morphological adaptations that enhance community growth and migration [89].

A drawback of adhesion is the inhibition of motility, partially due to phenotype changes, which renders the bacterium incapable of seeking out more favourable areas or additional nutrients [89]. In some cases, especially on surfaces that are beneficial for bacteria, bacteria are not attached directly onto the surface, but rather to a conditioning film of excreted exopolymeric character. Thus, a few adherent microbes can stimulate adhesion of others [72].

Proteins present in the bacteria matrix are essential in the numerous mechanisms in response to environmental determinants, and are thus also participating in the microbial attachment to surfaces [98]. Examples are cell wall-anchored proteins and proteins secreted to the extracellular milieu or retained in the membrane or cell wall. These are of special interest because of their role as virulence factors of *Staphylococcus aureus* infection [102].

4.2.3 Predicting microbial responses with physico-chemical theories

Different surface properties have been considered influential on microbial viability, and different physico-chemical theories have been applied to explain the adhesion process. As with proteins, these include mass transport theories for the initial transport of bacteria to the surface, thermodynamic analyses and DLVO theory. However, bacteria are such responsive and adaptive entities that an omnipotent theory or model has not been reached [64], [88].

Thermodynamic approaches have in a few cases proven adequate for predicting cell adhesion. Commonly, however, more intricate approaches have been found necessary, especially since any equilibrium state of the system might be hard to define [80]. The DLVO theory has also been used, not least because bacteria are near-colloidal in size and therefore allow the interpretation of the attaching microbe as a sphere approaching a surface. From the perspective of the DLVO theory, the situation where vdW forces are stronger than the electrostatic at long and short distances can be compared to reversible adhesion. A microbe is stable at the separation distance of the secondary minimum, and if it can penetrate through the energy barrier to the primary minimum, adhesion turns irreversible. A lower energy barrier and total interaction energy estimated by the DLVO theory have been connected to increased number of adhered cells [80]. Also, the xDLVO theory have been used with some success [78], [88]. In at least one case, the acid-base interaction was reported to improve the predictive power of the model for bacterial attachment [69]. It has also been observed that while a high adhesion force can be beneficial to the adhesion process it can also increase the cell stress and ultimately decrease viability [80]. Through these approaches one can obtain at least some rudimentary deposition kinetic models.

Since both the DLVO and xDLVO were developed for ideally smooth surfaces, roughness of both the surface and the bacteria, due to appendages of different size and shape, cause difficulties for this model, as does the biological responsiveness of bacteria. Further, the exact physico-chemical nature of pre-adsorbed layers is also difficult to evaluate [78], [88], [95], [103].

4.2.4 The influence of surface properties on bacterial adhesion and biofilm character

The complex interactions between surface, medium and bacteria during attachment has made it difficult to completely decouple the weight of singular properties. Most reports appear to contribute a significant role to material properties such as surface energy, wetting and topography. Further, the zeta potential of the surface could be an important parameter that controls the bacterial response [95], [104]. Material stiffness was recently reported as an additional contributor to the bacterial viability and adhesion [105]–[107]. Response differences between bacterial models, at least partly due to their morphological variations, also limit general observations [78]. This could be helped by a broader choice of materials in the investigations [78], [108]. Several later instances have highlighted a length-scale dependence of the response to roughness, especially where surface features are proportional to the size of the bacterium [78], [108].

Several issues are encountered when evaluating the influence of surface topography on bacterial interactions. The first obstacle comes from the nature of the surface structure, which can be ordered, random or even hierarchical — a feature that might be contributing to differences in, e.g., adhesion. Differences in roughness parameter values and length scales used, and a low number of parameters makes a proper comparison of results difficult, occasionally even impossible [32], [95]. Using computer-driven metadata analysis by compiling evidence from a large number of studies is a possibility if researchers provide a thorough description of the surfaces used. Singular observations on adhesion and viability could then be placed into the bigger picture.

The impact of roughness, specifically height variations, has been suggested to stem from that it decreases both the energy barrier and total interaction energy during microbial adhesion. Detailed observations are numerous and varied and focus on a broad range of functions from directing microbe attachment to directly influencing attachment. For instance, Truong et al. observed an increasing R_a, R_q, R_{sk} and R_{ku} (profile roughness parameters average roughness, RMS roughness, skewness and kurtosis determined from 10 μm images) to decrease attachment of *S. aureus*, *Pseudomonas aeruginosa* and *Escherichia coli* [109], [110]. The cells appeared to produce more extracellular polymeric substance on a smoother surface. Roughness has in some cases been reported to be only a minor factor after initial adhesion [72]. An example of cells being only slightly affected by topography has been reported; the attachment of *Streptococcus thermophilus* to stainless steel was observed to be unaffected by different roughnesses of a steel surface [111]. However, in other studies, bacteria have been observed to respond to surface variations over a broad size range — from the level of a few nanometers [108]

to larger features [112]. It has been observed that the correlation between surface roughness and adhesion is better when images of similar size as the bacteria were investigated [95]. Also, the relative size of features in the surface films could be influential [112], with sizes larger than the bacteria (*S. aureus* and *P. aeruginosa*) appearing to be preferential, indicating that bacteria eventually seek out grooves or pits, which possibly offer protection from hostile environments [32], [97], [113]. Tightly packed aluminium oxide surfaces with high aspect ratio pores (d≥50nm) have been observed to reduce attachment of some bacterial models including *E. coli* and *S. aureus* compared to flat surfaces. This effect was contributed to increased acid-base and electric double-layer interaction forces [78]. The effect of roughness on cells can also be different to that mediated by adsorbed proteins [84].

Surface chemistry has also been shown to be influential to bacterial adhesion. Of *S. aureus*, *Staphylococcus epidermis* RP62 and *Streptococcus mutans* only *S. aureus* was shown to have a high affinity for electron donor solvents in a MATS (microbial affinity to solvents) study [95]. MATS compares the affinity of bacteria to monopolar solvents of acid or base type to the bacterial affinity to polar solvents. All solvents should have a similar Lifshitz-van der Waals surface tension [114]. This indicates that *S. aureus* bacterial species might have stronger acid-base interactions than other model species. Lewis acid-base interactions have been considered negligible in several studies of microbial adhesion [95]. Alam and Balani noted surface energy, wetting and roughness to affect *S. aureus* adhesion, specifically a lower surface energy and a smoother surface causing less bacterial adhesion [115]. Bellon-Fontaine *et al.* found a connection between the dispersive component of the free energy and adhesion for *S. thermophilus B* and also *Leuconostoc mesenteroides* NCDO 523 [111].

4.3 Interactions of mammalian cells with surfaces

Microbial interactions with a surface are often desired to inhibit adhesion and growth, as is also the case for implant materials or food packings. The opposite is typically true for mammalian cell-surface interactions. In implants, dental or other, it is desirable that bone cells migrate to — possibly into — the surface matrix attaching the implant. Strong adhesion is then also beneficial [116], [117]. However, it is not necessarily desired to have all types of mammalian cells active and positively driven by a surface. Macrophages, cells that are key players in the inflammatory response, might be necessary to downregulate in order to improve healing and reduce rejection on long term [118]–[120]. These examples are only scraping the surface of what cellular responses the interaction with materials can drive within the cell. These include adhesion, differentiation, motility changes, proliferation and phenotype changes [3]. The biological mechanisms behind these responses are too complex to be discussed here in their entirety. However, an overview of mammalian cell-surface interactions, in particular adhesion and proliferation, is discussed.

4.3.1 Mammalian cell adhesion

In essence, cell adhesion is the stimulation of cell membrane receptors by an encountered interface which results in a chain of signalling events that results in adhesion [3]. Cellular adhesion is part of many cell functions *in vivo*. These include not only adhesion of a cell onto a material, e.g. for spreading and migration, and thus by extension tissue regeneration and wound healing, but also cellular interactions with the extracellular matrix (ECM) and intercellular communication. Essentially, cellular adhesion is formed and dispersed continuously as the cells interact with their surroundings [3], [121].

While the ECM acts as a mediator of mechanical and biochemical signals and cues for the cell, remodelling the ECM is possible. Such remodelling is one means through which cells communicate with each other [3], [84]. There are two common types of adhesion for cells — cell-cell and cell-ECM adhesion. Cells can also attach directly, non-specifically, to surfaces. This occurs in the case where no ECM proteins are present in the environment. These bonds are typically weak, both in a chemical and a biological sense, and if cells cannot deposit their own ECM to strengthen their attachment, they will eventually undergo apoptosis [122]. Adhesion mediated by ECM molecules also allows for cellular sensing and signalling. Such molecules are fibronectin, vitronectin, collagen and laminin, all of which can be found in cell media and body fluids. As such, these molecules form parts of the conditioning film in most experiments [122].

Focal adhesion is one common mechanism, with which cells contact a surface. In this, integrins are a major adhesion receptor component, along with vinculin, α-actin and several others. Focal adhesions have been associated with spreading and cellular motility [84], [121], [122]. As such they can represent an example of a connection between adhesion mechanisms, surface sensing and signalling mechanisms in the cell [121]. It is through these ECM-modulated interactions that the surface properties induce a response in the cells, or that the cells perform as a part of tissue [3].

4.3.2 Mammalian cell responses to surfaces properties

Through advanced analytical methods more clues have been obtained on how cellular activities are affected by biomaterials [3]. Understanding cellular cues and responses is the ground step in understanding not only materials interactions, but also the cellular clockwork, and is one step in between materials engineering and tissue engineering [123]. A complete understanding of the biochemical and biophysical responses on the cellular level would facilitate the development of biomaterial engineering. As in the case with microbial interactions, in spite of a long and arduous venture to understand the cellular interactions with surfaces, our understanding is incomplete and no model yet can provide an explanation to all observed mammalian cell-material interactions [3], [5], [124]. In this case as well, some surface parameters have repeatedly been associated with a cellular response.

While cells, both cancerous and non-cancerous, have been widely observed to respond to surfaces, each cell type responds differently to surface properties. This is possibly a result of them having evolved for specific functions. It could also give clues for the most beneficial environment for different cell types in terms of stiffness and roughness. Examples of this are osteoblasts and osteoclasts, which are two types of bone cells that have been found to grow well on stiff nanotubes, and less well on smooth surfaces. Environmental factors can also affect this response as can be seen when comparing cells grown on 2D surfaces to those grown in 3D matrices. On flat substrates an increase in adhesion was typically observed. Depending on the stiffness of the 3D structures adhesion could be more reversible (softer scaffolds) or more stable (harder scaffolds) [3].

Stiffness has been observed to influence a variety of cellular mechanisms, such as proliferation, differentiation, migration and gene expression [125]–[127]. The stiffness of human tissue varies from 0.5 kPa to 12kPa for live, soft tissue, to 15–100 kPa for fibrotic tissue, and up to 350 MPa and 17 GPa for bone tissues. This is a broad range of stiffness that different cells will be responding to [128], [129]. Mechanical changes in the ECM can be reflected in the cellular activity and phenotype. Cells grown on stiff substrates also show

an increased expression of stress fibres and integrins, as well as changes in their adhesion to the substrate [3], [125]. Soft substrates can also be non-viable for some cell lines [125].

The cells are considered to interpret surface roughness as structural variations in the ECM, which the cell then adapts to [130]. This way the conditioning film of previously adsorbed proteins influences the adhesive interactions, as proteins have adsorbed differently on different features of the surface [130]. The Focal Adhesion Kinase signalling pathway has been associated with cell proliferation responses to roughness [3]. The scale of the surface feature appears to be an influential factor, at least in the case of fibroblasts, where smaller features (10–13 nm) increased adhesion and proliferation. Larger features (50–95 nm) resulted in a lower fibroblast adhesion [130]. Differences have also been shown between random surfaces and surfaces with an organised structure, the latter directing spreading and migration [3]. Differences in metabolic rates have also been observed when comparing this type of features — an ordered micrometer scale topography increased the metabolic rate of osteoblasts compared to a disordered surface [130].

Functional groups on the surface have also been observed to affect the functionality of cells. For instance, surface modifications with carboxylic acid (-COOH) and bisulphite ($-HSO_3$) groups have been shown to increase HeLa cell proliferation. The migration of these cells was increased by addition of amine ($-NH_2$) groups [3]. Surface charge has also been found influential and could be a partial explanation to why cells respond to some chemical species on the surface. A lower negative potential was associated with an increase in cell adhesion and spreading, as well as modulations in actin stress fibre formation [131]. Hydrophilicity is a surface energy property that generally improves adhesion and proliferation of mammalian cells, while hydrophobic surfaces typically inhibit them [3], [43]. Surface properties have also been connected to the response of immune cells to implant surfaces, effectively upregulating and downregulating the inflammatory response [118]–[120]. Titanium surfaces with an increased hydrophilicity were also observed to decrease cytokine production, which increases the inflammatory response, and promotes the production of anti-inflammatory agents [120].

At the frontier of materials for controlling cell-surface interactions are materials with properties that can drive responses in neural cells. Nanostructures have been shown to influence also neural cells, but for this type of electrically active cells material conductivity is also of interest. Such materials could be implemented in applications needing electrical stimulus to connect with neural tissue, which has been utilised in pacemakers, vision protheses and brain-interfaces [132], and by extension to prevent and treat neurological disorders or improve quality of life of patients [133]. Electrical

stimulus has also been observed to affect neural stem cell migration, differentiation and proliferation which could be utilised to improve the poor generative properties of the central nervous system [134], [135]. Fibroblast cells have also been observed to respond to electrical stimulus (ES). *In vitro* studies have observed an increased secretion of growth factors, cell growth and cell migration of HDF cells [136], [137]. Electrical stimulation of the pelvic floor was observed to promote the activation and proliferation of fibroblasts *in vivo* in a mouse model [138]. An example of a non-electrical surface property that influences neural cells is, as said, topography. Rough surfaces appear more viable for neural cells than smooth ones [139]. Neural cells have been observed to respond to nanoscale features, such as grooves between graphene oxide, in terms of attachment. Neural stem cell differentiation has also been shown to be directed by fibrous structures. Improved proliferation has been observed on 3D graphene structures [140]. On polystyrene (PS) surfaces with microscale roughness, human induced stem cells show differences in neuronal markers, indicating a differentiation response [141].

These examples on cellular responses to surface properties indicate that the responses are as diverse as the surface properties that drive them. Differing responses between cell lines convolute the matter. Some generalised observations have been suggested in a review by Li, Xiao and Liu [3]. Positively charged and moderately hydrophilic surfaces increase cell spreading, while softer materials reduce it. Topography can induce a phenotype change related to spreading. Proliferation is induced by 3D structures, especially when interconnected, but stiffness and topography also increase proliferation through different signalling pathways. Cellular differentiation has been connected to variations in stiffness, but also the ordered nature of the topography can affect it, with osteogenesis preferring random structures, while neurogenesis prefers ordered structures. Surface functionality, for instance pre-adsorbed proteins can also influence e.g. proliferation [3].

4.3.3 The predictive power of physico-chemical models for mammalian cells

As with microbial cells, the DLVO theory was initially deemed suitable for describing initial mammalian cell-surface interactions due to the size of these cells and the properties of their membranes, which are typically hydrophobic and negatively charged [5]. The main issue here was the surface heterogeneity of the membrane in both a chemical and physical sense. Similarly, a thermodynamic approach requires the definition of some equilibrium state, which for cells might not even exist [142], [143]. The cascade of interactions of a cell with different surfaces and the subsequently expressed and modified ECM limits the use of these theories in the long term, but their use has merit when the focus is the initial adhesion [143]. While emphasis is generally laid on longer interactions and confluent films, the initial, short-term adhesion steps could still influence the long-term interactions between the biological environment and the material. Investigating the validity of these physico-chemical models and further developing them can thus also help further the understanding of cellular interactions with functional biomaterials. What such materials are will be discussed next.

5. Functional materials at biological interfaces

Functional materials either possess a property that has an intrinsic function, or that can show a function under some external stimulus. For functional materials at a biological interface, or biofunctional materials, the function is some kind of biological interaction, or the possibility to initialise or tune an interaction with a biological object, which can be on any level — cell, tissue or organ. As previously established, surface properties can affect cell-material adhesion, cell migration, cell spreading, cell shape, cell proliferation and cell differentiation through their chemical, topographical and mechanical properties on a cellular level. Materials engineering aims to make use of such cellular responses to benefit certain applications [3]. Typically, a cell-line specific response is sought after. This can be exemplified by dental implants and wound dressing applications where bacterial infections and inflammatory responses should be suppressed, whereas soft and/or bone tissue interactions with a functional material should be promoted [116], [117], [144].

In this final section of the literature overview some examples of uses of biofunctional materials are described. Focus is put on polymeric materials and their processing into biofunctional films.

5.1 Biofunctional materials and their applications

Biofunctional materials can be designed to primarily function as impermeable surfaces, such as bioactive coatings, but they can also be intended to allow for release of a molecule, such as in the case of drug delivery systems [145], or the passing of cells into their matrix, as in the case of, e.g., scaffold materials [123], [130], [144], [146]. Even the earliest biofunctional materials research could show that surface and colloid science is a key field when investigating and determining interactions between materials and proteins or cells [147]. The idea was that all interactions, biological or not, are driven by the same fundamental forces [72]. As has been indicated, and this still appears to hold true, a decisive model requires accounting for an unfathomable number of different interactions. Some key aspects, like reactivity of water at materials surfaces through hydrophobic and hydration forces, are still partly unresolved [147], [148]. In medical applications, biofunctional applications are commonly termed biomaterials. Currently, there is a shift from permanent, i.e. non-degradable, implants towards biodegradable biomaterials where plausible [149].

Biomaterials are often metallic (e.g., titanium implants), ceramic (e.g., bioactive glass), polymeric (e.g., polystyrene (PS)) or natural-based (e.g., cellulose or plant scaffolds).

Metallic biomaterials and ceramics are common in implants not least due to their durability [150], [151]. Such applications include joint replacements, dental implants, orthopaedic fixations and stents [152]. Currently, also biodegradable metallics are available, which are typically based on Mg, Fe and Zn alloys rather than, e.g. stainless steel found in permanent implants. These provide better fracture fixation where complete tissue regeneration is expected. The result is still a strong and biodegradable implant. Shape-memory alloys are a sub-type of metallic materials that can have beneficial properties in the biomedical field. Shape-memory refers to the capability of a material to return to its original shape after a deformation, even below its transition temperature. Nitinol, which is one of several titanium-nickel shape-memory alloys, has been widely used in different medical applications, such as dental, vascular, neurological and vascular a.o. [152]–[154]. This material could for instance allow for operating through a smaller incision and expanding the used device only in the last stages of the procedure [155]. A limit to their use has been the control of Ni released from the material. For all types of metallic biomaterials, 3D printing has provided interesting new manufacturing possibilities [152], [156].

Ceramic materials are often used to interact with bone tissue. Of note are calcium phosphate based ceramics which are biocompatible, but their degradation products can contribute to bone cell activity [149]. Similarly, calcium silicates provide means to influence bone calcification and can promote collagen and bone-related gene expression, through Si-cell interactions [149]. Bioactive glasses, which consist of SiO_2, CaO, and P_2O_5, among others, provide good biocompatibility and strong bonding in proximity with tissue. These are in fact the only bioceramics bonding with both soft and hard tissue [149], [151]. A weakness of bioceramics is their low toughness, which can be improved by using it in a composite material together with tougher components [149]. While bone regeneration is the major application for this group of materials it is expected to perform also with soft tissues, in wound healing, as scaffolds or even in cosmetics [149], [151].

Polymers are used vastly as biomaterials in diverse applications from medicine and food technology to cosmetics due to their versatility and affordability [145], [157]. They can be tuned to suit any application, and offer a wide selection of chemical, topographical and mechanical properties [157]. Polymeric materials can also be made stimuli-responsive, meaning that some of their properties, like surface charge or stiffness, undergo a change when they are exposed to a stimulus, e.g. light, pH-change or electric stimuli. This can be used in biosensors, where a material reacts to a pH change induced by

inflammation, or the release of a medical agent from an implant material surface due to an increased tissue heat or pH change [155]. The stability of polymeric materials can also be tuned to suit the needs of the application, as they can be made both biodegradable and stable over the long-term [149], [157]. Biodegradable polymers are often, however, considered to be mechanically inferior to biodegradable metallics, when used in implants [152]. Shape-memory effects have also been observed in polymers [155]. Unlike alloys, shape-memory polymers (SMP) are generally more biocompatible. Again, the tuneability of polymers to device foam-materials is beneficial in biomedical applications. This has been utilised with polyurethane-based SMP foams for treating lateral wall aneurysms in carotid arteries of dogs [155], [158]. Polylactic acid-based polymers can show SMP behaviour and simultaneously be biodegradable [159]. Conductive polymers (CPs), like polypyrrole and polyaniline, form another subgroup of polymers, which can provide means for electrical stimulus, sensing or even neural interfaces [160], [161]. For CPs, biocompatibility and poor mechanical properties are some recurring issues [161].

Cellulose-based and cellulose-like materials are not only an interesting support for bioactive materials but are also promising on their own. This is a wide group of materials that stem from both plants and bacteria [162]. One of their strengths is the possibility to modify their chemical and mechanical properties [144], [146], [163]–[165]. This can be achieved through synthesis, processing, copolymerisation and blending. That said, naturally occurring polymers can have interesting properties that can be utilised as biomaterials but they can be difficult to modify or purify [157]. Cellulose materials can also come in 3D form, which can be printed or be the ink-basis in cell printing [166], [167]. These materials have been used for a wide range of applications from cell culture, as hydrogels, to organ scaffolds [123], [146], [162], applications which use the cellulose material as an ECM mimicker. In such 3D environments it has been observed that the stiffness is a particularly influential material property [168]–[170]. These properties have also allowed cellulose-based hydrogels to be used in dental implants, corneal grafting, or reconstructive surgery [162]. Due to its versatility and tunability, addition of metal nanoparticles or conductive materials can make cellulose a versatile sensor material [171], and it was recently even deployed as a homeostatic biosensor [172].

Paper, another cellulosed-based material, is a potential support material for a low-cost cell study or diagnostics platform [82], [173]–[176]. It is also lightweight and suitable for large scale production [176]. Cell studies have been carried out *inside* paper based structures, occasionally with added microfluidics [177], utilising the scaffold-like character of cellulose. This way paper can be utilised for both 2D and 3D cell culture platforms [165]. A key benefit of using paper is its customisability, especially when considering that

both the bulk and interfaces in the bulk can be used in cell culture [165]. Tuneability can also be provided by the inclusion plastic films, e.g. polyester, which gives the added benefit of transparency — a feature which paper-based devices are limited in [178]. If they are easy to use, sturdy and accurate, paper-based diagnostics and cell-culture devices can be invaluable in developing countries, where expensive instruments and trained personnel are severely limited [179]. Paper-based platforms have been used in a wide variety of applications, such as high-throughput screening, drug development, biomolecule detection or as a disease diagnostics tool and have been tested using a wide array of body fluid samples, from blood and sweat to tears [165], [176]. In the case of pharmaceutical studies, e.g., the tuneability and possible 3D environment can provide a more native-like environment for cells, which can add value and reliability to the study [165]. Paper has also been considered as a base for organ-on-a-chip models [180]. However, paper is not without drawbacks in these applications. Light scattering might limit confocal imaging, fluorescence imaging must be done mindful of possible autofluorescence and humidity might change the mechanical properties of the paper substrate [176].

One approach to adjust biocompatibility of a prefabricated material is by biomodification of the surface. This can involve chemical processing of the surface to adjust its surface chemical properties and can be done by grafting or otherwise adding, e.g., a polymeric coating, or even by adding biomolecules such as proteins or small interfering RNA [181]. Similarly, the surface structure can be processed [157]. Surface modification can also provide a multifunctionality to a surface. This can make a bio-inert but stable and strong material also biocompatible [152]. An advanced example is e.g. controlled biomodification of a thermo-responsive poly(N-isopropylacrylamide-co-2-carboxyisopropylacrylamide) grafted onto tissue culture PS. Using this responsiveness, the binding of proteins to the surface was controlled and by extension also the attachment and detachment of human umbilical vein endothelial cells [182]. Biomodification has also been investigated in the case of implants, where methods like sintering, acid etching, heat treatments and micro-arc oxidation have been used to modify surface chemistry or topography to improve cell-surface interactions [183], [184].

Some applications require a ‘one-dimensional’ interaction with its surroundings. For example, in food industry, biofilm formation needs to be controlled in order to prevent food spoilage and foodborne diseases, while bioreactor surfaces need to maximise the yield from the process [72], [95]. These applications involve different anti- and pro-microbial surfaces, which are obtained by targeting different phases in the bacterial and/or biofilm life cycle. These surfaces can be developed through physico-chemical materials design or surface functionalisation, e.g., by use of nanoparticles (NPs). NPs can not only be used to modify the physicochemical properties of a surface, but

can also provide an intrinsic antimicrobial activity, for example in the case of silver NPs [185], [186]. Initial implant materials were chosen and designed with a similarly simple point-of-view — to increase their inertness and thereby reduce the risk of rejection. Later the perspective was broadened, and materials were chosen to be biocompatible [3]. They should be suited to the application without inducing any undesired responses in the biological entity it's in contact with [157]. Biocompatibility is a common issue with novel synthetic polymers.

State-of-the-art biomaterials design often embraces a more multidimensional approach where some interactions are downregulated while others are enhanced. Examples of this are a type of superhydrophobic implant that can reduce fouling while retaining biocompatibility, and wound dressing materials with highly antibacterial properties that yet enhance wound healing [144], [187]. Advanced functional biomaterials can also be designed to show a response to changes in the environment, e.g. pH, temperature, electric field or even metabolites [157].

The application of biomaterial engineering of surfaces to cell culture applications offers interesting possibilities. Traditionally cell culture plates are made of rigid glass or plastic, and while they might have a conditioning layer, their surface chemistry and topography reflect the manufacturing processing rather than conscious design [188], [189]. With cells adapting to their environment, even differentiating due to biophysical cues, the validity and repeatability of cell studies done in environments with, for the cells, very un-native properties is critically assessed [3], [168], [189]. Using the knowledge from cell-surface interaction studies, a tuneable platform could be devised, where the most *in vivo*-like responses are obtained in *in vitro* studies.

Incorporating bioelectronic elements in a cell study platform, or any other bio-application for that matter, can add to the investigation and gained data, or add means to stimulate cells electrically or with added release of bioactive agents [190], [191]. With these one can monitor cell adhesion and viability using, e.g., impedance spectroscopy [192], or metabolites and pH sensing [193].

Printing techniques, inkjet printing and flexographic printing among others, are a convenient way to add a functionality to a surface — even on large scale — by modifying the surface chemistry or adding, e.g., electrodes [173], [174], [194]. For small scale applications, physical vapour deposition can provide a means to produce thin-film metal coatings or electrodes, especially on a small scale [190], [195]. Other ways to add surface texture or features are etching, ion beam milling, hot embossing, solvent treatments and lithography [191], [196], [197]. When studying cell-surface interactions, care should be taken when modifying the surface, because the manufacturing process can

inadvertently alter more properties than intended, for instance the surface chemistry when altering the topography.

5.1.1 Latex films as biofunctional surfaces

In this thesis the primary functional surfaces for controlling cell interaction are different nanostructured polymeric latex surfaces. A latex is a polymer emulsion produced by polymerisation, while the emulsification of a polymer results in a pseudolatex dispersion [198]. The development of these has allowed for polymeric film manufacturing to utilise water soluble or dispersible dispersions in addition to solvent-based dispersions or solutions. Water-based dispersions often need added dispersive agents, which can be a drawback when additives are undesired, such as in bio-applications [199]. They are still often preferred for being more environmentally friendly than solvent based systems [200]. Other possible additives present in a polymer latex are plasticisers (film forming agents) [141]. These can be fugitive to improve block resistance. Common latex dispersion stabilisers are anionic sulphate or sulfonate [201]. The distribution and migration of surfactants in the film can affect its properties, such as particle packing, film thickness and film-substrate adhesion [199], [202]. In the case of PS:ABS blends, an IR treatment was found to both cause partial annealing and removal of additives [201].

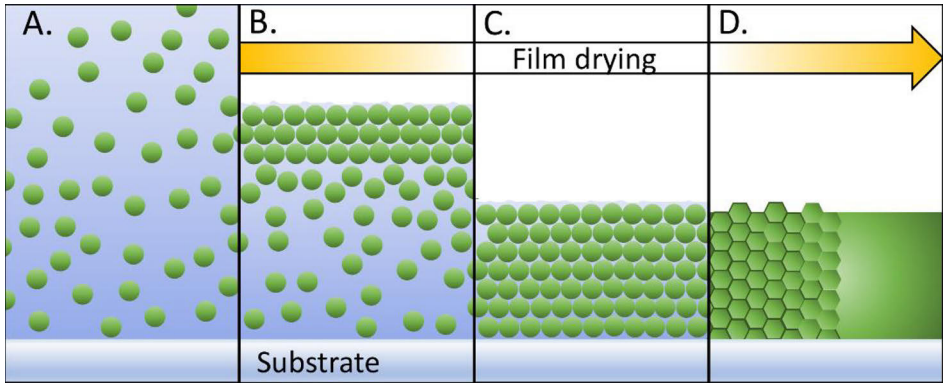

Figure 14 — Illustration of the film formation of a latex coating. The concentration of particles increases as water evaporates from the film (A to B), starting from the surface. The latex particles then organise (C) and finally deform (D). In the final stage, they can progressively interconnect to form a homogeneous film, depending on the ambient temperature and the T_g of the latex.

As a coating of dispersed latex particles dries it forms a film (Figure 14). Film-forming occurs in three steps: first the particles concentrate as water evaporates, starting from the surface. They then deform and finally interconnect by polymer chain interdiffusion. Temperature is a property-influencing factor. For example, should a film with good transparency be desired, e.g. for optical microscopy of cells, it should be cast at temperatures above the minimum film formation temperature (MFFT). Adhesion might also be affected by casting conditions [199], [203], [204].

In addition to using singular polymers, blending different polymers or including core-shell-type latex particles also provide means to obtain specific tailored properties [199]. Blends can improve block resistance, strength and integrity of the film. Influencing factors are the glass transition temperature, T_g (similar to MFFT), particle size, and relative fractions of the components in the blend [200]. The mixing ratio of latex components also forms the basis for controlling the surface topography of the resultant films [199]. The optical properties might also be affected by the mixing ratio [205], [206]. Long-term stability of polymeric films should also be considered involving changes caused by film aging, such as changes in mechanical properties or smoothening [199].

The latex surfaces, made of PS and ABS, that are used in this thesis have been shown to be cytocompatible materials with surface properties that can readily be tuned [174], [175], [191]. This has made them an intriguing means to study the influence of surface character on cells and biofilms adhering to them. The materials used and how they were manufactured and characterised is unfolded in the following section. The final section then presents observations made and conclusions drawn from the cell and biofilm studies in this work.

6. Materials and methods

This chapter describes the materials and methods used in the study.

6.1 Base substrates

Borosilicate glass substrates were used in all main studies. In Paper I and Paper II they were a preliminary test support and were used both as reference samples (as received) and coated with a polymer layer. In Paper III they were also used for preliminary testing of the synthesised latices. The glass substrates were 13 mm in diameter and produced by VWR (ECN 631–1577, Germany). Subsequent use of 'glass' and 'coverslips', or similar, in this thesis refers to these substrates.

The base paperboard used in Paper III was a commercial uncoated paperboard (henceforth "BKS") produced by BillerudKorsnäs (Sweden). The board had a basis weight of 272 ± 2 g m^{-2} and a thickness of 348 ± 3 µm.

6.2 Polymers

6.2.1 Latex dispersions

6.2.1a Commercial latices

Two aqueous latex dispersions were in focus in this thesis: A polystyrene (PS) dispersion (HPY83, Styron Europe GmbH, CH) with an average PS particle size of 130 nm and a T_g of 105 °C, and a dispersion of acrylonitrile butadiene styrene (ABS) copolymer particles (HPC26, DOW Europe GmbH, CH) with an average particle size of 140 nm and a T_g of 8–10 °C. For reference, the ABS latex DL920 in [175] is very similar, if not equivalent, to HPC26. It has previously been shown that the ABS latex includes non-ionic and hydrophilic sulphonate based surfactants. However, after thermal annealing with IR light, and a subsequent wash, the surfactants have been shown to be removed from the surface of the latex film [201]. The high-T_g latex and the low-T_g latex dispersions had a solids content of 47.9% and 54.5%, respectively. The given PS:ABS ratios and PS% are relative volume ratios of the dispersions.

The nanostructured surface texture was achieved by irradiating the latex-coated substrate with a short-wavelength infrared (IR) heater (IRT systems, Hedson Technologies AB, Sweden). The IR-treated samples were rinsed with water and ethanol, and then dried in ambient conditions. A good adhesion of the latex film to a borosilicate glass surface was ensured by an additional heat treatment (60 min, 105 °C).

6.2.1b Synthesised latices

In addition to the commercial latices, a set of in-house synthesised latices, L-01, L-02, and L-05, were used in Paper III. These were prepared via a semi-batch emulsion polymerisation. The details of the synthesis can be found in Paper III. In short, a pre-emulsion was prepared by mixing acrylic acid, butyl acrylate and styrene (Sigma-Aldrich, Finland) and emulsifiers (i.e. Disponil FES 32 and Disponyl NG 1080; BASF, Ludwigshafen am Rhein, Germany) in distilled water for 30 min at RT. A mixture containing the anionic surfactant (Calfax DB 45) solution and 50% of the total amount of the initiator (ammonium persulfate) solution was poured into the reactor and heated to 80 °C under stirring over 2 h, and subsequently stirred for another 2 h. Then the temperature was lowered to 55 °C and redox agents (tert-butyl hydroperoxide TBHP and sodium formaldehyde sulfoxylate) were added, allowing for a reaction time of 30 min at 55 °C before cooling. The pH was then adjusted with ammonium hydroxide. After removing coagulates the solids content of each product was measured.

6.2.2 Polydimethylsiloxane (PDMS)

The used PDMS contained vinyl groups (Dehesive® 920 by Wacker Chemie, AG, Germany) and was synthesised using Wacker Chemie's (Germany) chemicals Wacker® catalyst OL and Crosslinker V24 (mixing ratio 100:2.5:1 wt%). The PDMS was cured at 80 °C.

6.3 Surface manufacturing techniques

6.3.1 Drop casting

The latex blends were manually drop-cast on the glass cover slips with a radius of 13 mm. Approximately 25–30 µL of a 1:3 (latex : MilliQ-water) diluted latex dispersion was cast at the centre of each coverslip. After casting, the coverslip was manually tilted to completely spread the dispersion over the cover slip. For best results, the rotational tilting was conducted for several minutes, or until the dispersion had formed a thick skin. Transmission spectra showed that the drop cast latex films were highly transparent (90%) to light in the visible spectrum [191]. This allowed for the use of optical methods in the cell studies. By choosing suitable wavelengths (green) for confocal microscopy the disturbance of autofluorescence could be minimised (see Supporting Information in Paper I).

6.3.2 Flexographic printing of PDMS

For flexographic printing of PDMS patterns on the latex-coated paperboard in Paper III a laboratory scale printability tester (IGT Global Standard Tester 2, IGT Testing Systems, The Netherlands) was used. Printing was done at an ambient temperature of 23 °C and a relative humidity of 50%. The used anilox roll had a cell angle of 45°, a cell volume of 20 mL m^{-2} and a line count of 40 lines/cm. For ink transfer, a patterned Ohkaflex photopolymer printing plate (Espoon Painolaatta, Finland) was used. Printing produced an array of "reaction areas" or "wells" which are the non-printed areas, i.e., circular areas free from PDMS. The printing speed was set to 0.5 m s^{-1} and the printing pressure between the anilox roll and the printing plate was set to 100 N. The force between the printing plate and the substrate was set to 50 N.

6.3.3 Inkjet printing of the drug

The flexographically printed wells were loaded with drug with an ink-jet desktop printer of type Epson XP-760 (Japan). To do this, doxorubicin (DOX) was first dissolved in MilliQ water (0.1 mg mL^{-1}) and the printing solution was injected into a disposable plastic cartridge (Canon quick-fill) through a 0.2 µm polyethersulfone (PES) membrane filter. Drug loading in the well was done by increasing the number of layers (1–14) printed over the well.

6.3.4 Reverse gravure coatings

The latex dispersions and blends were coated onto the substrate papers with a MiniLabo reverse gravure coater (Yasui Seiki Co., Japan). The used microgravure roll had 120 lines per inch and a 65 µm depth, giving an approximate wet thickness of 5–11 µm (transfer fraction was 0.28). A typical coating web speed was 0.5 m min^{-1} and the rotation speed of the gravure roll 25 rpm. Two 1 kW IR driers provided sufficient drying power to provide the intended nanostructure.

6.3.5 Infrared drying and sintering

The nanostructured surface texture was finalised by irradiating the latex coating with a short-wavelength infrared (IR) heater (IRT systems, Hedson Technologies AB, Sweden) which caused partial annealing of the PS beads.

6.4 Surface characterisation

The manufactured substrates were characterised for their physico-chemical properties including wetting, surface chemistry and topology.

6.4.1 Contact angle measurements

Equilibrium contact angles, θ_a , were determined on washed and dried surfaces with a CAM200 goniometer (KSV Instruments Ltd, Finland). The drop size used was 2 µL (1.4 µL for DIM). The drops were dispensed on the surface and the contact angle was recorded for 15–25 seconds, typically at a capture rate of 1 frame per second. Occasionally higher capture rates were used (4 frames per second, Paper I). To determine the surface energies, three liquids were used: Milli-Q water, diiodomethane (DIM), and ethylene glycol (EG). The contact angles of the droplets were determined frame by frame with a software supplied with the instrument, which uses a Young-Laplace fitting method to the drop silhouette curvature.

The measured average apparent water contact angles at equilibrium were corrected for roughness using the Wenzel equation, with the developed surface area, S_{dr}, as the experimental roughness parameter for calculating factor r [45]. Surface energies were calculated with either the Owens-Wendt-Rabel-Kubelka (OWRK), or van Oss-Chaudhury-Good (vOCG) methods. Surface tension values of the probe liquids in the calculations were those suggested by van Oss-Chaudhury-Good [207].

Table 1 — Surface tension components (at 20 °C) of three probe liquids — water, DIM and EG — for determining the surface energy of a surface with contact angle measurements as suggested by van Oss, Chaudhury and Good [207].

Liquid	γ^{LW} [mJ m^{-2}]	γ^{AB} [mJ m^{-2}]	γ^{+} [mJ m^{-2}]	γ^{-} [mJ m^{-2}]	γ^{tot} [mJ m^{-2}]
Water	21.8	51.0	25.5	25.5	21.8
DIM	50.8	0	0	0	50.8
EG	29	19	1.92	47.0	48

6.4.2 Atomic force microscopy

Topographical imaging of the surfaces was conducted with Bruker's Nanoscope V MultiMode 8 atomic force microscope (Bruker, USA). Typically, 5 μm by 5 μm images with a resolution of 1024 by 1024 pixels were captured at a scan speed of 0.391–1.00 lines per second. For Paper II, 512 by 512 pixels images were used instead. For Paper I and Paper III the cantilevers used were of type NSG10 (NT-MDT, Russia), with a nominal tip radius of 10 nm and 8 nm, respectively. For Paper II NSG01 (NT-MDT, Russia) cantilevers with a nominal tip radius of 10 nm were used.

For Paper I the stiffness of some of the bimodal blends in liquid was measured with a JPK Nanowizard II AFM (Germany). These 2 μm by 2 μm force volume images were captured with a resolution of 55 by 55 pixels. For these measurements, TESP cantilevers (8 nm nominal tip radius; Bruker, USA) were used.

The Scanning Probe Image Processor (SPIP) software by Image Metrology (Denmark) was used for image analysis. The same software was used to determine surface roughness values. In all cases, filtering of the obtained topographs was conducted with the software's Gaussian filter (ISO 11562). An LMS-fit (zeroth degree) was also applied when necessary.

6.4.3 Barrier testing

The barrier properties provided by the latex coatings were tested with a modified prism-based method [13] in Paper III. This involved using a glass prism to detect time-dependent changes in the refractive index of the sample when exposed to solvents. Tests were done with three types of solvents: deionized water, ethanol, and vegetable oil. The images obtained during the experiment were analysed with an open-source Java image processing program FijiImageJ [14], [15].

6.5 Microbiological methods

6.5.1 *Staphylococcus aureus* culture

Clinical biofilm-forming strain *Staphylococcus aureus* (ATCC 25923) was stored at -80 °C with 15% glycerol added. An inoculation of *S. aureus* stock was added onto a tryptic soy agar plate (TSA, Neogen®, Lansing, Michigan, USA) and incubated at 37 °C for 18 h. Liquid bacterial cultures were obtained by transferring single colonies of *S. aureus* into 100 mL of tryptic soy broth (TSB, Neogen®, Lansing, Michigan, USA), and then incubated in aerobic conditions for 16–18 h (220 rpm, 37 °C) until bacterial growth reached 10^8 colony-forming units (CFU)/mL. The bacterial density was determined optically with a Multiskan Sky microplate spectrophotometer (Thermo Scientific, Vantaa, Finland at 595nm), followed by viable cell counting on TSA plates.

Each surface was assessed with two biological repetitions of three replicates, each in every biofilm quantification assay. Uncoated borosilicate glass coverslips were used as surface controls.

6.5.2 *S. aureus* cultivation assays

6.5.2a Agar plate assay

For the agar plate-based assay performed in Paper II, the colonisation of *S. aureus* onto the latex surfaces was conducted according to recently reported protocols [208]. Shortly described, 1.5 mL bacterial suspension (1:10 dilution of the bacteria culture in TSB, approx. 10^7 CFU/mL) was distributed uniformly over a sterile Whatman filter paper (diameter 70 mm, GE Healthcare, Little Chalfont, UK) on a TSA plate (100 mm by 17 mm, Nunclon™ Delta). The studied surfaces were sterilised by immersing for 10 min in 99% EtOH and air dried, and then placed on top of the filter paper, with the coating side in contact with the culture. Bacterial attachment was allowed for 24 h in humidified conditions at 37 °C.

6.5.2b Microtiter plate assay

For the microtiter plate-based assay in Paper II, ethanol-sterilised latex coated coverslips were placed (coating side facing upward) in flat-bottomed 12-well plates (NunclonTM Δ surface, Thermo Scientific, Roskilde, Denmark), and 1.5 mL of *S. aureus* bacterial suspension (estimated 10^7 CFU/mL) was added. The bacteria were allowed to incubate 24h at 37 °C under aerobic conditioning with shaking (220 rpm).

6.5.3 Counting viable cells

The biofilms grown on each surface in Paper II were detached by vortexing and sonication, and the loosened cells rinsed off with TSB. These were then transferred to a Tween® 20-TSB at 0.5% (w/v) solution (5 mL), vortexed twice for 10 s, with a 5 min sonication treatment (at 25 °C, 35 kHz) in a water bath (Ultrasonic Cleaner 3800, Branson Ultrasonics, Danbury, CT, USA) in between. Afterwards, the bacterial solution was subjected to 10-fold serial dilutions with TSB and plated on TSA plates. Colony forming units (CFU) were counted after 18 h of incubation of the agar plates at 37 °C and given as CFU per cm^2.

6.5.4 PNAG quantification

In Paper II, the formed PNAG quantities were measured using Wheat Germ Agglutinin Alexa Fluor® 488 conjugate (WGA, Molecular Probes Inc., Eugene, OR, USA) and by using a modified version of the protocol described by Skogman *et al.* [209]. The biofilms formed on the latex surfaces and glass reference samples during the 24 h incubation (according to 6.5.2) were soaked in sterile phosphate buffered saline (PBS) to remove loose cells and placed, coating side up, into a 24-well plate. A WGA-staining solution (15 µg/mL) was added to each well, and the dyes were fixed at 4 °C in darkness for 2 h. The samples were then washed thrice with PBS and air-dried at RT. The surface samples were then sonicated for 30 s (25 °C, 35 kHz) in 1 mL of 33% acetic acid, re-incubated at 37 °C for 1 h, and sonicated again for 30 s. Finally, 200 µL of the remaining suspension was transferred to 96-well plates for fluorescence measurements (excitation at 495 nm, emission at 520 nm) using a Varioskan™ LUX Multimode microplate reader (Thermo Scientific, Vantaa, Finland). The fluorescence signals were blank corrected for each latex blend.

6.5.5 Measurement of protein concentrations

For the protein studies in Paper II, the surface proteomes of the biofilms grown on the latex blends (30%, 50% and 60% PS) and the glass coverslip reference were cleaved off using trypsin shaving. To do this, 24 h old biofilms were grown on the samples using both biofilm assays. This method was based on a previously disclosed approach [210]. Here, films were first scrape-harvested with a 100 mM triethyl ammonium bicarbonate solution (TEAB, pH 8.4) supplemented with 16% w/v sucrose and centrifuged (4 °C, 8 000×g, 3 min). The cells were then re-suspended in 90 µL of a TEAB-sucrose solution (as above) with added trypsin (sequence grade modified porcine trypsin (Promega, Madison, WI, USA); c_{fin} 40 ng/L) and incubated for 30 min at 37 °C. These digestions were again centrifuged (RT, 4 000×g, 3 min) and purified with 0.22 µm membrane filters (Costar® Spin-X Centrifuge Tube Filter, USA) and centrifuged yet another time (RT, 16 000×g, 2 min). After a 12 h

incubation at 37 °C trypsin was deactivated by trifluoroacetic acid (c_{fin} 0.6% w/v; Merck, Darmstadt, Germany).

Protein detection was performed by a μDrop™ Plate (Thermo Scientific, Vantaa, Finland) on a Multiskan Sky microplate spectrophotometer. A comparison of cell counts before and after the trypsin shaving was done to confirm that cell integrity was maintained during the procedure.

6.5.6 Protein identification

In Paper II, the tryptic peptide samples produced were concentrated and purified with ZipTip C18 resin (Millipore®, Merck, Darmstadt, Germany), and then analysed with LC-MS/MS according to [211], [212]. This involved passing the purified peptides through an Easy-nLC 1000 nanoflow liquid chromatography (LC) system (Thermo Scientific, Waltham, MA, USA) with a quadrupole Orbitrap mass spectrometer (Q Exactive™ Plus, Thermo Scientific, Waltham, MA, USA) equipped with a nano-electrospray ion source (Easy-Spray™, Thermo Scientific, Waltham, MA, USA). The LC separation was performed with a C18 column with a flow rate of 300 nL/min. The peptides were eluted in a solvent gradient of 2% – 30% (99.9% acetonitrile, 0.1% formic acid) for 60 min. To identify proteins, the MS data was processed with the MaxQuant software 1.6.2.1 [213]. The first search of mass tolerance was set to 20 ppm and the main search of mass tolerance to 4.5 ppm. Two missed cleavages were allowed. The minimal unique + razor peptides number was set to 1, false discovery rate (FDR) to 1% for peptide and protein identification, and a label-free quantitation (LFQ) with default settings was performed [214]. Protein intensities were expressed as $\log_2$. Only proteins expressed in at least 2/3 replicates were considered valid identifications.

6.6 Cell biological methods

6.6.1 Cell culture

In Paper I, human dermal fibroblast (HDF) cells were used in the cell studies. In Paper III, both HDF and cervical cancer cells (HeLa) were used. In Paper I the seeding density was $5 \cdot 10^5$ cells. In Paper III the seeding densities were 0, 1×10^3, 3×10^3, 5×10^3, 10×10^3, 15×10^3, 20×10^3, 30×10^3 cells in either 100 μL cell medium (DMEM) in the paper-based platform wells or 200 μL medium (DMEM) in the commercial plastic microtiter plate wells.

The HDF and HeLa cells were obtained from ATCC (Manassas, VA, USA) and preserved in DMEM medium (Sigma-Aldrich, USA) supplemented with 10 % foetal calf serum (BioClear, Wiltshire, UK), 2 mM L-glutamine, 100 U/mL penicillin, 100 μg/mL streptomycin at 37 °C in a 5% CO_2 / 95% O_2 and 90 RH%

atmosphere and kept under sterile conditions in a cell culture incubator. The cells were passaged three times a week at a 1:3 split ratio and cultured under 20 passages to maintain normal phenotype.

6.6.2 Cell staining protocol

In Paper I, the HDF cells were seeded onto the substrates and grown for 96 h. In Paper III, the cell growth of HDF and HeLa cells was analysed at three different end points: 24 h, 48 h or 72 h by staining. Prior to staining, the cells were washed with phosphate buffered saline (PBS). Staining was done using a staining solution (0.2% crystal violet: 2% ethanol: 97.8% MilliQ water) for 10 min at RT, after which excess dye was removed by rinsing with MilliQ water. The samples were then dried.

6.6.3 Cell readout

To obtain cell data in Paper I, the crystal violet dye was re-solubilised in 2% sodium dodecyl sulphate (SDS) and the absorbance of each well read at 570 nm with a HIDEX micro plate reader (Finland). To obtain a comparable end-point measurement of cell growth on different materials of interest, the absorbance of each sample was normalised to the mean value of the glass coverslip samples.

To analyse the biofilms in Paper III, the stained paper-based platforms were scanned with an office scanner (CanonScan LiDe 120, Canon) at a 600-dpi resolution and analysed using an in-house analytical software. For analysing the number of cells in the multi-well plates, the crystal violet dye was re-solubilised in 2% SDS and the absorbance of each well was determined at 570 nm using a Hidex Sense Beta Plus microplate reader (Hidex Oy, Turku, Finland).

6.6.4 Phase contrast imaging of cells

For phase contrast imaging of the cells with CellIQ (CM Technologies, Finland), HDF and HeLa cells were seeded (seeding density of $5 \cdot 10^5$ cells) onto glass cover slips and coated glass cover slips placed in 24-well plates. The used cell media was DMEM. Prior to seeding, the samples were sterilised using 70% ethanol. From the cover slips a 3 × 3 phase contrast image raster was imaged at 6 h intervals over a period of 72 h, starting 24 h after seeding. The total incubation time was 96 h.

6.7 Statistical methods

In Paper I, the HDF data was statistically analysed with GraphPad Prism® 6.0 (San Diego, California, USA). The GraphPad Prism® 8.0 software was used for analysing the results from the stained cell cultures in Paper III, both from the microplate reader and the paper scans.

Statistically significant differences ($p<0.05$) in bacterial colonisation parameters, number of colonies and PNAG-fraction between the latex surfaces were determined using Welch and Brown-Forsythe analysis of variance (ANOVA) with Tamhane's T2 post-hoc means separation test executed by GraphPad Prism (version 8.0.0). The assays were compared by evaluating the assay repeatability through standard deviations (STD) and coefficient of variation (CV), the STD divided by the mean measurement of the biofilms formed on the control glass surface [215].

In Paper II the roughness parameter errors were given as a 99% confidence interval (CI), rather than as STD. The coefficients of determination were obtained using Origin (Origin2020, Version Number 9.7.0.188. OriginLab Corporation, Northampton, MA, USA).

In the abundance analysis of the proteome data in Paper II, any missing label-free quantitation (LFQ) values were ascribed by random draws from a low abundance-adjusted distribution, and then normalised to the relative abundances of proteins using Z-scores, as obtained from the Perseus software (version 1.6.5.0). This software was also used for ANOVA analysis of the differential expression of the proteome of the different biofilms. In this case three replicates per sample were used based on their log2-transformed LFQ abundances. A permutation-based false discovery rate of 0.1 was applied in this exploratory analysis of statistically significant differences among the samples. For studying the interactions of the proteins detected and to do a functional enrichment analysis (FDR < 0.05) the STRING database (version 11.0) was used [216]. The strength of the correlation between protein abundances and surface properties was evaluated first with a manual subjective screening and then with the R-squared and adjusted R-squared values obtained from curve fitting with the Origin software. Additionally, Pearson's chi-squared test and Student's t-test were calculated for the correlations, with a further cut-off value for Pearson's r at $|0.8|$.

7. Results and discussion

The common denominator of the studies conducted for this thesis is the use of nanostructured polymer coatings for cell studies and cell study applications. These surfaces and their properties, applied on different substrate materials, are described first. Then the results obtained from investigations on protein adsorption and *Staphylococcus aureus* adhesion are described (S. Paper I). After this, the formation of *S. aureus* biofilms (Paper II) as well as the proliferation of HDF and HeLa cells (Paper I and unpublished data), are discussed and related to the surface properties of the polymer films. Finally, the deployment of the polymer coatings in a tuneable analysis platform is presented (Paper III and S. Paper II). These sections are concluded with a brief commentary on aspects that can be developed, including future prospects.

7.1 The nanostructured latex surfaces

Polymer coatings were prepared from dispersions of two latices, both commercial and synthesised, as a bimodal mixture or as individual components. By varying the blend ratio, the nanostructure and surface energy of the coatings could be tuned. The manufacturing processes and methods for making these surfaces were discussed in Part 6. In this part, the topography of these surfaces is described first, followed by the surface chemistry and wetting as the second important properties. These physical and chemical properties define the functionality of the surfaces.

7.1.1 The topography of the polymer films

Different topographies were obtained by mixing the latices in different ratios. However, the topography was also influenced by the heat treatment. The coating and IR-treatment procedures are described in Part 6. The formation of the obtained nanostructures was dependent on both the relative abundances of the two components, their T_g and their particle sizes, but also surfactants present. The constituents of the dispersion ultimately also influenced the coatability and adhesion of the films [199], [200], [202].

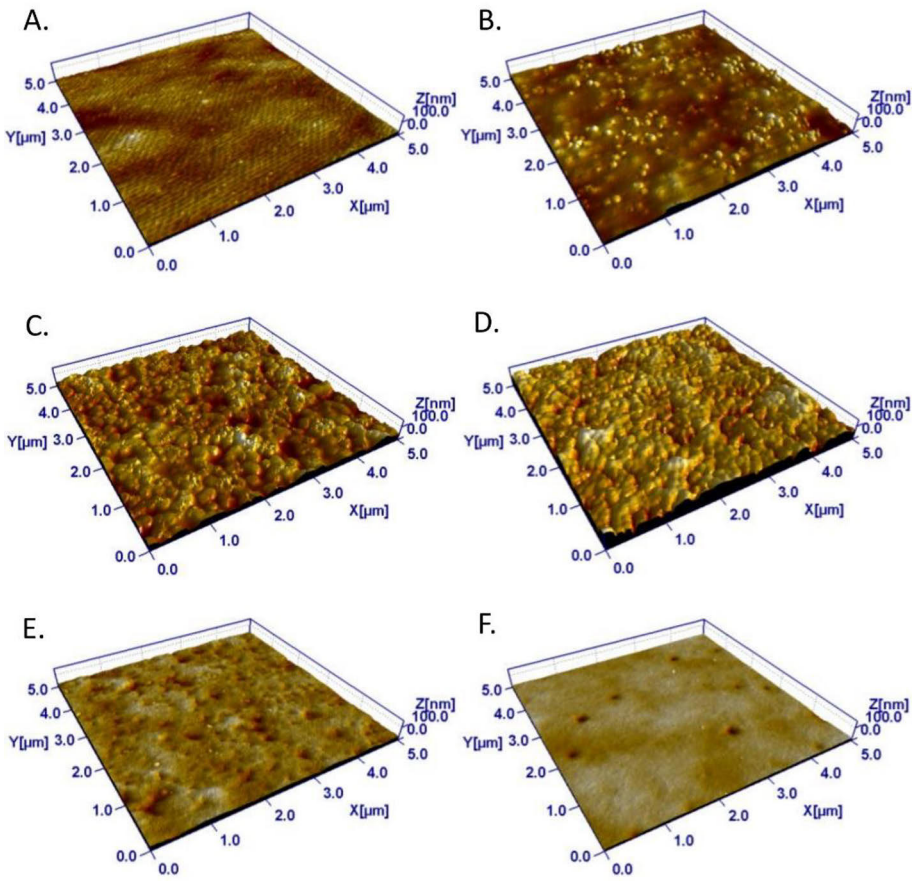

Figure 15 — Representative AFM images (5 µm × 5 µm, 512 px × 512 px) of latex surfaces on glass after heat treatment. The blends (given as percentage of PS in the PS:ABS blend) are A. 0% PS (height scale Z = 45.19 nm), B. 20% PS (Z = 76.89 nm), C. 40% PS (Z = 100.2 nm), D. 60% PS (Z = 141.2 nm), E. 80% PS (Z = 48.92 nm) and F. 100% PS (Z = 35.85 nm). The height scales are magnified by a factor of 3 to more clearly visualise the topography.

In the blend films, the ABS component has a low T_g (8-10 °C), while PS has a high T_g (105 °C). When a mix of these two is coated onto a substrate, ABS forms a film whereas PS particles retain their spherical shape and appear as high peak areas in the coating. A heat treatment partially anneals the PS particles, causing some neighbouring PS beads to adjoin and result in a partial flattening. An increasing PS content in the dispersion results in an increased number of PS 'hills' (Figure 15A,B). At a moderate PS content, most of the surface is covered by PS and the PS beads pack more tightly (Figure 15C,D). Increasing the PS content beyond this, the topographical variations come primarily from valleys between annealed PS clusters (Figure 15E,F). The packing and annealing cause the characteristic nanostructure of the films.

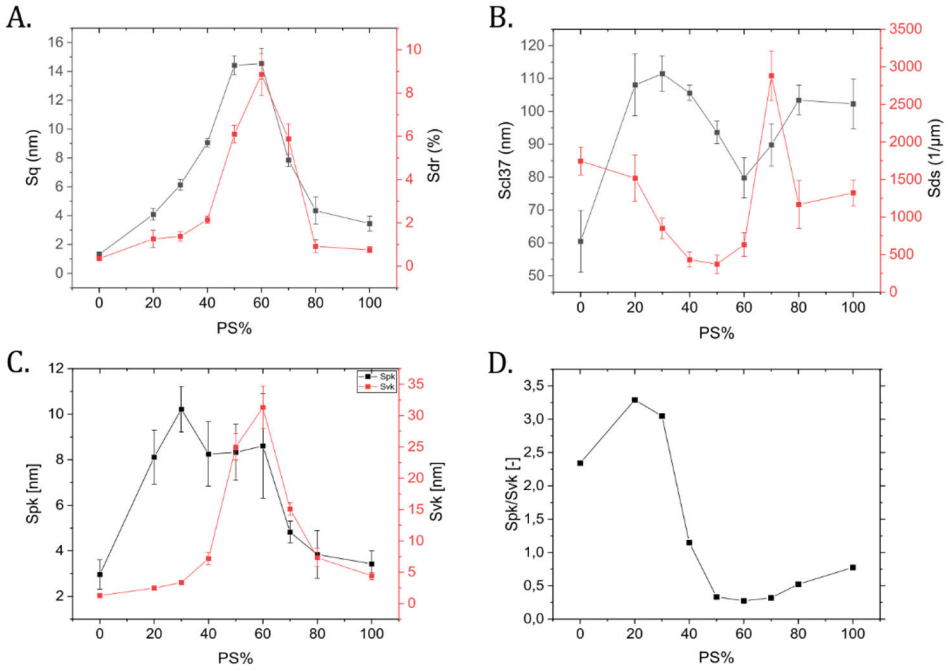

Figure 16 — Changes in a selected set of roughness parameters of the nanostructured surfaces coated on glass as the PS content is varied. A. The RMS roughness, S_q, and effective surface area, S_{dr}. B. The autocorrelation length, S_{cl37}, and density of summits, S_{ds}. C. The peak and valley contributions compared as variations in reduced peak height (S_{pk}, in black) and reduced valley height (S_{vk}, in red); and D. the reduced peak height to reduced valley depth ratio (S_{pk}/S_{vk}). Error bars indicate the 99% CI.

In Figure 16, the change in roughness with PS content is described with a few roughness parameters for latex coatings on a borosilicate glass coverslip. A more thorough listing of the variations in roughness is found in Table 2–Table 4. These roughness values could also be compared to Figure 15. In Figure 16A both S_q and S_{dr} have a similar trend: a pure ABS surface (0% PS) is the flattest, and as more PS is added, height variations and the surface area increase. S_q and S_{dr} both reach a maximum at intermediate blend ratios. The increase in roughness can then be attributed to an increasing number of PS beads, hill areas, filling up the surface. Both S_q and S_{dr} decrease when the PS content is further increased up to 100%. These pure, annealed PS coatings are almost as smooth as the ABS film. At high PS content the height variations stem from valley areas forming between clusters of PS. Figure 16C illustrates this, by showing that S_{pk} increases already at lower PS% than the S_{vk} — this occurs immediately when any PS is introduced. Only when the surface is largely covered by PS, at intermediate blends, S_{vk} increases. It is also interesting to note that for these surfaces S_{vk} is larger than S_{pk} (three-fold, at their respective

highest values, Table 2 – Table 4). Their relationship is well illustrated by the ratio S_{pk}/S_{vk}, Figure 16D, which can be used for comparing the peak and valley character of a surface. Other examples of the characteristics of the surface textures are described with the parameters S_{cl37} and S_{ds} (Figure 16B, Table 2 – Table 4). Both parameters relate to the distribution of heights in the lateral direction. S_{ds} measures the number of local maxima per area, whereas S_{cl37} the separation between them. Thus, a high S_{ds} should indicate a low S_{cl37}, as also is seen for these latex surfaces, but for more structurally heterogeneous surfaces they might deviate, as can be seen for the 60% PS and 70% PS surfaces.

Table 2 — Roughness parameter (those primarily used in this thesis) values with 99% CI for the 0–30% PS surfaces drop cast on glass.

	0% PS		20% PS		30% PS	
Param.	**Mean**	**CI**	**Mean**	**CI**	**Mean**	**CI**
S_a	0.85	*0.08*	3.03	*0.28*	4.78	*0.27*
S_q	1.31	*0.19*	4.08	*0.39*	6.13	*0.37*
S_{sk}	2.07	*1.68*	1.26	*0.27*	0.98	*0.30*
S_{ku}	27.98	*41.44*	6.39	*1.19*	5.76	*4.55*
S_{10z}	22.82	*7.59*	44.59	*5.44*	60.09	*12.33*
S_{ds}	1744	*188*	1516	*308*	849	*132*
S_{dr}	0.35	*0.05*	1.26	*0.41*	1.38	*0.21*
S_{pk}	2.96	*0.64*	8.11	*1.18*	10.22	*1.00*
S_k	2.06	*0.15*	7.53	*0.88*	12.89	*0.64*
S_{vk}	1.26	*0.18*	2.46	*0.35*	3.35	*0.35*
S_{fd}	2.33	*0.02*	2.21	*0.04*	2.14	*0.01*
S_{cl37}	60.43	*9.46*	108.04	*9.38*	111.48	*5.39*

Table 3 — Roughness parameter values (those primarily used in this thesis) with 99% CI for the 40–60% PS surfaces drop cast on glass.

	40% PS		50% PS		60% PS	
Param.	**Mean**	**CI**	**Mean**	**CI**	**Mean**	**CI**
S_a	7.44	*0.24*	11.23	*0.63*	10.72	*0.98*
S_q	9.06	*0.30*	14.41	*0.64*	14.54	*1.06*
S_{sk}	-0.05	*0.16*	-1.02	*0.19*	-1.45	*0.32*
S_{ku}	2.86	*0.32*	3.98	*0.44*	6.10	*0.91*
S_{10z}	66.85	*8.58*	100.5	*4.9*	128.1	*18.7*
S_{ds}	430	*102*	373	*122*	632	*154*
S_{dr}	2.14	*0.16*	6.10	*0.41*	8.86	*0.97*
S_{pk}	8.25	*1.41*	8.32	*1.24*	8.61	*2.28*
S_k	24.70	*1.33*	26.15	*3.65*	20.86	*4.55*
S_{vk}	7.18	*0.97*	24.97	*2.09*	31.31	*3.39*
S_{fd}	2.08	*0.02*	2.04	*0.03*	2.10	*0.03*
S_{cl37}	105.57	*2.33*	93.63	*3.51*	79.76	*6.04*

Table 4 — Roughness parameter values (those primarily used in this thesis) with 99% CI for the 70–100% PS surfaces drop cast on glass.

	70% PS		80% PS		100% PS	
Param.	**Mean**	**CI**	**Mean**	**CI**	**Mean**	**CI**
S_a	5.48	*0.44*	3.21	*0.74*	2.65	*0.41*
S_q	7.85	*0.44*	4.34	*0.93*	3.45	*0.52*
S_{sk}	-2.01	*0.37*	-1.34	*0.43*	-0.75	*0.20*
S_{ku}	11.43	*2.91*	8.94	*3.75*	7.16	*2.61*
S_{10z}	96.9	*5.3*	53.5	*10.3*	42.7	*6.0*
S_{ds}	2881	*332*	1167	*317*	1322	*175*
S_{dr}	5.88	*0.68*	0.91	*0.30*	0.75	*0.14*
S_{pk}	4.82	*0.47*	3.84	*1.04*	3.43	*0.56*
S_k	14.09	*1.81*	8.79	*2.13*	8.19	*1.34*
S_{vk}	15.08	*1.01*	7.32	*1.47*	4.42	*0.56*
S_{fd}	2.17	*0.01*	2.17	*0.03*	2.18	*0.01*
S_{cl37}	89.81	*6.33*	103.4	*4.53*	102.3	*7.61*

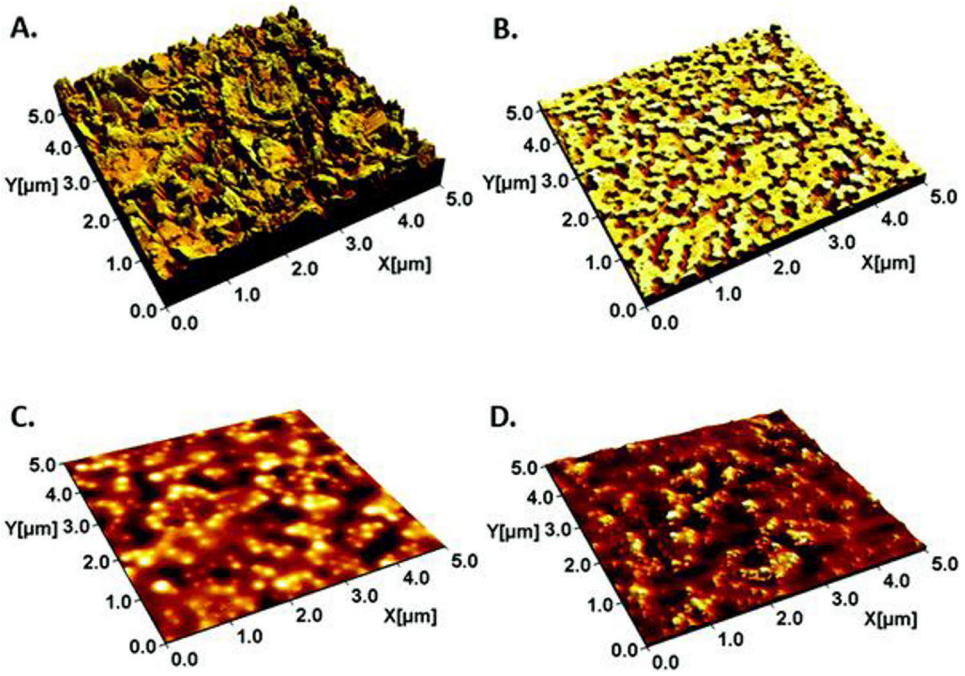

Figure 17 — AFM images (5 µm x 5 µm) of the paperboard substrate used (A.), as well as the substrate being coated with B. the PS:ABS blend (50:50 blend ratio), C. the L05:L02 blend (50:50 blend ratio) and D. the L01:L02 blend (50:50 blend ratio), used in Paper III. The height scale is magnified by a factor of 2. Reprinted from Paper III with permission by the RSC, the copyright holder.

The latex films used in Paper III were coated on a paperboard rather than the glass substrates (Figure 17). This publication also introduced coatings of the synthesized latices. Some roughness values of these surfaces are listed in Table 5. In comparison to the previously discussed 50% PS coating on a glass substrate, a paper support resulted in a significantly rougher surface — the S_q and S_{dr} being 14 nm respectively 6% on glass, and 23 nm respectively 25% on paperboard. Coatings on paperboard also showed a higher number of summits, 570 μm^{-2} compared to 373 μm^{-2} on glass. The uncoated paperboard was rougher yet before coating. Using the same descriptors show an over twice as high S_q (52.8 nm) and 3.5 times higher effective surface area (S_{dr}=85.9%) than after coating. This rougher texture could be arising from the underlying substrate, even though it appeared to be completely covered by the nanostructure familiar from Figure 15. Differences in manufacturing the surfaces were both the coating technique and the IR treatment, which most probably also contributed to variations in the topography.

Table 5 — Roughness values for uncoated paperboard, and paperboard coated twice with the three different latex blends used in Paper III. The table includes means and STD of the data.

	Unc. Board		50% PS		L01:L02		L05:L02	
Param.	**Mean**	**STD**	**Mean**	**STD**	**Mean**	**STD**	**Mean**	**STD**
S_a	40.4	6.5	19.6	0.4	10.8	0.2	2.6	0.04
S_q	52.8	7.6	23.2	0.2	13.4	0.2	3.30	0.06
S_{sk}	-0.53	0.10	-0.85	0.13	-0.41	0.05	0.52	0.16
S_{ku}	4.19	0.53	2.96	0.27	2.99	0.13	3.75	0.24
S_{10z}	489	57	155	26	92	2	28	1
S_{ds}	232	41	570	64.6	610	24	1955	197
S_{dr}	85.9	16.6	24.7	0.9	1.87	0.13	0.31	0.01
S_{pk}	50.7	5.2	11.2	3.5	11.1	0.6	4.7	0.3
S_k	117	22	34.8	3.5	33.2	0.9	7.8	0.3
S_{vk}	72.1	6.6	41.0	4.3	15.4	0.3	2.4	0.3
S_{fd}	2.18	0.03	2.22	0.02	2.02	0.03	2.19	0.04
S_{cl37}	117	4	83	3	145	18	173	11

The synthesised latices, L-01, L-02 and L-05, had slightly different particle sizes and T_g than the commercial ones. L-01 and L-05 both had a T_g of 100 °C, and their particle sizes were approx. 150 nm respectively 250 nm. Both were used together with the film-forming, low-T_g L-02 which had a T_g of 16 °C and a particle size of about 300 nm. These contributed to different roughness properties than the PS:ABS blend when coated onto paper. Using the same two parameters, the L-01:L-02 was slightly rougher with an S_q of 13 nm and S_{dr} of 2%, while coatings with the L-05:L-02 resulted in quite a smooth surface with S_q 3 nm and S_{dr} 0.3%.

The AFM topographs shown in Figure 17 illustrate the differences between the coatings. The surface of the L05:L02 shows the high-T_g particles separated by the low-T_g component (Figure 17C). This appears also true for the L01:L02 (Figure 17D), but for these films the high-T_g components appear to have settled so that they form protruding arrangements on the film surface. By contrast, the L05:L02 appears to have formed a very even, smooth arrangement. As on glass, the high-T_g commercial latex blend (Figure 17B) was able to anneal giving the characteristic topography.

7.1.2 The surface energy of the studied surfaces

As was described in the background section, a change in topography can often be accompanied by a change in surface chemical properties. Variations in the latter could even be expected when using a bicomponent film in different mixing ratios. In either case it is also important to establish all properties relevant for cell-surface interactions.

Wetting on, and the surface energy of, the pure commercial latices and two reference surfaces, PDMS and a Cellstar® well plate bottom, were first investigated in Paper I. A more detailed study of the surface energy variations with PS:ABS blend ratio was executed in Paper II. In Paper III, the same coatings were investigated being curtain coated, rather than drop cast, onto BKS paperboard in addition to some other surfaces relevant to the paper platform. These surfaces were reference paperboard, two synthesised latex blends, and wax (ColorQube®). In all cases the surface chemistry was determined from the contact angles of MilliQ water, EG and DIM using either the OWRK (Paper I and Paper III) or vOCG methods (Paper II), with surface tension values as suggested by van Oss-Chaudhury-Good [207] (Table 1). The water contact angles were measured after a thorough wash of the surfaces with MilliQ water to remove surfactants migrating to the surface during drying and heating [201]. The results of the contact angle measurements on the surfaces used in this thesis and the surface energy values determined from them are summarised in Table 6.

Pure ABS surfaces (denoted as 0% PS surfaces) were slightly hydrophilic with a water contact angle of 71.8° (±4.1°). They had a negative polar surface energy component, being approx. 11 mJ m^{-2}, no polar positivity, and an overall surface energy of 43.1 mJ m^{-2}, the main contribution coming from the dispersive surface energy. Pure PS surface (here 100% PS) had a similar total surface energy (44.6 mJ m^{-2}) but was nearly non-polar with the only polar component of the surface energy being the small, 0.7 mJ m^{-2}, negative component. Its water contact angle was also higher, being neither hydrophilic nor hydrophobic (90° ±16.2°). The large measurement error for the 100% PS surface was a result of microscopic cracking, with sizes beyond what could be captured by the AFM. This cracking is typical for high T_g latex films, and is caused by capillary tensions in the film during drying [217]–[219]. It could also be seen in the bicomponent films with approx. 80% and higher PS dispersion content.

Table 6 — A summary of the measured contact angles of MilliQ water, EG and DIM on surfaces investigated in the scope of this thesis, and the surface energies determined from them using the vOCG method. The error shown is the STD. All contact angle values are roughness-corrected (Equations 7 and 9).

Surface	Substr.	Contact angles [°]			Surface Energy [mJ m^{-2}]			
		Water	EG	DIM	Disp.	Pol-	Pol+	Total
BKS	—	65 ± 2	64 ± 1	71 ± 4	22.3	33.0	0.0	23.9
PDMS	—	114 ± 1	92 ± 2	96 ± 1	10.1	0.6	0.3	11.0
ColorQube Wax (black)	Paper-board	109 ± 1	85 ± 1	59 ± 1	29.2	1.0	0.7	30.9
PS	Glass coverslip	90.2 ± 16.2	45.7 ± 21.4	29.3 ± 11.5	44.3	0.7	0.0	44.6
ABS	Glass coverslip	71.8 ± 4.1	38.6 ± 9.4	34.3 ± 5.6	42.2	11.1	0.0	43.1
PS:ABS (20:80)	Glass coverslip	73.4 ± 3.4	41.9 ± 7.1	33.9 ± 7.8	42.1	10.4	0.0	42.2
PS:ABS (40:60)	Glass coverslip	76.3 ± 6.6	46.9 ± 9.4	40.4 ± 8.4	38.4	9.8	0.0	38.4
PS:ABS (50:50)	Paper-board	77 ± 3	50 ± 3	53 ± 2	32.6	10.5	0.1	34.6
PS:ABS (60:40)	Glass coverslip	74.5 ± 6.7	41.8 ± 8.7	35.8 ± 5.0	39.1	10.1	0.0	39.1
PS:ABS (80:20)	Glass coverslip	79.9 ± 3.5	44.4 ± 10.2	31.7 ± 6.4	43.0	5.7	0.0	43.0
L01-L02	Paper-board	73 ± 1	73 ± 1	61 ± 3	28.0	11.7	1.0	34.9
L05-L02	Paper-board	73 ± 2	76 ± 1	61 ± 3	28.0	10.2	1.5	35.8
Well plate	—	59 ± 3	51 ± 3	29 ± 3	44.6	13.5	1.1	52.5

For bicomponent films with low PS content, the water contact angle was observed to be rather stable at 72°–77°. Above 60% PS the surface turned progressively less hydrophilic, the contact angle being 80° at 80% PS, and was near-hydrophobic at 100% PS with a contact angle of approx. 90.2°. The change in contact angle at high PS content surfaces was associated with a reduction of the polar negative surface energy component from approximately 11 mJ m^{-2} to negligible. This is probably due to a thin film of the low T_g component covering the whole surface, when its relative abundance is sufficient. As the relative content of PS increased, less ABS was available to cover the whole area and the highest areas remained uncovered. Another surface energy variation was seen in the dispersive surface energy component of the films. For average blend ratios (approx. 40–60% PS) this was observed to decrease the surface energy slightly, going from ca 42 mJ m^{-2} to 38 mJ m^{-2} on glass. On paper, the 50:50 blend showed even lower dispersive surface energies, 32.6 mJ m^{-2}. This could be due to an increased contact area caused by waviness of length scales larger than what the AFM can detect and would therefore be unaccounted for by the roughness correction with the S_{dr} parameter.

Wetting on the synthesised latices L01:L02 and L05:L02 was similar to the commercial surfaces ($CA_{H20} \approx 73°$). The total surface energy profile was also similar to their commercial counterpart, the 50% PS, when coated on paper, with total surface energies of 34.9 mJ m^{-2} to 35.8 mJ m^{-2}, compared to 34.6 mJ m^{-2}. Similar was also their polar negative surface energy, at 11.7 mJ m^{-2} and 10.2 mJ m^{-2}, compared to the commercial 50% PS blend's 10.5 mJ m^{-2}. Their polar positive components were larger, however, being 1.0 mJ m^{-2} for the L01:L02 and 1.5 mJ m^{-2} for the L05:L02. The 50% PS on paper had a negligible base character. All three cases should eventually be compared to the commercial plastic well plate, given the application they should serve in. The standard comparison sample was of brand Greiner Cellstar®, chosen arbitrarily among commonly available brands. Its PS surface showed a generally higher surface energy — the components being γ^{tot} = 52.5 mJ m^{-2}, γ^{disp} = 44.6 mJ m^{-2}, γ^{-} = 13.5 mJ m^{-2} and γ^{+} = 1.1 mJ m^{-2}. Wetting on the commercial well plate was also higher than on any of the latex coatings ($\theta_{H20} \approx 59°$ on the commercial well plate compared to 70–80° on the used latices). As a further comparison, moderately hydrophilic surfaces (40–60°) have been shown to promote cell spreading [3]. Hydrophobicity (and low polarity) has, on the other hand, been observed to improve Schwann cell adhesion and proliferation [3], [220]. Protein adhesion is also poor to hydrophilic surfaces ($\theta_{H20} \leq 60–65°$) [43], [221]. These differences can therefore cause quite different responses in the cells.

In Paper III, other materials used were the hydrophobic ColorQube wax and PDMS. These were used to limit the wetting to the hydrophilic non-print areas, where the nanostructured latex surface was exposed (Paper III). Other than their wetting behaviour, the wax and PDMS surfaces were surface energetically rather different. PDMS is a very low energetic and nearly non-polar surface (γ^{tot}=11.0 mJ m^{-2}, γ^{-}=0.6 mJ m^{-2} and γ^{+}= 0.3 mJ m^{-2}). The wax had a much higher γ^{tot} than PDMS, being 30.9 mJ m^{-2} — and in fact a higher γ^{disp} =29.2 mJ m^{-2} than the synthesised latices. Their hydrophobicity, and in the case of PDMS also the low surface energy, directed the cell adhesion to the bottom surfaces, i.e. the different lattices [165], [174], [175].

7.2 Protein interactions with the nanostructured latex polymer coatings

Since cellular and bacterial adhesion is preceded by adsorption of proteins, studies of the interactions of proteins with the investigated biomaterials can give clues to their performance at a biological interface. Thus, in S. Paper I, the adsorption of avidin protein onto the nanostructured bicomponent latex surfaces was investigated (Figure 18A). This study also investigated other proteins. This was done by first using a 350 μg ml^{-1} avidin solution to study the loading capacity of avidin on three surfaces — 0%, 50% and 60% PS. The protein loading was observed to increase with PS content in the film, being approx. 470 ng cm^{-3} for 0% PS, 520 ng cm^{-3} for 50% PS and 590 for 60% PS (Figure 18B). Differences in adsorption were considered to be a result of surface topography, specifically S_{dr}. Large surface area has been associated with high protein loading [43]. Further, differences in surface chemistry have been observed to alter the alignment of the adsorbed proteins, changing the packing density [83]–[86]. The effect of surface properties was also seen as variations in the available binding sites of pre-adsorbed avidin when biotin-bovine serum albumin (BSA) binding was measured. In this case the 50% PS surface showed least binding of biotin BSA per avidin (1.27), slightly more on the 60% PS (1.45) and a binding of nearly 2 on the 0% PS. This underlines the varying activities of avidin adsorbed onto surfaces with different properties, which is likely due to conformational variations of the adsorbed proteins which can hide or expose active sites on the adsorbed proteins.

The investigation also looked at the arbitrating role of pre-adsorbed avidin on *Staphylococcus aureus* adhesion (Figure 18). In this short bacterial adhesion test (2 h at 37 °C), *S. aureus* preculture solution ($1 \cdot 10^8$ CFU mL^{-1} in TSB) was inoculated onto TSA plates. Into these plates, the samples that were to be studied (0% PS, 50% PS and 60% PS — both coated and uncoated with avidin) were placed. A PDMS substrate was used as a reference to which bacterial adhesion is poor. This has been attributed to both the smoothness and low surface energy of PDMS [175]. Glass was used as another reference. After incubation, reversibly attached cells were rinsed off the samples with TSB. Attached cells were removed, by sonicating immersed samples in a 0.5 wt% Tween 20–in–TSB cleaning solution, and viable cells were counted. Higher numbers of colonies than on both reference substrates were observed on all three latex surfaces without avidin, Figure 18. The cell counts were observed to increase with the PS content on the latex surfaces not coated with avidin. On the 50% PS with avidin, the colony density was low, being on a similar level as on PDMS (approx. 6 log(CFU cm^{-2})). The highest number of colonies in the study was observed on the avidin coated 0% or 60% PS (about 6.8–6.9 log(CFU cm^{-2})).

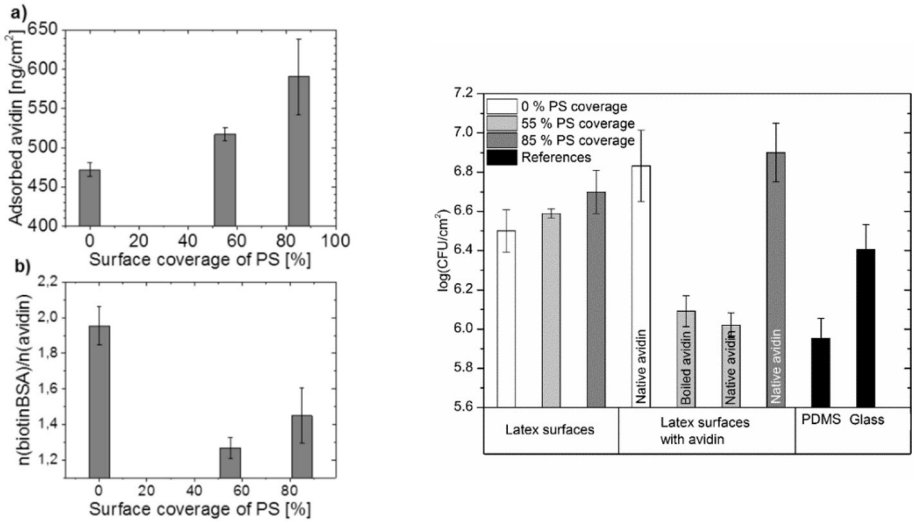

Figure 18 — Left: (a) Avidin adsorption onto different latex surfaces and (b) molar biotin binding capacity of pre-adsorbed avidin on different latex surfaces. Right: Variations in S. aureus *colony density on different latex surfaces with and without avidin, as well as on PDMS and glass reference surfaces. Surface coverages correspond to PS content as: 0% coverage – 0% PS, 55% coverage – 40% PS and 85% coverage – 60% PS. Figures are reprinted from S. Paper I with permission from Elsevier, the copyright holder.*

The study showed very different *S. aureus* attachment to avidin-coated latex surfaces with different surface properties (Figure 18). The effect of surface properties and an immobilised layer of avidin altered the attachment of *S. aureus* by either increasing the bacterial counts (for 0% PS, by 0.35 log(CFU cm^{-2}), and 60% PS, by 0.05 log(CFU cm^{-2}), statistical significance of change not evaluated) or reducing them (in the case of 50% PS, by 0.7 log(CFU cm^{-2})). The reduction in numbers of viable cells was seen for both native and denatured avidin, to a similar extent.

The variations in bacterial adhesion between different latex surfaces appeared to be a combination of the protein adsorption and the binding capacity. In the case of avidin-coated surfaces, the bacteria encountered a hydrophilic layer with high surface energy and polar negativity. An increased bacterial adhesion has been seen for hydrophilic surfaces coated with hydrophilic proteins [222]. This is similar to the case seen for the 0% PS and 60% PS. The fact that adhesion was poor with both native and denatured avidin on 50% PS confirmed that the inhibitory effect was not only related to the specific interaction between *S. aureus* and avidin, but also to the surface chemistry and topography of the surface, and their influence on protein

adsorption. The difference in activity of avidin was due to its different alignment on the peak areas of high PS surfaces, compared to the 0% PS. Specific binding might be possible on the 60% PS surface due to a rougher surface, but any interactions between pili and specific binding sites might be limited on the 50% PS surface. This might enhance the effect of avidin on specific binding.

Based on the observation that adhesion varied with film composition, a more thorough investigation of the *S. aureus* interactions with the substrates was conducted. This eventually led to Paper II.

7.3 Response of *S. aureus* on the physico-chemical properties of nanostructured coatings

It was observed in S. Paper I that adhesion of *S. aureus* to different latex surfaces, specifically 0% PS, 50% PS and 60% PS, varies. Adhesion seemed to be improved by an increasing PS:ABS ratio of the coatings. Being inspired by this observation a more elaborate investigation of the responses of *S. aureus* to different surfaces properties was performed, which resulted in Paper II. In addition to a wider selection of both surfaces and descriptive parameters, the impact of using different assays was examined. The bacterial response was quantified with the following measures: colonies per area (CFU cm^{-2}), poly-N-acetylglucosamine (PNAG) level at the endpoint (measured as relative fluorescence units, RFU) and protein expression on three selected surfaces and borosilicate glass reference. From the surface proteome of the biofilms, the abundance of some proteins with a known role in pathogenicity and virulence were selected for a further study, and their yield was investigated towards the surface roughness properties.

7.3.1 Microbiological variations observed when growing *S. aureus* on nanostructured surfaces

The viability of *S. aureus* on the latex surfaces after 24 h was measured first. This was done with both the agar plate and the microtiter plate assays (Figure 19, left). In the agar plate assay, the cell numbers were measured to be on a similar level on all surfaces up to 60% PS, after which they progressively decreased to reach a minimum level at 80% and 100% PS. In the microtiter plate assay, the cell numbers appeared to increase with low to moderate PS surface content, reaching a maximum at 70% PS, only to decrease again at the highest PS content, reaching occasionally even lower levels than that of 0% PS.

Similarly, the expression of the extracellular matrix component PNAG was investigated. With the agar plate assay, the lowest PNAG levels were observed for the one-component surfaces and the 80% PS. On other surfaces up to two times more PNAG was measured, with 30% and 60% PS having the highest levels of PNAG. Generally, a lower PS content yielded more PNAG. For the microtiter plate assay, the relative differences were smaller. The highest PNAG amounts were observed for the 40% PS, while low amounts were observed on the 50–70% PS samples. Other surfaces showed moderately high amounts of PNAG. It has been shown that PNAG plays an important role in bacterial adhesion and biofilm formation [223], [224].

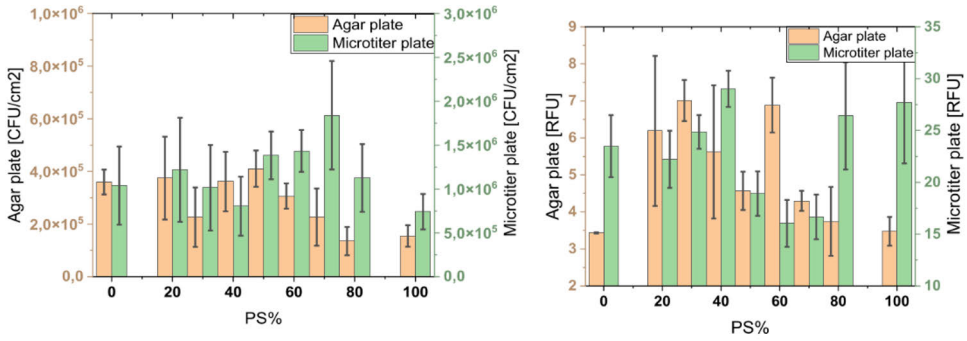

Figure 19 — Response of S. aureus *to the different surfaces measured as colony density per area (left) and detected PNAG (right) obtained from two different assays, the agar plate assay (peach) and the microtiter plate assay (green). The error bars show the SEM error.*

The quantified surface proteins were obtained by trypsin shaving from three bicomponent latex films and a glass reference from both assay types. It was found that while the total concentrations did not vary significantly between biofilms grown with the same assay, the concentration was assay dependent. Concentrations were lower for the agar-plate based assay, being 0.03–0.06 mg mL^{-1} cm^{-2} compared to 0.18–0.21 mg mL^{-1} cm^{-2} for the microtiter plate assay. An identification of these proteins also showed that the number of different proteins was almost 50% higher in the biofilms grown in the microtiter plate assay — 382 proteins were uniquely identified, in addition to the 935 proteins identified in the agar plate films. Most of these were classified as hydrophobic proteins. There were also differences in the individual proteins expressed on the different surfaces. An ANOVA analysis showed that 49 and 106 proteins in films from the agar plate assay and microtiter plate assay, respectively, differed to a statistically significant level in abundance between surface samples. Of these proteins, the ones that could be connected to some clinically relevant functions were further studied (25 of 49, resp. 31 of 106). Such functions were pathogenicity, host immune response evasion and pathogenic moonlighting proteins.

7.3.2 Pursuing surface properties that drive a microbiological response

While the *S. aureus* viability was originally intended to be investigated simply in comparison to a surface character, it was quickly observed that also the assay used influenced the outcome of the investigation. This was seen both as higher cell numbers counted in the microtiter plate assay — up towards ten times more than in the agar plate assay — and as different surfaces resulting different relative viabilities within each assay experiment. This could be a result of different seeding densities relative to the surface area in the different assays, possibly affecting the response related to biofilm maturity.

To investigate how different surface properties affected the viability of biofilms, the viability was plotted not against the blend ratio, but rather against individual surface properties. This approach was eventually used for all chosen measures of biological response, and, for the viability and PNAG expression, also using a combination of surface properties.

7.3.2a Viability variations in *S. aureus* biofilms with surface properties

A slightly lower viability was observed on the least polar and least hydrophilic surfaces (80% and 100% PS) in the agar plate assay. These two surfaces appeared to result in lower viability than surfaces with some similar topographical properties. This indicates that this parameter could be a driving factor. This was the case for instance with the 20% PS with similar S_q, S_{dr}, S_{ds}, and S_k, as 80% and 100% PS, but was much more peak dominated as indicated by S_{pk}/S_{vk}. A direct connection between dispersive surface energy and viability of *S. aureus* could not be made due to simultaneous changes in amplitude roughness (e.g., S_q) and dispersive surface energy. In the microtiter plate assay, no clear connection between surface chemical properties and viability could be made.

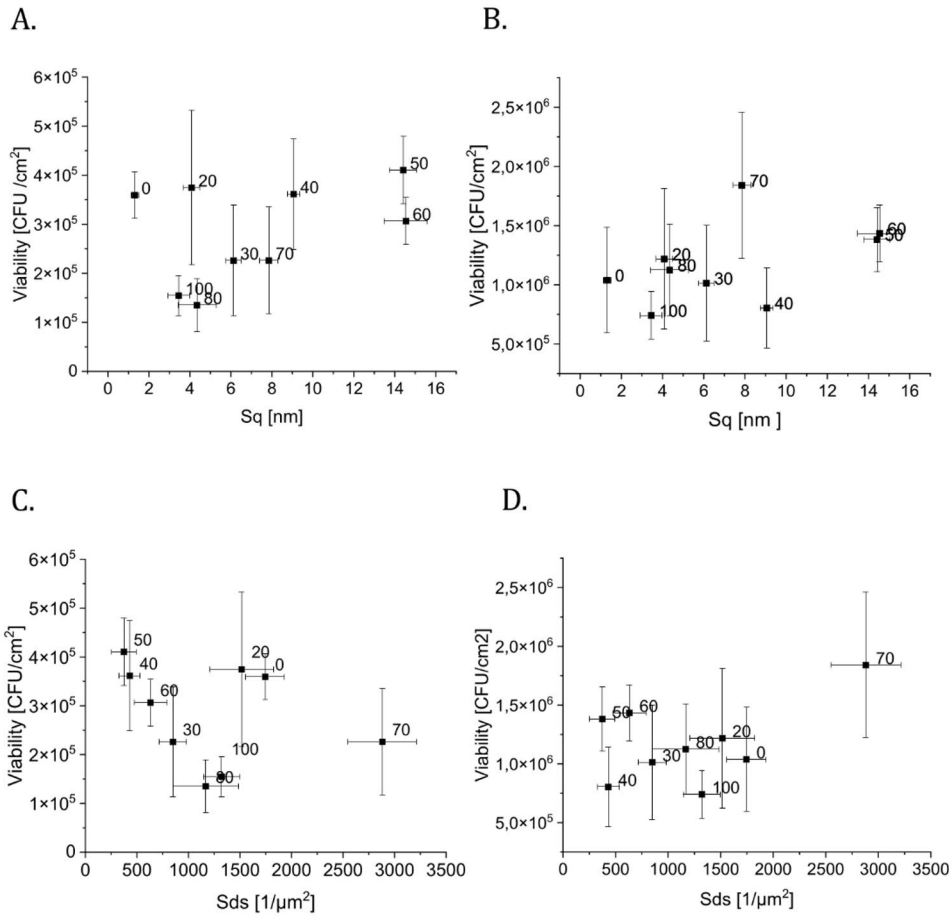

Figure 20 — Colony densities in agar plate (left column) and microtiter plate conditions (right column) to S_q, A. respectively B., and S_{ds}, C. respectively D. The error bars show the 95% confidence level for the S. aureus *data and 99% confidence level for the roughness characterisation. Figures are reprinted from Paper II with permission from Elsevier, the copyright holder.*

An interesting observation was that a higher (amplitude) roughness in the studied interval (1–15 nm) did not clearly increase the viability in either assay, as has often been reported (Figure 20A,B). In the agar plate conditions, several height-related parameters (S_q and S_{pk}) showed that the sample with the lowest height parameter values (0% PS, and often also 20% PS) gave the highest viability. The shape of the curves when either parameter was plotted against the viability are reminiscent of the plots that were obtained when investigating the effect of fine-structure parameters on viability, in particular S_{ds} (Figure 20C,D), and also the parameters S_{fd} and S_k. These showed that the viability corresponded rather linearly to these parameters if the 0% and 20%

datapoints were omitted — viability decreasing with increasing S_{fd} and S_{ds} and also increasing with increasing S_k (not shown). This indicates that a rougher surface, with some spacing between asperities, improved the bacterial viability. The S_{pk}/S_k parameter from the bearing area curve could provide some further insight to this, indicating that either a fine structure roughness (dominating S_k) or amplitude roughness (dominating S_{pk}) could augment the viability (Figure 21A). This parameter could also account for the low polar negative surface energy surfaces, 80% and 100% PS.

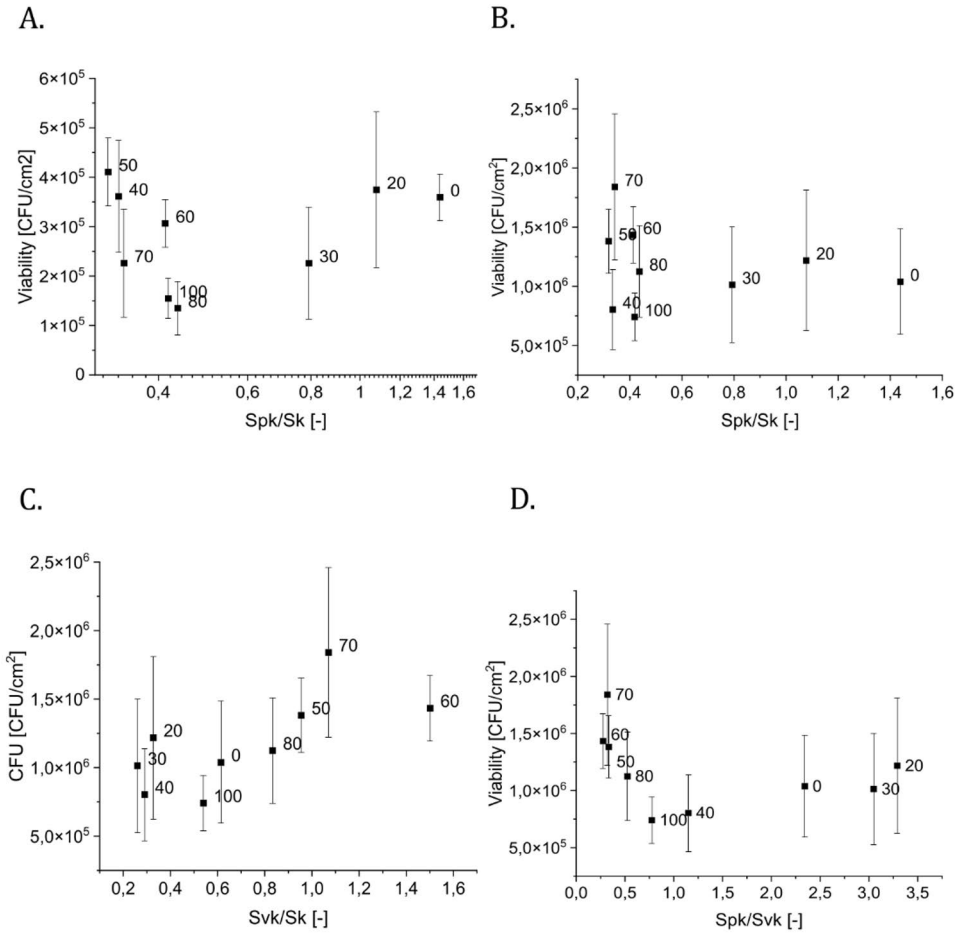

Figure 21 — S. aureus *viability variations with some roughness parameters: A. S_{pk}/S_k in the agar plate assay, as well as B. S_{pk}/S_k, C. S_{vk}/S_k and D. S_{pk}/S_{vk} in the microtiter plate assay. The error bars show the 95% confidence level for the* S. aureus *data and 99% confidence level for the roughness characterisation. Figures are reprinted from Paper II with permission from Elsevier, the copyright holder.*

As the microtiter plate viability data showed fewer statistically significant variations, it was more difficult to draw conclusions about which topographical parameters, if any, influenced the *S. aureus* viability in this assay. A higher S_q, S_{dr}, and S_q/S_{cl}, was more likely to result in higher viability. Unlike what was observed for the agar plate conditions, the fine texture (S_{fd}, S_{ds}, and S_k) did not show any connection with viability (not shown). The bearing area curve gave more clues, however. All surfaces that had high viability had a low S_{pk}/S_k (Figure 21B). For this assay, S_{vk}/S_k appeared also to express a viability driving factor, specifically, meaning that deeper valleys resulted in a higher viability (Figure 21C). Comparing the dominance of valley and peak regimes of the surfaces through the S_{pk}/S_{vk} parameter (Figure 21D) the viability gave another perspective on the viability-driving character of the surfaces, and the clearest trend. This showed that *S. aureus* studied in a microtiter plate assay is more viable on surfaces with either a dominating peak height or valley depth.

As a comparison, in S. Paper I, a larger number of *S. aureus* colonies was observed with increasing PS content (S. Paper I, Fig. 8). In S. Paper II, the bacterial growth protocol was most similar to the microtiter plate assay protocol used in Paper II. A major difference was the maturity of the biofilms investigated — 2 h in S. Paper I, compared to 24 h in Paper II. The used coatings also had slightly different properties due to a different substrate and coating. In both studies lower colony densities were observed on the 0% PS film compared to the PS blend surfaces.

7.4.2b PNAG abundances in *S. aureus* biofilms vs. surface properties

The PNAG abundance in 24 h *S. aureus* biofilms was measured with both the microtiter plate assay and agar plate assay, on all nanostructured latex surfaces. The responses in the agar plate assay were seen to depend on surface wetting and polarity (not shown). No clear response to the surface energy in the microtiter plate assay was observed (Figure 22A and not shown data). However, in this assay, a high amount of PNAG was detected on surfaces that had a low polar negative component (100% and 80% PS) even if the number of colonies was low on these surfaces (Figure 19). This could indicate a weak response in the PNAG expression of the biofilms.

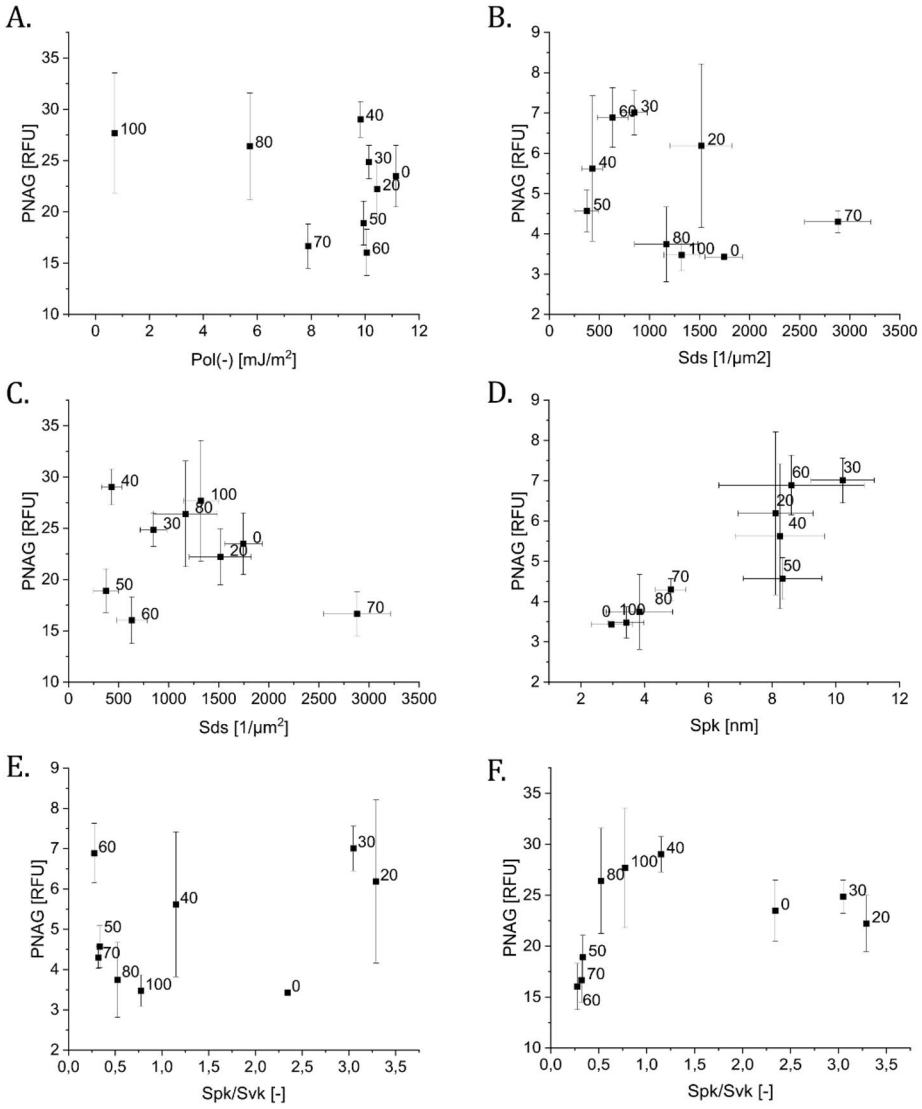

Figure 22 — PNAG abundance variations plotted against different surface properties: (A.) the polar negative surface energy for the microtiter plate assay; (B.) S_{ds} of the agar plate assay; (C.) S_{ds} of the microtiter plate assay; (D.) S_{pk} of the agar plate assay; and S_{pk}/S_{vk} for both agar plate assay (E.) and microtiter plate assay (F.). Figures are reprinted from Paper II with permission from Elsevier, the copyright holder.

The topography of the surfaces also appeared to drive a different PNAG response than what was observed for the viability. For instance, in both assays an increasing S_{cl37} appeared to increase the amounts of PNAG in the biofilms, indicating that spacing between asperities was influential. The effective surface area also appeared to affect the PNAG amounts in the microtiter plate,

a higher area decreasing the detected levels of PNAG. The fine structure parameters, S_{fd}, S_{ds} and S_k (Figure 22B,C), also appeared to influence the PNAG expression. These three parameters all showed the highest detection rates at intermediate values, typically with the low polarity surfaces separating from the group. The real response behind this observation could be their description of small-scale peak and valley geometries, which were also investigated through the S_{pk} and S_{vk} parameters, as well as their normalisations (S_{pk}/S_k, S_{vk}/S_k, S_{pk}/S_{vk}). First, an increasing peak height S_{pk} seemed to increase the PNAG biomatrix component in the agar plate study (Figure 22D). In comparison, no clear relationship with this parameter and the detected PNAG amounts could be observed in the microtiter plate assay (not shown). For the microtiter plate assay, a possible decrease in PNAG abundance was observed with an increasing S_{vk}. Normalising the parameter with the core roughness, S_{vk}/S_k, showed a much clearer trend of decreasing PNAG expression with a higher parameter value. The peak counterpart, S_{pk}/S_k, showed the highest values for intermediate parameter values in the agar plate assay, interpreting a lower PNAG value on the 80% and 100% PS to low polar negative surface energy. A weak decrease in PNAG expression was seen for an increasing S_{pk}/S_{vk} parameter in the microtiter plate, with the three surfaces with higher S_{vk}, also showing low values and resulting in low PNAG detection rates. This perspective, relating peak heights and valley depths with the S_{pk}/S_{vk}, yielded the clearest trends (Figure 22E,F). According to this, surfaces with a higher peak height or a deeper valley depth resulted in higher PNAG abundances in the agar plate assay — the opposite being true in the microtiter plate studies. Not fitting the trend in the agar plate data is the 40% PS sample, with higher PNAG rate than expected according to this trend. This data point also had a relatively high error. Some surface properties of this sample stand out — its features were neither peak nor valley dominant (S_{pk}/S_{vk} approx. 1), it had among the lowest dispersive surface energies and a low S_{ds}. This perspective was also in line with previous results that a higher roughness affects cells, but it also indicates that, on this length scale and this type of disordered hemispherical geometries, the surface topography should also be clearly dominated by peaks or valleys.

7.4.2c Combined effects of surface chemistry and topography on *S. aureus* biofilms

Driven by a vision that both surface chemistry and topography together affect biofilms, a simple model that could account for these properties was considered. Interesting figures were obtained by using parameters that account for height variations (S_q and S_{10z}) and the density of asperities (S_{ds}) together with the surface chemistry parameters that most probably influence the biofilms — the contact angle and the polar negative surface energy component. The model aimed for a linear alignment of the biological response, BR (in units of CFU/cm^2 for viability, and units of RFU for PNAG abundance), plotted against the key surface properties, SP, with a slope a and intercept b:

$$BR = a \cdot SP + b \tag{19}$$

The agar plate assay viability data showed a reasonable linear fit for the following model:

$$BR = a \left((S_{ds} \cdot S_{10z}^2)^{\frac{1}{Pol-}} \right)^{-1} + b \tag{20}$$

The statistical strength of the fit was R^2 = 0.81 and Pearson's r =0.90 (Figure 23a). For the PNAG abundance data from the agar plate assay, the best fit was found for

$$BR = a \left(S_{ds} \cdot S_q \right)^{\frac{1}{CA}} + b, \tag{21}$$

but this still gave a weak correlation (Figure 23c). The height variations appeared to have an emphasised effect on the viability (squared S_{10z}). While a 'model' accounting for the effect of the polar negative surface energy component on the *S. aureus* viability gave the best fit, it could be compared to a differently weighed water contact angle, since the surface in parallel becomes less hydrophilic and less polar. A mathematical issue with the use of this parameter is that the polar negative surface energy component approaches 0 mJ/m^2 for the 100% PS surface, which tended to draw out the datapoint where this parameter was used (e.g., Figure 23a). Eventually, a smarter, yet undiscovered way of utilising the parameter might yield even better results. The model utilising Eq. 21 was successfully deployed for both datatypes obtained for the microtiter plate assay — the viability and biomatrix expression (Figure 23b and Figure 23d). The obtained correlation strength was R^2 = 0.80, Pearson's r = 0.91 and 0.60, Pearson's r = 0.81.

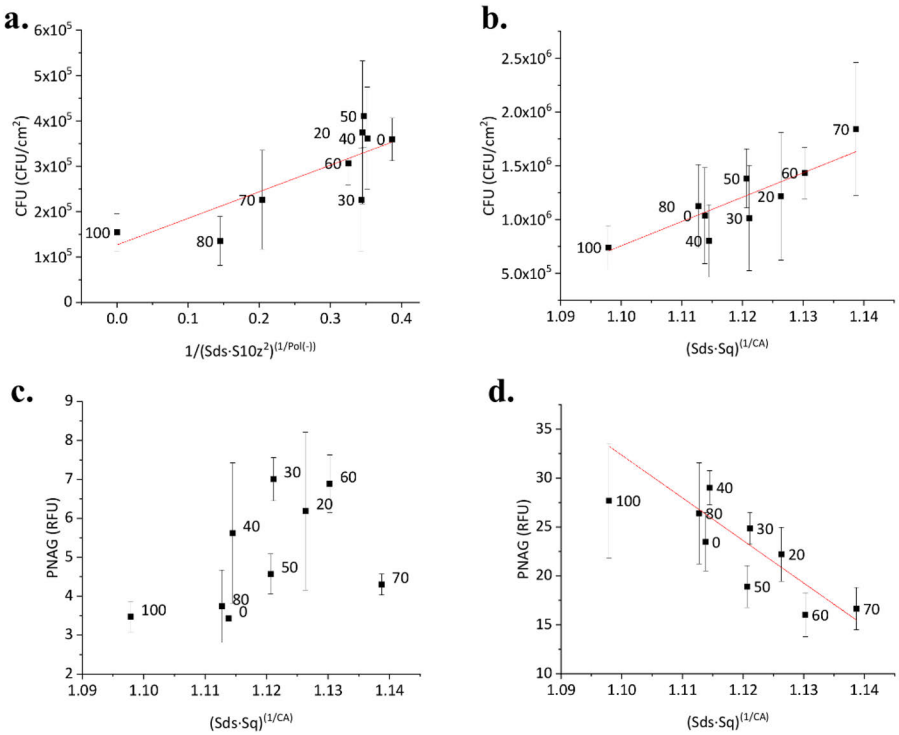

Figure 23 — Illustrations of the rudimentary models for a) number of colonies in the agar plate assay with Eq. 20, b) number of colonies in the microtiter plate assay with Eq. 21, c) PNAG amounts in the agar plate assay with Eq. 21, and d) PNAG amounts in the microtiter plate with Eq. 21. Best linear fits with Origin shown in red. Error bars show 95% confidence level. Reprinted from Paper II with permission from Elsevier.

The models suggested in Equation 20 and 21 account for both the height variations in the form of S_q or S_{10z} and the distribution of asperities through S_{ds}. These two surface parameters are enough to describe a simple Gaussian surface. For these surfaces the height distributions are slightly more complex. Particularly for the blends in the mid-range which can be described as bimodal from a histogram perspective. As discussed, physico-chemical models for describing particle-surface interactions have used parameters describing these surface properties in describing the adhesion force, but weight the different parameters in different ways [77]. These would probably be better fit for explaining very early cell numbers. Similarly, the response to the surface chemistry is already complex on a protein level, where even simple protein mixtures can be observed to have various interactions with the material. But, seeing that even such rough trends could possibly describe the maturation of a biofilm is quite interesting.

7.3.2d Phenotype changes in *S. aureus* biofilms due to surface properties

The variations in the detected PNAG and number of colonies, and their connection to surface properties raised the question whether the variations in the protein detection could be connected to the surface character. After all, phenotype changes have been reported for adhered bacteria, but also connected to responses of mammalian cells to surface properties [3], [89].

Similar to the other biological responses scrutinised, the protein abundance of each significantly varying and clinically relevant protein was analysed against the surface properties of the four samples used for this part of the study — 30%, 50% and 60% PS, as well as the glass reference. In numbers, the investigated proteins were 25 out of 49 proteins detected on the surfaceome in the agar plate assay that were associated to virulence-related functions. In the microtiter plate assay, the number was 36 out of 106 proteins. The linear correlation strength of their abundances to surface properties was investigated with the R^2, Pearson's r and Student's t. The cut-off value for a strong correlation was set at Pearson's $r \geq 0.8$, a cut off value which also resulted in high R^2 and student's t values. An example of two correlations is shown in Figure 24. Here, Immunoglobulin G-binding protein A and Nitrodreductase abundances in biofilms grown in the agar plate assay were seen to linearly grow with increasing S_{ds} of the latex surfaces. Assuming a linear fit, these two correlations had R^2=0.9477 and Pearson's r=0.973, respectively R^2= 0.9751 and Pearson's r=0.9751. A full listing of the 61 proteins which were found to correlate with some surface character can be found in Paper II – Supplementary Information.

Even with these limitations the abundance of several proteins was discovered to correlate with some of the roughness parameters that caused a response in *S. aureus* viability and PNAG abundance. In the agar plate assay, all but six proteins appeared to have some correlation with the surface properties. The others appeared to fall into two groups depending on which parameters they responded to. In the microtiter plate assay, strong correlations with the surface properties were found in spite of the relatively few statistically significant differences in viability (CFU cm^{-2}) or PNAG detection. Of the 36 proteins, only three protein abundances could not be correlated to any roughness parameter.

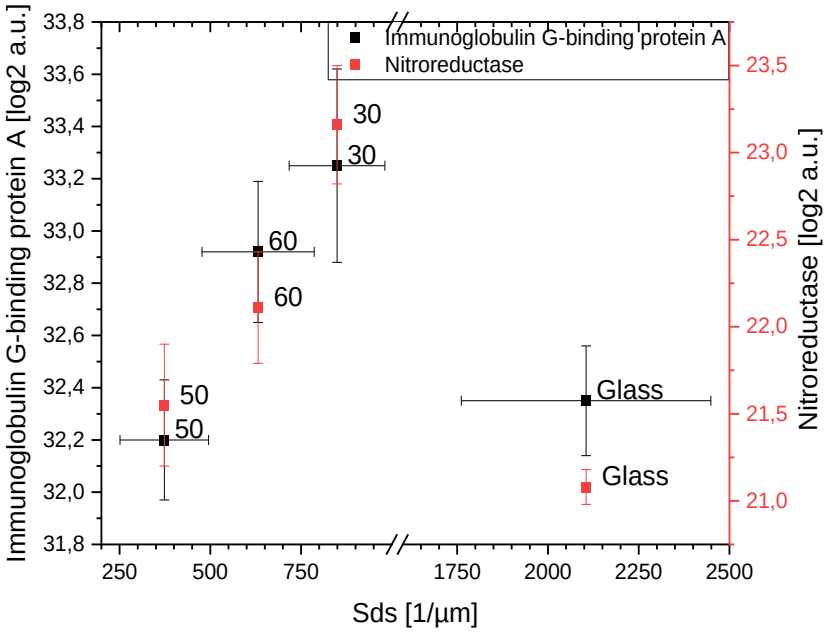

Figure 24 — The change in Immunoglobulin G-binding protein A (black) and Nitroreductase (red) abundance with a change in S_{ds} for biofilms grown in the agar plate assay.

The surface proteins, named after their placement in the microbial cell surface and their role in cell-surface interactions [225], were thus observed to often respond to the surface properties the bacteria had adhered to. The impact of the assay type was also significant, showing an enriched protein function for the microtiter plate assay. Many of the successfully correlated proteins, in both assays, were so called moonlighting proteins, that have been considered to be strategically excreted by the microbe and, as their name suggests, could fill multiple roles in the cell function [226]–[228]. These include virulence factors and mediators of host factor attachment [226], [229]. Others, such as lipoteichoic acid, have been associated with bacterial growth and cell division, and in the case of pyruvate dehydrogenase and pyruvate kinase moonlight as adhesins [230]. The largest group was the ribosomal proteins, which have been associated with biofilm integrity [231]. A final set of proteins that could be specifically highlighted are the antibiotic target, penicillin-binding protein 2, and cytosolic proteins, related to the antibiotic resistance and chronic systemic infectivity of *S. aureus* [232], [233].

7.3.3 Conclusions

Staphylococcus aureus biofilms were grown on 9 nanostructured two-component polymer surfaces in two different assays. The results from the two assays differed on all levels — the number of colonies, the detected PNAG levels, and protein abundances but also in how these responses were affected by the surface properties. Both PNAG expression and *S. aureus* viability, measured as viable cells per area, were markedly higher in the microtiter plate conditions. Also trends among the surfaces were different between assays. This could be a result of different surface-to-volume ratios between assays, but also the mechanisms with which the bacteria attach to the substrate. Indications that the assays might differ in oxygen concentration was also found, as several proteins relating to the anaerobic growth mode were enriched in the biofilms. The choice of assay should therefore be done carefully, and mindfully of what conditions would suit the perspective of the study or application of the material(s) investigated.

In agar plate conditions, the surface chemistry of the substrate affected the biofilms. In particular, a decreased hydrophilicity and polar negativity decreased both the viability of, and PNAG detection in, the *S. aureus* biofilms. Those surface roughness parameters that reflect the fine structure character of the surface, i.e., S_k, S_{ds} and S_{fd}, were found particularly influential. Biofilms grown in the microtiter plate assay were not observed to be influenced by the surface chemistry. Parameters that described the relative dominance of peaks or valley areas appeared to do so — these included S_{pk}/S_k, S_{vk}/S_k, and S_{pk}/S_{vk}. Rougher surfaces, especially where the roughness was increased by valley structures, increased the viability and decreased the PNAG expression. The autocorrelation length, S_{cl37}, and the effective surface area, S_{dr}, also seemed to describe a surface character that influenced the PNAG expression in the biofilms.

These observations of influential individual parameters were combined to see if they could together account for a general response of the studied bacterial model to both surface chemistry and topography. Combining both amplitude parameters, asperity densities or average separation, as well as surface chemical parameters a rudimentary 'model' could be described. The suggested model, and the combination of these parameters, could be interpreted to relate to adhesion, as it bears similarities to models used to describe colloidal particle interactions with topographically heterogeneous surfaces, e.g. [77]. Developing a true model would need more data over a broad range of structural and surface geometries, however, and a computational approach.

The investigation of the potential influence of the surface character on the phenotype, or protein abundances, gave a more detailed look into how bacteria respond to the properties of the surface they adhere to. Similarly, to

the viability and PNAG abundances, 15 out of 26 investigated proteins were found to correlate with the fine structure parameters, when the agar plate assay was used. The correlation length, S_{cl37}, was also found to be a parameter that several (5 of 26) protein abundances could be linked to in the agar plate assay. Likewise, the protein abundances measured in biofilms grown in the microtiter plate assay appeared to correlate with the parameters that influenced the viability and PNAG abundance. Particularly common were the S_{cl37}, S_{pk} and S_{pk}/S_k parameters which 25 out of the 31, 17/31 and 15/31 closely investigated proteins appeared to correlate with. Another influential topographical character appeared to be the one described by the S_q/S_{cl37} parameter, to which the abundance of 18/31 proteins could be correlated.

As these proteins had been associated to bacterial virulence and pathogenic pathways, these observations could be valuable for developing medical surfaces or implant materials. A correlating behaviour between surface character and protein expression has not been, to our knowledge, reported before. Not only would a further investigation of whether these surfaces could similarly impact other bacterial models be interesting to conduct, but also of whether surface properties directly impact the virulence of bacteria. This could be valuable when countering fomite transmission.

Another highlight of this study is the benefit of using the multitude of parameters available to the surface scientist. Using a more varied parameter toolkit can clarify which parameters drive the bacterial response in interactions with surfaces, which otherwise risk being missed. In this case the combination of the amplitude parameter S_q with peak and valley related roughness parameters helped to distinguish between the impacts of an overall roughness over specific height domains. Using only the most common S_q and S_{dr} would have missed the observation that other aspects of the surfaces also can influence different surface protein abundances. All parameters used here are equally easily available.

7.4 Controlling mammalian cell proliferation with nanostructured latex polymer coatings

As was discussed in previous sections, both bacterial and mammalian cells can respond to surface properties. In the case of bicomponent polymer surfaces it was first observed that mammalian cells respond well to their properties when used in studies of ARPE-19 human retinal pigment epithelial cells [175]. We thus hypothesised that HDF cells, too, could respond to these surfaces. This was the outline for Paper I. Later, in Paper III, we wanted to test human HeLa cervical cancer cells. In this section, viability data of HDF cells from Paper I are presented. In addition, observations on the viability response of HeLa cells to the surfaces are included for comparison. The latter are yet to be published at the time of writing this thesis.

7.4.1 HDF and HeLa viability on latex coatings

The study was conducted on glass coverslips with drop cast nanostructured coatings with PS% 0–100%, onto which $3 \cdot 10^5$ of either HDF or HeLa cells were seeded. The proliferation of cells was imaged with CellIQ during a 96 h incubation period, to detect any morphological changes indicative of cell stress, and the cultures were stained with crystal violet and the staining intensity was used to obtain endpoint measurements of cell viability. These viability numbers are presented in Figure 25.

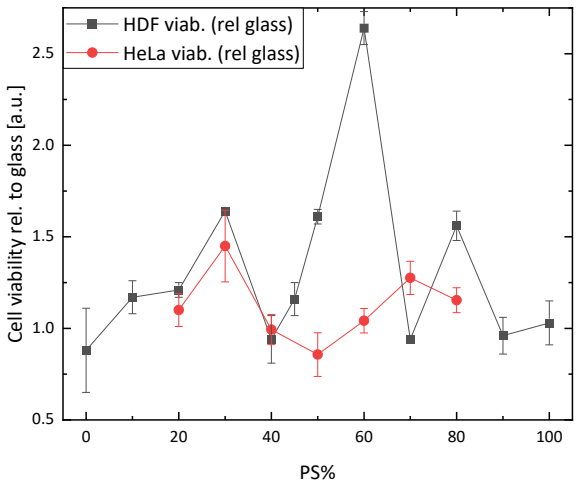

Figure 25 — Variations in the viability of HDF and HeLa cells, expressed relative to the glass reference used, grown on the nanostructured bicomponent latex surfaces with varying mixing ratio of the components given as PS%.

At the lowest, the viability for both the HDF and HeLa cells grown on the nanostructured bicomponent surfaces was at a similar level as those grown on the glass reference. The surfaces with the highest and the lowest PS contents resulted in relatively low HDF viability, with also the intermediate 40% and 70% PS surfaces giving similar results. For HeLa cells, viability was low on the intermediate 40 to 60% PS, with a minimum level of viability on the 50% PS surface. The other surfaces resulted in cell numbers higher than the reference glass, especially for the HDF cells, which yielded exceedingly high cell numbers on 60% PS (over 2.5 times the glass reference level) and approximately 1.5 times above the reference level on 30%, 50% and 80% PS. The HeLa cells showed the highest cell yield on the 30% and 70% PS surfaces, the former displaying a 1.5-fold increase in yield compared to the glass reference, the latter a slightly smaller effect (1.25). The trend here suggests different responses for the different cell lines, especially on the 50% and 60% PS surfaces.

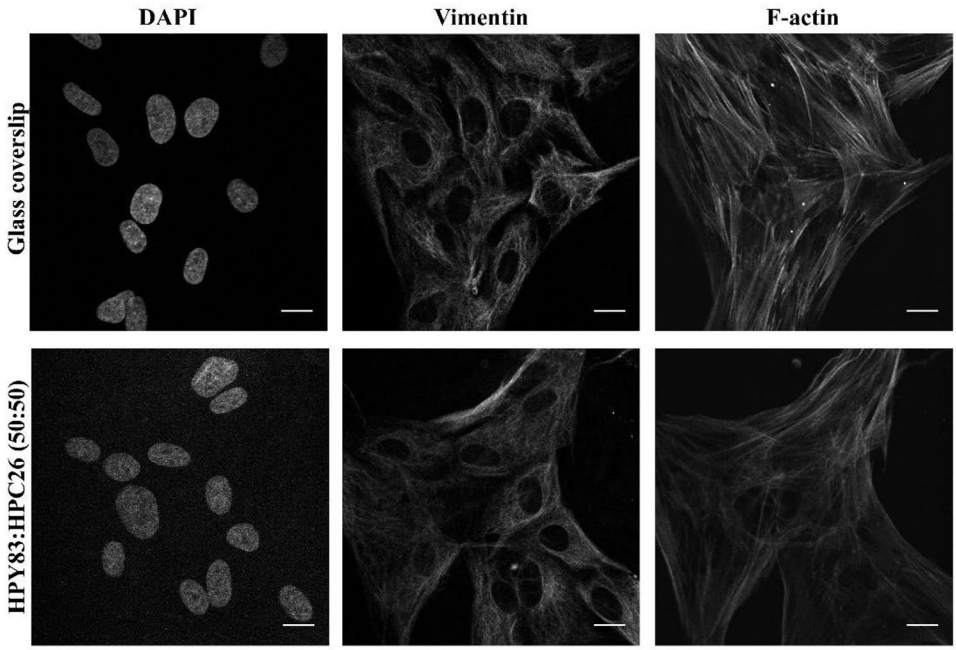

Figure 26 — HDF cells cultured on glass (top row) and 50% PS (bottom row) imaged with confocal microscopy. The scale bar is 15 µm. Nuclear staining (DAPI, left column) revealed the nuclei of the cells. The distribution of vimentin in the cells is shown in the centre column and F-actin is shown in the right column. Figure is reprinted from Paper I with permission from Elsevier, the copyright holder.

In Paper I, HDF cells grown on 50% PS surfaces were compared with cells grown on glass using confocal microscopy (Figure 26). DAPI staining, which showed the nuclei of the cells, indicated no major DNA damage due to the latex surface. Neither could any morphology changes be observed when the cells were stained for vimentin — the filament structures of cells cultured on glass and latex appeared similar. An interesting difference was seen in the filamentous actin (F-actin) abundances. This showed a larger amount of F-actin in cells grown on glass. This could on one hand be a result of substrate stiffness, the glass having a stiffness of 30 GPa while stiffness of the 50% PS was measured with AFM to be 1–2 GPa [188]. It could also be a response to the latex surface topography being interpreted as ECM cues [3], [126], [234].

7.4.2 Analysing the surface properties that drive the mammalian cell response

The response of HDF cells to different surface parameters was investigated in Paper I, using the same approach that was deployed for investigating the response of *S. aureus* biofilms in Paper II. This approach involved studying possible connections between surface properties and, in the case of mammalian cells, viability measured as cell yield compared to the borosilicate glass reference. In this section, yet unpublished results for HeLa cells cultured on the nanostructured polymeric surfaces are also presented. These data allow for a comparison of the responses of the two cell lines, HDF and HeLa, giving their responses a broader context, as well as adding an interesting background for Paper III.

7.4.2a Surface properties driving viability of HDF

Paper I focused on the cellular response to the topographical variations of the bicomponent polymer surfaces. However, in the investigation of *S. aureus* cells, Paper II, the observations were expanded not only with new roughness parameters, but also with some considerations on surface chemistry that could shed light on the nature of the surfaces that the cells respond to. The surface parameters included in Paper II, but not considered in Paper I, are added to the discussion here, as they add further insight to the surface character the HDF cells respond to.

Although hydrophilicity has been associated to an increase in proliferation [3], [43], a decreased hydrophilicity, as seen for the high PS% surfaces, did not show any significant impact on the cell yield. Both low PS and high PS surfaces, that are similarly smooth but represent different polar negative surface energy components, had a similar viability. Since the polar negative surface energy component decreased simultaneously as the hydrophilicity of the surfaces, the individual effects of these two properties could not be decoupled.

Based on the observation that the dispersive and total surface energy showed a slight reduction at average blend ratios, we were curious to see whether there is any connection between the parameters and the cell yield. Such a connection could not be made (Figure 28A).

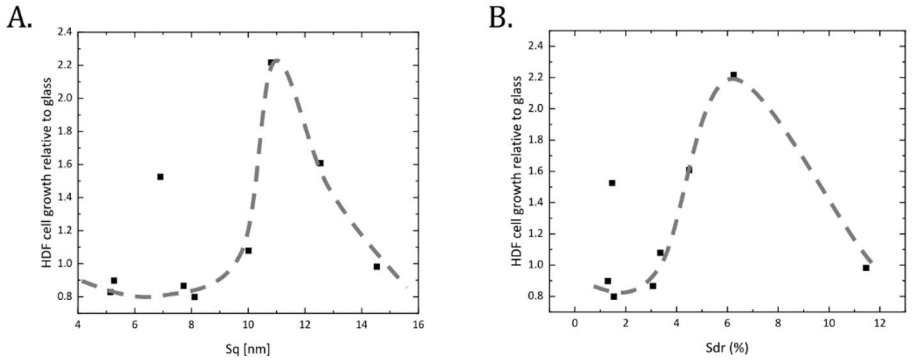

Figure 27 — Variations in the HDF cell growth relative to glass with changes in (A.) S_q and (B.) S_{dr}. Images reproduced from Paper I with the permission of Elsevier, the copyright holder.

Based on previous results it was expected that roughness would be a driving parameter for cellular viability. In this case the roughness parameters S_q and S_{dr} were considered, which HDF proliferation appeared to follow at a first glance (Figure 27A,B). A positive influence of height roughness parameters was also expected based on literature [3], which was confirmed by our data. In particular, the highest maximal viability was observed on surfaces with an S_{dr} and S_q of approximately 6% respectively 11 nm. This maximum corresponded to a normalised roughness (S_q/S_{cl37}) value of about 0.15. The published observation that cells show the highest proliferation rates on surfaces having near Brownian fractal dimensions (2.5) [235] also suggested that S_{fd} would be a potential parameter describing the cell response. This was not observed for these surfaces (Figure 28C). The investigated length scale of the surfaces in [235] was higher than what was used in this thesis (S_a up to 100 nm). This could indicate that some other descriptor, linked to S_{fd}, might be the true driver behind the response, i.e., that the observation is more specific to geometry than what can be deduced from the mere two parameters that noted the observation. Alternatively, the relevance of this parameter could be length scale specific. When S_{fd} was associated to the fine structure of the surfaces, due to its connection to S_{ds}, the HDF viability appeared to loosely decrease with increasing summit density (Figure 28B).

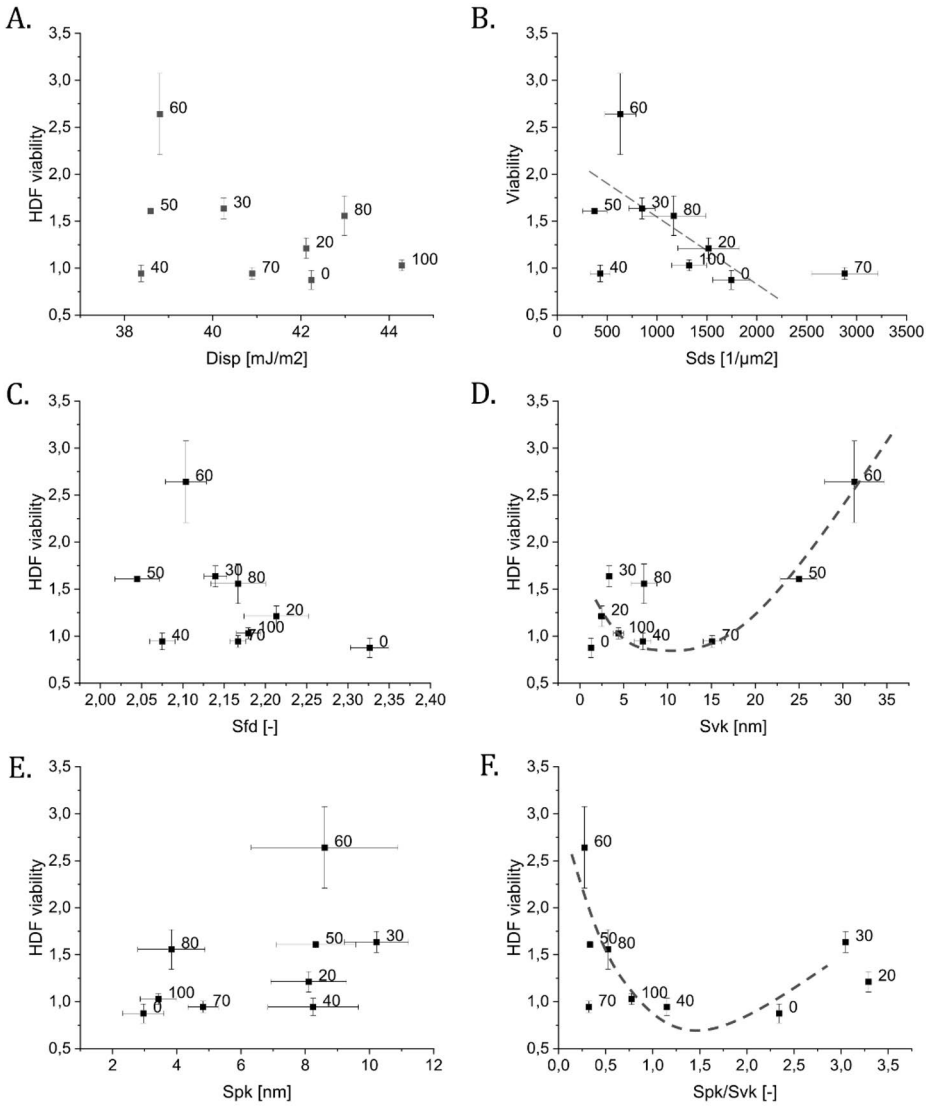

Figure 28 — The variations in HDF viability (relative to glass) with changes in the parameters A) dispersive surface energy B) S_{ds}, C) S_{fd} D) S_{vk} E) S_{pk} and F) S_{pk}/S_{vk}. Dashed lines show suggested trends.

While the 40% PS appears to have a lesser cell yield than what the loose trend of S_{ds} suggests, and 60% and 70% a higher viability than suggested, these could be explained using some additional functional parameters (Figure 28D-F): S_{pk}, S_{vk} and S_{pk}/S_{vk} (unpublished data). These parameters helped to indicate if peaks or valleys are more influential on the cellular response. This feature could not be distinguished from S_q and S_{dr} alone. A relationship could also be observed when comparing cell yield versus S_{vk} and yield versus S_{pk} plots (Figure 28D-E). In these figures the cell yield appears to increase when

the reduced valley depth (S_{vk}) is higher than 15 nm. No equally clear trend was observed for the parameter reduced peak height (S_{pk}), but interestingly, it remained below 15 nm for the whole set of data. Further, a viability vs. S_{pk}/S_{vk} plot has a parabola-like shape with a minimum at a ratio within 1.5–2. This can be interpreted such that both valleys and peaks can improve the HDF yield, which indicates the same for viability.

Going back to Figure 28B, and the suggested trend, the low viability on 40% could then be explained by that the surfaces are neither clearly peak nor valley dominated ($S_{pk}/S_{vk} \approx 1$). The 60% surface, which showed the highest viability overall, had the most valley dominated topography and the highest S_{vk} (valley depth) (Figure 28D,F). Finally, that the 70% PS sample had the third highest valley depth and a dominating valley structure could be used to explain the relatively high viability observed in Figure 28B. That S_{ds} was a potential driving parameter was also observed for *S. aureus* biofilms.

Based on this data, it can be hypothesised that the adhesion mechanisms, such as focal adhesion, that HDF cells utilise to attach to surfaces might be geometrically limited to respond to surfaces beyond a certain size (S_{pk} = 15 nm), and with clearly dominating peak or valley roughness character.

The yield of HDF cells was also observed to be lower on the pristine, i.e., non-IR-treated surfaces, which had a relatively high roughness (S_q = 25 nm, with a 0.75-fold decrease in cell yield — data not shown) due to the PS beads retaining their hemispherical shape. This effect could be a result of the different surface properties, but it has also been observed that such surfaces show lesser protein adsorption, possibly due to the surface chemical changes caused by the treatment [201]. This could also relate to differences in adhesion interactions associated to hemispherical surfaces [79].

7.4.2b Surface properties driving the viability of HeLa cells

The HeLa human cervical cancer cell line is one of the most used immortalised cell lines in cell studies. It has also been shown to respond to surface properties such as surface energy, charge and topography, but also stiffness and surface modifications [236], [237]. These considerations, as well as its availability, made the cell line an interesting counterpart to compare with the HDF cell data.

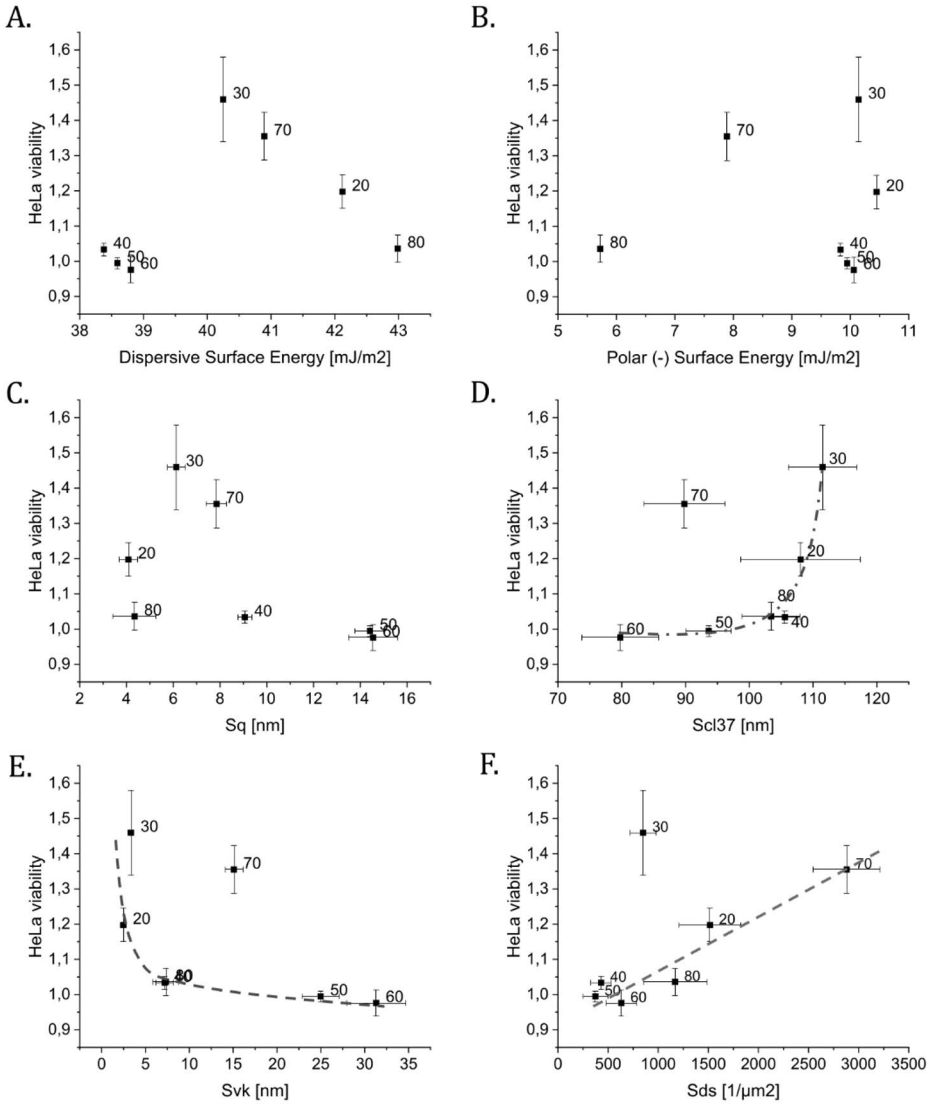

Figure 29 — The measured viabilities of the HeLa cells plotted against A) the dispersive surface energy component of the samples; B) the polar negative surface energy component of the samples; C) the RMS roughness (S_q) of the samples; D) the autocorrelation length (S_{cl37}) of the samples; E) the reduced valley depth (S_{vk}) of the samples, and F) density of summits (S_{ds}). Dashed lines indicate suggested trends.

HeLa cells appeared to be more responsive to the surface energy than HDF cells in terms of cell yield (see Figure 29 and Figure 28). Foremost, the dispersive surface energy seemed influential, an intermediate value, just over 40 mJ m^2 (Figure 29A), resulted in the highest cell yield. A closer examination indicated two groupings with one group having relatively low dispersive surface energy and a comparatively high roughness (e.g., S_q and S_{dr}), i.e. 40%, 50%, and 60% PS, and another group with a lower roughness and slightly higher dispersive surface energy. A lower polar negative surface energy component could also be a viability reducing factor (e.g. Figure 29B). This can be seen as a lower viability of the 70% and 80% PS surfaces than other surfaces with similar roughness values — compare, for instance, the viability of HeLa on 20% and 80% PS surfaces in Figure 29C. These two surfaces have similar S_q, but the 80% PS has a lower viability. The influence of these two surface chemical parameters, polar negative surface energy component and the dispersive surface energy, cannot be decoupled with this data.

The roughness parameter S_q showed the highest cell yield at 6–8 nm, which is an intermediate roughness for these surfaces (Figure 29C). The autocorrelation length indicated, however, that an increase in S_{cl37} resulted in a steep increase in cell counts (Figure 29D). In this case 70% PS, with an intermediate S_q and dispersive surface energy, stood out from the trend. A similar, albeit horizontally mirrored, scatter was obtained for the S_{vk} parameter (Figure 29E) and S_{10z} (data not shown). These could be interpreted in such a way that a higher spacing between features is beneficial for the HeLa cell proliferation, and those features should preferably be peaks rather than valleys. As an exception, however, the 70% PS (with a relatively high viability) is more dominated by valleys, which can be observed by comparing $S_{pk,70\%PS} > S_{vk,70\%}$. Density of summits, S_{ds}, also appeared to be a driving character of this topography (Figure 29F). In this case an increasing S_{ds} increased the viability. Interestingly, this plot appears to include the 70% PS datapoint, but now the 30% PS datapoint stands out from the suggested trend. Interpreted this way, the S_{ds} parameter suggests that a higher number of asperities is preferable for HeLa viability.

To summarise, for a surface with such disordered nanotopography as has been obtained with the latex dispersions used, the surface chemistry appears to have a more pronounced effect on the HeLa proliferation than what was observed for HDF cells. A lower dispersive surface energy resulted in an increased cell proliferation, and a low polar negative surface energy component had a possible reducing effect on proliferation. A low amplitude (S_q), a high lateral roughness (S_{cl37}), and also a high density of asperities (S_{ds}) were beneficial topographical features.

7.5 Nanostructured polymer coatings in a highly tailorable paper-based screening platform

In Paper III, the nanostructured latex coating developed in Paper I and Paper II was utilised in a paper-based screening platform (PBSP). This was a direct development from the previously presented observations on how the properties of the films supported HDF [238] and HeLa cells, as well as *S. aureus* [239], [240]. Utilising the cell proliferation properties of the coating was of particular interest, in the case of HDF cells, a potentially reduced cell stress. Further, the planar design of such a setup would allow for a very high processability, which is not the case for conventional plastic well plates. Three studies were conducted to demonstrate the usability and processability of the paper-based screening platform in cell, materials, and pharmaceutical studies.

7.5.1 Design of the screening platform

The PBSP was developed with paper as a base substrate, onto which the latex dispersion was coated. The platform was based on a system previously developed by Määttänen [173], [174] and Juvonen [175]. Initial tests used a specialty paper for printed functionality as a base substrate. Due to the buckling of the substrate paper in humid conditions necessary for cell culture, a commercially available uncoated paperboard was used instead. A double dispersion coating was needed to obtain an optimum coating quality. This was done with either rod coating or reverse gravure coating technique. Single coating layers often resulted in pinholes that had adverse effects on staining studies, where the pinholes were differently stained by the staining agent, or cell cultures, where microcapillaries would cause the wells to dry. This could also be seen in the barrier tests, where a single layer on the paperboard was a poor barrier for ethanol, even over short periods of time, and an insufficient barrier to vegetable oil or water for a period of 72 h, a typical length of cell studies [241].

Figure 30 — Images of paper-based screening platforms with geometries similar to those of the commercial plastic 24- and 96-well plates. Green and black wax create the matrix of spherical well areas on the paper-based substrate.

The coatings were dried either on-line (roll-to-roll produced reverse gravure coatings) or after coating (rod coated samples). A second drying was done either on-line, during curtain coating, or after a cooling down period, for rod coated samples, to obtain the topography which had been found to stimulate cell growth in Paper I and II. On top of the nanostructured latex-coated paperboard a final layer of either flexographically printed PDMS or wax deposited with a wax printer, was then deposited to provide wetting-directed cell-study areas, the 'wells' (see Figure 30). In this study, the printed well areas had an 8 mm diameter and were aligned in two-column rows. This geometry was based on two factors, the first being that it held a liquid volume that is easily maintained over longer cell studies without evaporation, the second factor the space limitations on the flexographic test printer. In principle, any geometry is possible according to the design of the printing plate. This means that the paper-based screening platform can be made compatible with any plate reader equipment available. PDMS was cured in a short, approximately 30 s, IR heat treatment. This manufacturing process was used for all latex coatings.

Obtaining a reliable readout of the platform was a key consideration during its design. Ideally, a novel platform conforms to current standards and protocols and gives the user value beyond what is obtained with available equipment. Such added value could come from its functionalisability, tunability or other means of on-line measurements, e.g., by electrical means. This means that they should ideally be compatible with optical readers and analysers — i.e., be transparent, or analysable with optical methods — or offer

enough added value to surpass such limits. Further, they should preferably be easy to use without any compromise in accuracy or reliability. Since the used paperboard substrate is opaque, alternatives to optically measuring the viability or proliferation yield had to be considered. In this study a colorimetric approach was chosen, using crystal violet end-point staining to stain the cells in order to correlate the staining intensity to the number of cells. These measurements could be done by imaging the stained substrates with a basic office scanner and using an in-house developed software to detect the well areas and the blue channel RGB intensity in the wells. This approach was tested in three proof-of-concept studies.

7.5.2 The proof-of-concept studies

To prove the usability and utility of this platform three different proof-of-concept studies were performed and compared with common plastic well plates (WP). In the first study, a basic cell growth assay with varying cell numbers was performed on 50% PS surfaces. Glass coverslips were coated with the latex blend, similarly as in Paper I–II, and placed coating side up in the plastic well plates. Both HDF and HeLa cells were used at initial seeding numbers of 0, $1{\cdot}10^3$, $3{\cdot}10^3$, $5{\cdot}10^3$, $10{\cdot}10^3$, $15{\cdot}10^3$, $20{\cdot}10^3$, $30{\cdot}10^3$ and incubated for 24 hours. The readout of the stained PBSP was compared with the readouts from the WPs (Figure 31). These appeared very similar to each other with an increasing detection rate as seeding number increased. In both, a limit of detection could be seen as the lowest cell numbers giving a similar read-out as the blank.

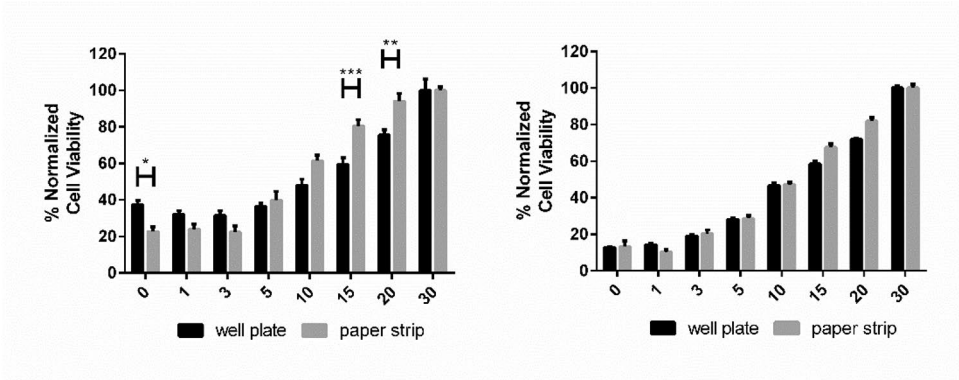

Figure 31 — Comparison of cell viability assays on a commercial well plate and a paper-based screening platform, with a double 50% PS coating. To the left, data for HDF cells, and to the right data for HeLa cells. The number of seeded cells is given as 10^3 (x-axis). Data shows average of 4 repetitions with SEM error of the end-point readout at 24 h. Images reproduced from Paper III with the permission of RSC, the copyright holder.

In the basic viability assay, for both HDF and HeLa cells, an increasing crystal violet readout was detected as the number of seeded cells was increased, both for viability assays done on the PBSP and in WP (Figure 31). The crystal violet stain showed some affinity to the surface itself, which was seen as a false positive readout in the $0{\cdot}10^3$ seeding area. The lowest number of cells that resulted in a significantly stronger coloration than the $0{\cdot}10^3$ level was translated to be the limit of detection. In the case of HDF cells the plastic well plates showed a coffee ring effect around the coated coverslips, which lead to a high background signal for the measurement. As such, numbers of $10{\cdot}10^3$ seeded cells or higher were detectable at levels significantly above the background in the conventional well plate. In contrast, a HDF viability assay done with the PBSP showed a lower level of background, and the detection of $5{\cdot}10^3$ seeded cells was possible above the background level.

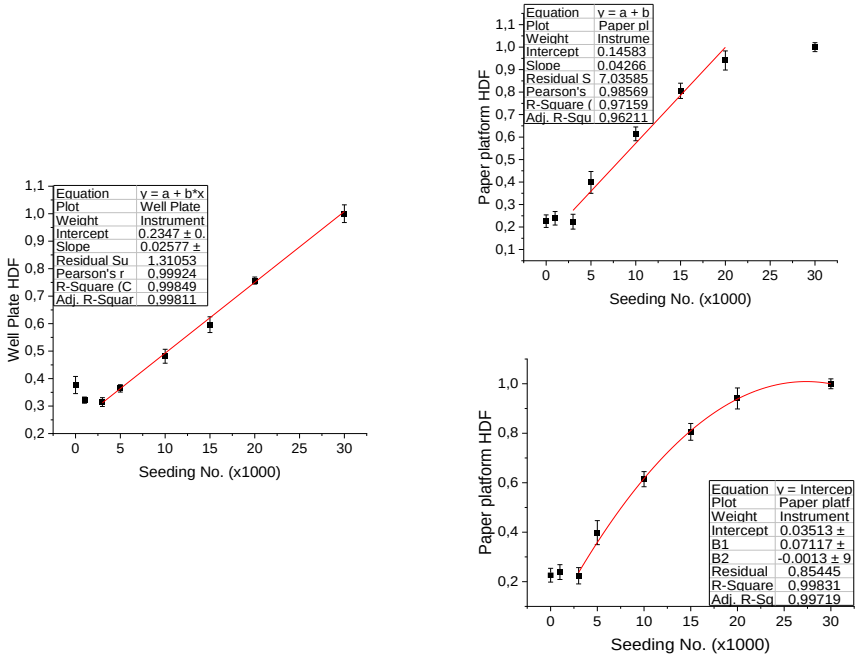

Figure 32 — Detected stained cells at the 24 h endpoint for the commercial well plate (left) and the paper-based screening platform (right). A linear fit is attempted for both experiments; a 2nd order fit yielded better results for the paper-based cell plate (bottom left). The data is normalised to the data point with most cells.

A measure of the reliability of the different assays is the predictability of the response. Comparing the SEM error and standard curves of detection rates for both the PBSP and commercial WP could give a further means to evaluate them. In studies with HDF cells, the error remained rather small for both the WP and PBSP (<0.048) but was slightly higher for the PBSP – average SEM error being 0.033 for the PBSP, respectively 0.021 for the WP. Linear fittings (Figure 32) showed a very good linear fit to the microtiter plate data ($3 \cdot 10^3$ – $30 \cdot 10^3$) with a R^2<0.998 and Pearson's r = 0.999. The PBSP data also showed a reasonably good fit for cell numbers in the range $3 \cdot 10^3$–$20 \cdot 10^3$ (R^2<0.971), but from the next highest to the highest cell counts in the study ($30 \cdot 10^3$) a statistically insignificantly increased readout was observed. The data set ($3 \cdot 10^3$–$30 \cdot 10^3$) appeared to fit a 2nd order fit better (R^2=0.997). This could be an indication of overpopulation within the PBSP wells at the highest cell numbers, either through limited space and/or the liquid media. The first case seems more plausible due to a larger well diameter and preliminary growth area being almost 3.5 times larger in the WP than in the wells of the PBSP. The latter explanation is improbable due to the total volume being deliberately measured to be the same in both the wells of the PBSP and the WP, and since a difference in cell numbers was observed for the corresponding seeding density in the other assay.

Similarly, a cytocompatibility study was done using the PBSP to test its usability in materials studies and demonstrate the tuneability of the surface. In this case two bicomponent high T_g:low T_g latex blends (50:50 blend ratio) from three synthesised latices — two with a high T_g, 100 °C, and one with a low T_g, 16 °C — were tested for their HeLa cell cytocompatibility at five seeding densities (0, $1 \cdot 10^3$, $10 \cdot 10^3$, $20 \cdot 10^3$, $30 \cdot 10^3$; Figure 33). The presence of cells, i.e., a level of cytocompatibility, was detected on both latex blends at the endpoint.

In this case as well, an increased seeding number caused an increased readout. Similarly, to what was seen in the first study, a false positive readout was observed for the blank, caused by the affinity of crystal violet to the latex materials.

There were slight differences between the two investigated surfaces. Firstly, the L01:L02 blend appeared less cytocompatible with low numbers of seeded cells ($1 \cdot 10^3$), where the result was no cells detected. In comparison, at seeding densities of $1 \cdot 10^3$ the L05:L02 blend showed significantly higher number of cells. The measured staining intensity also reached a plateau at $20 \cdot 10^3$ cells on the L01:L02 surface, whereas an increase was still seen at $20 \cdot 10^3$ with the other surface. The difference between the viability of cells grown on the different surfaces could be related to the topographical properties of the two surfaces since their chemical properties were very similar (see Table 6).

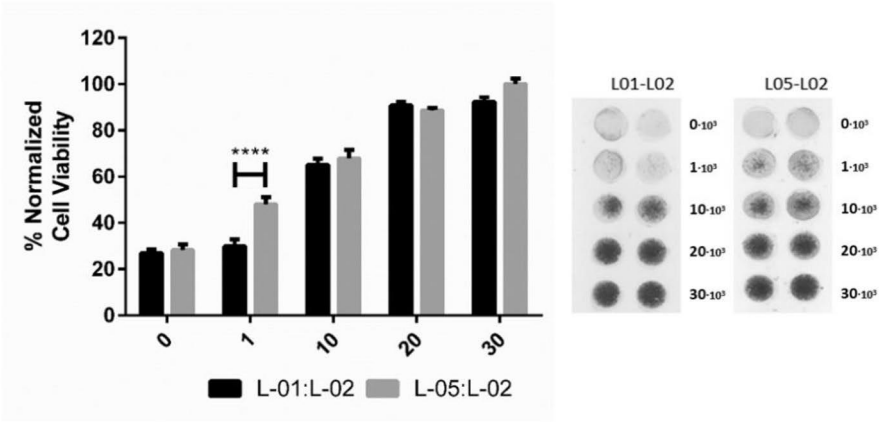

Figure 33 — The normalised cell viability at the end point, tested with varying seeding densities of HeLa cells (left). To the right are scanned images of strips of the paper-based screening platform with L01:L02 (left strip) and L05:L02 (right strip) after cell staining with crystal violet. The number of seeded cells is given as 10^3 (x-axis). The data shows an average of 4 repetitions with SEM error of the end-point readout at 24 h. Images reproduced from Paper III with the permission of RSC, the copyright holder.

The third study was to test the suitability of the PBSP for drug screening and the benefits of using pre-processed drug applications in drug interaction studies. Here, the viability of $30{\cdot}10^3$ HDF or HeLa cells seeded were investigated when cells were grown on the PBSP that had been impregnated by varying concentrations of pipetted or inkjetted doxorubicin (DOX) (Figure 34). In this study, the PBSP coated with the 50% PS blend, which would provide a high cell yield at a low cellular stress level, according to the findings in Paper I. Using ink-jet application the drug loading in the wells of the PBSP was increased by printing an increasing number of layers of DOX solution. The commercial WP study used similar drug concentrations deposited by pipetting. The drug loading in each well was examined using a drug dissolution test to ensure the comparability of different methods of drug loading. The choice to manually pipette DOX into the microtiter wells was done as inkjet printing has limited resolution at long printing ranges due to droplet displacement. Therefore, depositing materials into the well of a well plate, which has walls of typically 14–20 mm height [242], can become inaccurate. In the case of paper-based strips, a modified office printer was used. At concentrations in the range 0.1–5.0 μg mL^{-1}, it was expected that HeLa cell viability would be sharply reduced at these 'therapeutic' doses, but that the non-cancerous HDF cells would survive [243]–[245]. Variations in the cellular viability, using a seeding density of $30{\cdot}10^3$, after the cells had been grown for 24 h in presence of an increasing DOX loading, is shown in Figure 34.

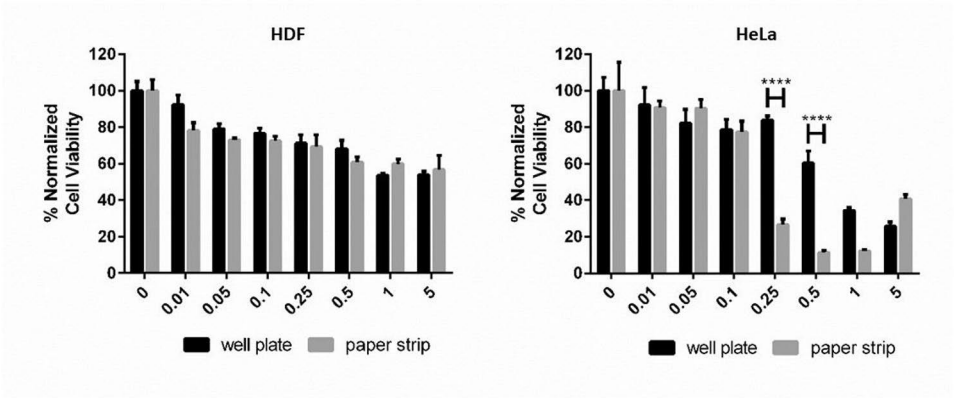

Figure 34 — Changes in viability measured at the end point for HDF (left) and HeLa (right) cells with changes in DOX loading (x-axes, µg mL^{-1}) in the wells. DOX was pipetted into the plastic well plate but printed onto the paper-based screening platform. Images reproduced from Paper III with the permission of RSC, the copyright holder.

The results obtained showed that, indeed, DOX deposited into the wells had a limited effect on the viability of HDF cells, both in the WP experiment, where it was pipetted, and in the PBSP experiment where it was printed. Already small concentrations (0.01 µg mL^{-1}) reduced the viability of these cells with 10–20%. Only concentrations of 1 µg ml^{-1} and above had a larger impact on the viability reducing it to approx. 60%. The results of both the well plate and PBSP studies were very similar. Larger differences between the two parallel studies were observed for the HeLa cells as they were, as expected, more responsive to the drug. Here, low non-therapeutic concentrations (<0.05 µg mL^{-1}) of the drug had a limited effect on the HeLa cells, even lesser than on HDF, reducing the viability to 90% from the blank reference. At 0.1 µg mL^{-1} the viability was at similar levels as the HDF cells at similar drug concentrations (approx. 80%). These observations of the effects of the drug HeLa viability had a larger error than the HDF counterpart, which also indicates a mild responsiveness to the drug at low concentrations. From concentrations of 0.25 µg ml^{-1}, the drug showed a marked effect on the HeLa cells studied on the PBSP by reducing their viability to below 30%. At higher concentrations, the viability was maintained at approximately 40% (5 µg mL^{-1}) or below (0.5–1 µg mL^{-1}). In the WP study, the viability decreased progressively from 0.25 µg mL^{-1}–5 µg mL^{-1}, reaching approximately 30% at lowest. Results from the inkjet-deposited DOX study on the PBSP followed suit with the results for the pipetted study on the PBSP. From 3 to 8 inkjet-printed layers of drug solution, corresponding to approximately 0.2–0.6 µg mL^{-1} concentrations of the drug, according to the standard curves obtained, the HeLa cell viability decreased

significantly to approx. 10% of the viability of the reference sample. This was a much quicker decline than what was observed for the well plate data infused with pipetted doxorubicin. The decline was non-linear, as was also seen for the pipetted data. This could indicate a more complicated response mechanism to the drug, or an activity change of the pipetted drug [246].

7.5.3 Further developments of the tailorable platform

As shown in S. Paper II, the nanostructured surface can be constructed to provide structures on different length scales. In the study, a layer of the 50% PS dispersion was cast onto template surfaces, i.e. lithographically patterned AFM calibration grids. When peeled off, the resulting surfaces had not only the inherent nanostructure of the latex blend, but also step heights provided by the calibration grid. Four different step heights in the range 1.8 μm–104 μm were manufactured. Incorporating such structures into the cell culture areas or using such films as a base for diagnostic plates would allow for new ways of manufacturing topological features that can stimulate cell behaviour while studying them directly. This possibility was underlined by the very promising optical character of the surface films. Rewetted films had an 80 % transparency measured with UV-vis, and ultra-thin (20 nm) Au electrodes deposited on them still maintained 50% transparency. Such semi-transparent electrodes would allow for stimulating or measuring the cellular activity, for instance with electrochemical impedance spectroscopy (EIS) or cyclic voltammetry, while optical measurements are performed [247]–[249]. The long-term stability of the electrodes was also confirmed.

Using EIS to measure cells with different electrodes deposited on the nanostructured latex coatings with different support materials was briefly investigated with HDF and HeLa cells. The method has been widely explored and proven a useful tool in biology many times over [250], e.g. for measuring singular cells [251] or discriminating between cancerous and non-cancerous cells [192], [252], just to name a few.

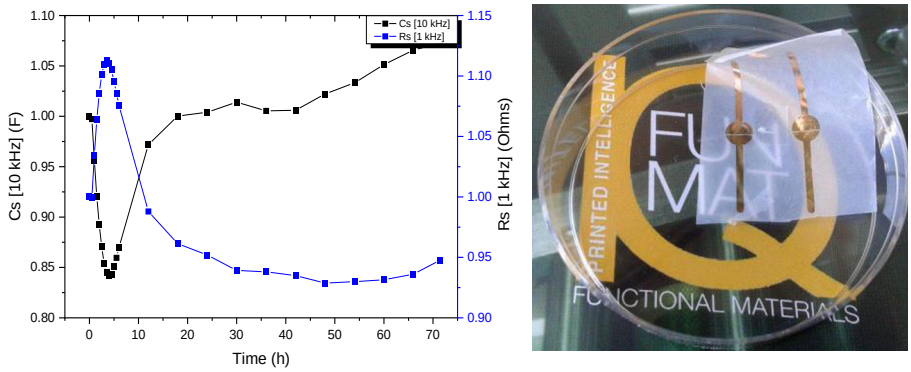

Figure 35 — Left: Typical EIS spectra showing the capacitance (black, f = 10 kHz) and resistivity (blue, f = 1 kHz) of HDF cells attaching and spreading on a 20 nm thick Au electrode film on a nanostructured latex-coated paper. Previously unpublished data. Right: The 20 nm Au electrodes deposited on a layer of nanostructured latex peeled off a paper substrate.

Impedance measurements of cell cultures utilise an alternating current with varying frequency passing over the electrodes to study the electrical properties of the cells or a biofilm at a single time-point or as changes with time. Different frequencies interact differently with the materials on or in proximity with the electrodes, e.g., the biofilm, the ECM or the cell media, and thus characterises different aspects of them. In Figure 35, an example curve of data was obtained with EIS of HDF cells attaching on a two-electrode system of gold on the nanostructured latex film. In this case the capacitance, measured at 10 kHz, and the resistance, measured at 1 kHz, changed as the cell population approached the surface, from the seeding time-point (t=0), to attach (up to ca 5h) and spread (t> 5h). This shows an example of how the different phases of the cultured cells can be observed with the technique.

7.5.4 Concluding remarks on the paper-based screening platform

In this section, the use of an opaque, low-cost and paper-based platform was shown to be a valid alternative to commercial plastic microtiter plates in colorimetric cell studies. Even through such a simple tool as an office scanner was used to get a cell readout, a result of similar quality to that obtained with costly high-end instruments was obtained. This shows that the paper-based platform can well be ASSURED ("Affordable, Sensitive, Specific, User-friendly, Rapid and robust, Equipment-free and Deliverable to end-users"), as the World Health Organisation has called for diagnostic devices to be [179]. Such tools could provide new healthcare and diagnosis methods in areas with poor infrastructure or limited resources, or could even be used as educational tools at any level [253].

The main benefits of using a planar platform are the processability and tuneability that it brings to the researchers' table. Using large-scale manufacturing methods to obtain different coatings or to deposit drugs means these can quickly be compared and screened for their responses with cell lines. The processing of known hazardous chemicals or novel compounds is associated with potential health risks, as was the case with doxorubicin in the study [254]. Therefore, automated processing not only reduces the risk of human error, but also the risks for the researcher. The processability also allows for tailoring the properties of the surfaces that cells are to be grown on. This could mean applying a surface like the material that is to be studied to the bottom of the cell culture, providing the possibility to study cell-surface interactions on it without losing any experimental tools. Another valuable approach would be tuning the surface properties to exhibit properties that are most natural, or suitable for a specific cell line of interest. This could give data that are more representative of the cells in their natural state.

Added value could be obtained by manufacturing the platform on a transparent support, or developing it as a self-supported platform, e.g., by casting. This would allow for both a direct optical study of the cultures and to give the platform hierarchically structured surface features and would thereby provide further tools for studies involving cellular interactions with various surface features. Similarly, electrode systems could be readily included into the wells for the detection of adsorption of proteins, cells or even metabolites or to stimulate the cells or bacteria grown on it. Such options, especially at a low-cost, are not currently widely available on the market.

8. Conclusions and outlook

In this thesis nanostructured surfaces were manufactured by coating PS and ABS latex dispersions onto borosilicate glass coverslips and paperboard. The varying mixing blend ratio of these high T_g and low T_g latices caused differences in topography, surface chemistry and wetting on the prepared coatings. Variations in protein deposition depending on the blend ratio were observed (S. Paper I). When used in studies of microbial (*S. aureus*) (Paper II) and mammalian cells (HDF and HeLa), variations in some biological parameters were observed (Paper I). These included differences in colony numbers, PNAG expression and protein abundances for *S. aureus*, and the relative cell number (viability for the mammalian cells). In HDF cells, variations in stress fibre formation were also observed. Finally, the manufactured surfaces were deployed as a base for a cell study plate, to test the reliability and versatility of a paper-based platform in basic cell culture, materials studies and pharmaceutical studies (Paper III). Hierarchical structures and electrode applications with promising optical character were also tested using latex as self-supported films (S. Paper II).

The surfaces used were mostly hydrophilic, but the highest PS% ratios decreased, and ultimately cancelled the hydrophilic character. The surfaces also showed a decreased polar negative character, and for 100% PS surfaces it was negligible. The dispersive surface energy component of the surfaces, and thereby also the total surface energy, decreased slightly at close to equal blend ratios. Topographically the roughness increased as the PS% ratio was increased, reaching a maximum at near-equal blend ratios. The topography of the surfaces shifted from being peak dominated at low PS% content to being valley dominated for high PS% surfaces. The substrate on which the surfaces were manufactured on was also observed to have some influence on roughness.

Protein adsorption was observed to vary with PS content of the films, in S. Paper I. Depending on the proteins studied, the protein adsorption appeared also to differ between PS regions (peaks) and ABS regions (valleys). Differences in protein activity were also observed. Such differences were contributed to local variations in the surface chemistry and the topography.

In Paper II it was shown that 24 h *S. aureus* biofilms were able to respond to nanoscale features of the surfaces. Differences were seen in colony densities and PNAG detection, representing viability and microbial stress, which appeared to vary depending on which nanostructured film they were grown. The biofilms responded to different surface properties depending on which assay was used. For instance, the surface energy did not appear to influence the biofilms in the microtiter plate assay, but it did so in the agar plate assay.

Variations in the detected amounts of PNAG in the biofilms did not directly correlate with the viability. This indicated that the PNAG amount was indeed a response to the surface properties. An interesting observation was that a set of parameters could be combined to form a rudimentary 'model', that appeared to connect a surface chemistry parameter and two topographical parameters to the viability and PNAG detection responses. This is of interest as previous attempts have focussed on describing the adhesive behaviour of cells using, e.g., DLVO-based approaches which specifically describe adhesion of a particle to a surface. This suggests that microbial responses over longer times could be estimated based on the surface properties of materials.

Further, in Paper II, changes in the protein abundances were also correlated for several of the proteins in the *S. aureus* surfaceome. The protein numbers and abundances depended on the assay used. Overall, the results in Paper II show that the bacteria respond to nanoscale differences of the surface they attach to and, depending on the assay used, also to the surface chemistry. Indeed, the assays used for studies of this type should be chosen with care as this could significantly alter the response observed for, e.g., studied novel biomaterials. Phenotype changes for attaching bacteria have previously been observed [89]. The fact that these can be correlated to surface properties was a completely new observation brought forward through the studies in this thesis. This observation is made more interesting by the fact that these phenotypic changes could be related to the pathogenicity, virulence, and host immune system evasion. If possible, materials that inhibit such responses could be very beneficial for preventing the spread of diseases, e.g., via medical devices.

Similarly, responses to the nanoscale topography of the surfaces were seen for mammalian HDF and HeLa cells in Paper I. HDF cells appeared to benefit from an increased roughness, especially a larger effective surface area and height variations, which can generally be described as 'rougher' surfaces. Comparing viabilities on peak dominated surfaces and valley dominated surfaces showed no difference for the geometries used here. Interestingly, the data shows that HeLa cells respond to very different surface properties than the HDF cells. The HDF cells were also expressing less stress fibres (vimentin and actin) on the surfaces associated with a higher viability. This could indicate that surfaces of this type are a more beneficial growth environment for the cell line.

In Paper III the nanoscale surface was successfully deployed in a paper-based cell culture platform. The planar design of the platform enabled free modification of the surface for investigating prefabricated drug dosage in the wells, a symbol of pharmaceutical studies, or even using another biofunctional coating. The reliability of the platform was compared to a commercial microtiter plate, and it showed equal performance on many levels, especially considering that it required no expensive diagnostics equipment to be

analysed. Similarly, using a functionalised base could have its benefits, as this is something that is difficult to do in the plastic well plate base. A drawback of the paper-based platform is the lack of transparency, which would enable optical imaging. This could be overcome by using a transparent base but might come at the price of the eco-friendliness associated with paper.

S. Paper II showed some interesting potential lines of further research, and potential features that could be added to the tailorable paper-based cell culture and diagnostics platform. Casting methods were shown to provide nanoscale grooves while retaining the nanostructure, giving a true hierarchical structure to the coating. This was also possible to achieve on free standing latex films. Transparent electrodes were also developed on the nanostructured paper, which could enable electrical read-outs, using ECIS, e.g., or the detection of metabolites, pH etc. during cell culture. This is also a possible means to overcome the transparency issue.

The question remains, if a unifying theory can be devised to explain bacterial and mammalian cell responses to surface properties. These processes are very intricate and involve interactions of countless biochemical species, in a constantly reactive and dynamic relationship. An issue with individual observations is that they can easily become irrevocably anecdotal if a), the surfaces are not thoroughly reported both physically and chemically and b), the biological responses are not broadly investigated. This could be mediated by defining standards which must be reported. Broadly reported results can then be more readily used in meta-reports and big data analysis.

9. Acknowledgments

I still remember how warmly I was welcomed was when I came to Physical Chemistry to do my Master's degree 2012. Professor Jouko Peltonen took me in to a project looking to enhance the membrane filtration of wastewater. For a student that had only seen the theoretical side of science it was a blast working putting things into practice. With such a beginning to my research work, it was easy to say 'yes', 'please' and 'thank you' when the opportunity arose to join the Functional Materials at the Biological Interfaces Centre of Excellence project in 2015. This set me on the path of a Ph.D. candidate and set, also, the title on the front page.

Thank you, Jouko, for your guidance, advice, support, and your always open door throughout these years. Few can rely on such careful revisions time after time.

Adjunct Professor Petri Ihalainen, you showed the value of a researcher's focussed drive. Thank you for your help to put my research work in motion and giving it perspective.

I also want to thank Professor Elena Martínez for taking on the role as my opponent. I am looking forward to our discussion — will surely be constructive. I am also very grateful for the time Professor Per M. Claesson and Professor Tapani Viitala took to pre-examine my thesis and all their positive comments.

My fellows in FunMat, both senior and junior, working with each one of you was great. Professor Ronald Österbacka, thank you for leading a warm environment for us to grow in and explore. Erik, you shaped this journey like no other. It has been great; it has been intense. We have shared so many invaluable lessons. Arun, thank you for your help, your explanations, and your curiosity.

Paola, you made the last chapter possible! Always easy to work with you and to turn over all stones. Thank you! You too, Professor Adyary Fallarero, for all the constructive feedback you gave during our study.

Everyone whom I have worked with at FyKe, thank you for the togetherness we have made. Anni, Björn, and Helka – thank you for all you have taught me. I am grateful Jan-Henrik for you letting me in on the side-quests. Gun, you made so many things easier for a youngling to navigate. Your ceaseless efforts, Kena, to make sure all the machinery ticks. Miraculously, it always does. Teaching team, I appreciate how you are always welcoming to my ideas.

All other colleagues, I feel privileged for having had the opportunity to meet you and work with you. You keep showing me science from so many points of view. Anna and Johan, you fluoresce as you make work equal play. (This is surprisingly often necessary during a Ph.D.)

Friends, ready take me away when need be, even to places unfathomable. With you there is always something to be happy about. Thank you for being around.

My family, mum and dad. You're always there and have always let me take my own path. I cannot ask for more.

Maiju, maybe this time they let me leave you a message in the acknowledgments. You are an absolute belter — thank you. :◊

The financial support of this work, granted by Svenska Kulturfonden, Waldemar von Frenckells Stiftelse, Tor, Joe och Pentti Borgs Minnesfond, Åbo Akademi University and the Jane and Aatos Erkko Foundation is greatly appreciated.

Through you all I have learned so much. With you all I hope to learn so much more.

Emil Rosqvist
Åbo, October 2021

10. Bibliography

[1] M. S. Dodd *et al.*, 'Evidence for early life in Earth's oldest hydrothermal vent precipitates', *Nature*, vol. 543, no. 7643, pp. 60–64, Mar. 2017, doi: 10.1038/nature21377.

[2] S. Doron and S. Gorbach, 'Bacterial Infections: Overview', *Int. Encycl. Public Health*, pp. 273–282, 2008, doi: 10.1016/B978-012373960-5.00596-7.

[3] Y. Li, X. Yin, and L. Changsheng, 'The Horizon of Materiobiology: A Perspective on Material-Guided Cell Behaviors and Tissue Engineering', *Chem. Rev.*, vol. 117, no. 5, pp. 4376–4421, 2017, doi: 10.1021/acs.chemrev.6b00654.

[4] S. R. Heidemann, '1 - The Molecular and Cellular Bases of Physiological Regulation', in *Cunningham's Textbook of Veterinary Physiology (Sixth Edition)*, B. G. Klein, Ed. St. Louis (MO): W.B. Saunders, 2020, pp. 1–28. doi: 10.1016/B978-0-323-55227-1.00001-6.

[5] J. Vitte, A. M. Benoliel, A. Pierres, and P. Bongrand, 'Is there a predictable relationship between surface physical-chemical properties and cell behaviour at the interface?', *Eur. Cell. Mater.*, vol. 7, pp. 52–63; discussion 63, Jun. 2004, doi: 10.22203/ecm.v007a06.

[6] B. Bhushan, 'Surface roughness analysis and measurement techniques', 2000, pp. 49–119.

[7] D. J. Whitehouse, *Handbook of Surface and Nanometrology*, 2nd ed. Boca Raton, Florida, US: CRC Press, 2010.

[8] D. Whitehouse, '3 - Profile and areal (3D) parameter characterization', in *Surfaces and Their Measurement*, D. Whitehouse, Ed. Oxford: Kogan Page Science, 2002, pp. 48–95. doi: 10.1016/B978-190399601-0/50003-7.

[9] OverlordQ, 'Atomic force microscope block diagram.svg - Wikimedia Commons'. https://commons.wikimedia.org/wiki/File:Atomic_force_microscope_block_diagram.svg (accessed May 13, 2021).

[10] H. Zahouani, R. Vargiolu, P. Kapsa, J. L. Loubet, and T. G. Mathia, 'Effect of lateral resolution on topographical images and three-dimensional functional parameters', *Wear*, vol. 219, no. 1, pp. 114–123, 1998, doi: https://doi.org/10.1016/S0043-1648(98)00235-X.

[11] A. Méndez-Vilas, J. M. Bruque, and M. L. González-Martín, 'Sensitivity of surface roughness parameters to changes in the density of scanning points in multi-scale AFM studies. Application to a biomaterial surface', *Ultramicroscopy*, vol. 107, no. 8, pp. 617–625, 2007, doi: https://doi.org/10.1016/j.ultramic.2006.12.002.

[12] P. J. Ramón-Torregrosa, M. A. Rodríguez-Valverde, A. Amirfazli, and M. A. Cabrerizo-Vílchez, 'Factors affecting the measurement of roughness factor of surfaces and its implications for wetting studies', *Colloids Surf. Physicochem. Eng. Asp.*, vol. 323, no. 1, pp. 83–93, 2008, doi: https://doi.org/10.1016/j.colsurfa.2007.10.032.

[13] D. L. Sedin and K. L. Rowlen, 'Influence of tip size on AFM roughness measurements', *Appl. Surf. Sci.*, vol. 182, no. 1, pp. 40–48, 2001, doi: https://doi.org/10.1016/S0169-4332(01)00432-9.

[14] J. Shen, D. Zhang, F.-H. Zhang, and Y. Gan, 'AFM tip-sample convolution effects for cylinder protrusions', *Appl. Surf. Sci.*, vol. 422, pp. 482–491, 2017, doi: https://doi.org/10.1016/j.apsusc.2017.06.053.

[15] 'SecretDisc', *View of cantilever in Atomic Force Microscope (magnification 1000x)*. 2009. Accessed: May 14, 2021. [Online]. Available: https://commons.wikimedia.org/wiki/File:AFM_(used)_cantilever_in_Scanning_Electron_Microscope,_magnification_1000x.JPG

[16] 'Creative Commons — Attribution-ShareAlike 3.0 Unported — CC BY-SA 3.0'. https://creativecommons.org/licenses/by-sa/3.0/deed.en (accessed May 14, 2021).

[17] E. Nagao and J. A. Dvorak, 'Phase Imaging by Atomic Force Microscopy: Analysis of Living Homoiothermic Vertebrate Cells', *Biophys. J.*, vol. 76, no. 6, pp. 3289–3297, Jun. 1999, doi: 10.1016/S0006-3495(99)77481-3.

[18] D. Alsteens, H. E. Gaub, R. Newton, M. Pfreundschuh, C. Gerber, and D. J. Müller, 'Atomic force microscopy-based characterization and design of biointerfaces', *Nat. Rev. Mater.*, vol. 2, no. 5, p. 17008, Mar. 2017, doi: 10.1038/natrevmats.2017.8.

[19] S. Maghsoudy-Louyeh, M. Kropf, and B. Tittmann, 'Review of Progress in Atomic Force Microscopy', *Open Neuroimaging J.*, vol. 12, pp. 86–104, Dec. 2018, doi: 10.2174/1874440001812010086.
[20] T. J. Young, M. A. Monclus, T. L. Burnett, W. R. Broughton, S. L. Ogin, and P. A. Smith, 'The use of the PeakForce™ quantitative nanomechanical mapping AFM-based method for high-resolution Young's modulus measurement of polymers', *Meas. Sci. Technol.*, vol. 22, no. 12, p. 125703, Oct. 2011, doi: 10.1088/0957-0233/22/12/125703.
[21] S. Badger, 'Bruker's PeakForce Tapping AFM Mode in >4,000 Papers', *Blue Scientific*, Dec. 06, 2019. https://www.blue-scientific.com/bruker-peakforce-tapping-afm-mode/ (accessed May 14, 2021).
[22] V. Panchal, R. Pearce, R. Yakimova, A. Tzalenchuk, and O. Kazakova, 'Standardization of surface potential measurements of graphene domains', *Sci. Rep.*, vol. 3, no. 1, p. 2597, Sep. 2013, doi: 10.1038/srep02597.
[23] H. Si *et al.*, 'Emerging Conductive Atomic Force Microscopy for Metal Halide Perovskite Materials and Solar Cells', *Adv. Energy Mater.*, vol. 10, no. 10, p. 1903922, Mar. 2020, doi: 10.1002/aenm.201903922.
[24] T. Hassenkam, M. P. Andersson, K. N. Dalby, D. M. A. Mackenzie, and M. T. Rosing, 'Elements of Eoarchean life trapped in mineral inclusions', *Nature*, vol. 548, no. 7665, pp. 78–81, Aug. 2017, doi: 10.1038/nature23261.
[25] M. Cosentino, C. Canale, P. Bianchini, and A. Diaspro, 'AFM-STED correlative nanoscopy reveals a dark side in fluorescence microscopy imaging', *Sci. Adv.*, vol. 5, no. 6, p. eaav8062, Jun. 2019, doi: 10.1126/sciadv.aav8062.
[26] 'ISO - International Organization for Standardization', *ISO*. https://www.iso.org/home.html (accessed Jun. 17, 2021).
[27] F. Blateyron, 'The Areal Field Parameters', in *Characterisation of Areal Surface Texture*, 2013, pp. 15–43. doi: 10.1007/978-3-642-36458-7_2.
[28] J. F. Jørgensen, 'SPIP User's Guide, 6th Ed'. Image Metrology A/S. Accessed: Feb. 17, 2021. [Online]. Available: http://www.imagemet.com/WebHelp6/Default.htm
[29] K. N. Hansson and S. Hansson, 'Skewness and Kurtosis: Important Parameters in the Characterization of Dental Implant Surface Roughness—A Computer Simulation', *ISRN Mater. Sci.*, vol. 2011, p. 305312, Oct. 2011, doi: 10.5402/2011/305312.
[30] Y. Li *et al.*, 'Measuring the Autocorrelation Function of Nanoscale Three-Dimensional Density Distribution in Individual Cells Using Scanning Transmission Electron Microscopy, Atomic Force Microscopy, and a New Deconvolution Algorithm', *Microsc. Microanal. Off. J. Microsc. Soc. Am. Microbeam Anal. Soc. Microsc. Soc. Can.*, vol. 23, no. 3, pp. 661–667, Jun. 2017, doi: 10.1017/S1431927617000447.
[31] K. Żak and W. Grzesik, 'Metrological Aspects of Surface Topographies Produced by Different Machining Operations Regarding Their Potential Functionality', *Metrol. Meas. Syst.*, vol. 24, 2017, doi: 10.1515/mms-2017-0027.
[32] R. J. Crawford, H. K. Webb, V. K. Truong, J. Hasan, and E. P. Ivanova, 'Surface topographical factors influencing bacterial attachment', *Adv. Colloid Interface Sci.*, vol. 179–182, pp. 142–149, 2012, doi: https://doi.org/10.1016/j.cis.2012.06.015.
[33] S. K. Rhee, 'A method for determining surface energies of solids: Temperature-variant contact angle method', *Mater. Sci. Eng.*, vol. 16, no. 1, pp. 45–51, 1974, doi: https://doi.org/10.1016/0025-5416(74)90136-0.
[34] J.-C. Joud, M.-G. Barthés-Labrousse, and M.-G. Barthés-Labrousse, *Physical Chemistry and Acid-Base Properties of Surfaces*. Newark, NJ, UNITED STATES: John Wiley & Sons, Incorporated, 2015. [Online]. Available: http://ebookcentral.proquest.com/lib/abo-ebooks/detail.action?docID=4323067
[35] C. J. Van Oss, M. K. Chaudhury, and R. J. Good, 'Interfacial Lifshitz-van der Waals and polar interactions in macroscopic systems', *Chem. Rev.*, vol. 88, no. 6, pp. 927–941, Sep. 1988, doi: 10.1021/cr00088a006.
[36] C. J. V. Oss, R. J. Good, and M. K. Chaudhury, 'The role of van der Waals forces and hydrogen bonds in "hydrophobic interactions" between biopolymers and low energy surfaces', *J. Colloid Interface Sci.*, vol. 111, no. 2, pp. 378–390, 1986, doi: https://doi.org/10.1016/0021-9797(86)90041-X.

[37] T. Young, 'III. An essay on the cohesion of fluids', *Philos. Trans. R. Soc. Lond.*, vol. 95, pp. 65–87, 1805, doi: 10.1098/rstl.1805.0005.
[38] T. Huhtamäki, X. Tian, J. Korhonen, and R. Ras, 'Surface-wetting characterization using contact-angle measurements', *Nat. Protoc.*, vol. 13, 2018, doi: 10.1038/s41596-018-0003-z.
[39] A. Marmur, 'Equilibrium contact angles: theory and measurement', *Colloids Surf. Physicochem. Eng. Asp.*, vol. 116, no. 1, pp. 55–61, 1996, doi: https://doi.org/10.1016/0927-7757(96)03585-6.
[40] A. Marmur, 'Solid-Surface Characterization by Wetting', *Annu. Rev. Mater. Res.*, vol. 39, no. 1, pp. 473–489, 2009, doi: 10.1146/annurev.matsci.38.060407.132425.
[41] J. N. Israelachvili, '17 - Adhesion and Wetting Phenomena', in *Intermolecular and Surface Forces (Third Edition)*, Third Edition., J. N. Israelachvili, Ed. San Diego: Academic Press, 2011, pp. 415–467. doi: 10.1016/B978-0-12-375182-9.10017-X.
[42] J. N. Israelachvili, '10 - Unifying Concepts in Intermolecular and Interparticle Forces', in *Intermolecular and Surface Forces (Third Edition)*, Third Edition., J. N. Israelachvili, Ed. San Diego: Academic Press, 2011, pp. 191–204. doi: 10.1016/B978-0-12-375182-9.10010-7.
[43] E. A. Vogler, 'Protein adsorption in three dimensions', *Biomaterials*, vol. 33, no. 5, pp. 1201–1237, 2012, doi: https://doi.org/10.1016/j.biomaterials.2011.10.059.
[44] R. N. Wenzel, 'Resistance of solid surfaces to wetting by water', *Ind. Eng. Chem.*, vol. 28, no. 8, pp. 988–994, Aug. 1936, doi: 10.1021/ie50320a024.
[45] J. Peltonen, M. Järn, S. Areva, M. Linden, and J. B. Rosenholm, 'Topographical Parameters for Specifying a Three-Dimensional Surface', *Langmuir*, vol. 20, no. 22, pp. 9428–9431, Oct. 2004, doi: 10.1021/la0400252.
[46] A. B. D. Cassie, 'Contact angles', *Discuss Faraday Soc*, vol. 3, no. 0, pp. 11–16, 1948, doi: 10.1039/DF9480300011.
[47] T. Darmanin and F. Guittard, 'Superhydrophobic and superoleophobic properties in nature', *Mater. Today*, vol. 18, no. 5, pp. 273–285, 2015, doi: https://doi.org/10.1016/j.mattod.2015.01.001.
[48] L. Gao and T. McCarthy, 'An Attempt to Correct the Faulty Intuition Perpetuated by the Wenzel and Cassie "Laws"', *Langmuir ACS J. Surf. Colloids*, vol. 25, pp. 7249–55, Jul. 2009, doi: 10.1021/la901416m.
[49] M. V. Panchagnula and S. Vedantam, 'Comment on How Wenzel and Cassie Were Wrong by Gao and McCarthy.', *Langmuir ACS J. Surf. Colloids*, vol. 23, no. 26, pp. 13242; discussion 13243, Dec. 2007, doi: 10.1021/la7022117.
[50] L. Makkonen, 'Faulty Intuitions of Wetting', *Int. J. Wettability Sci. Technol.*, vol. 1, no. 1, pp. 13–30, 2018.
[51] N. Shardt and J. A. W. Elliott, 'Gibbsian Thermodynamics of Wenzel Wetting (Was Wenzel Wrong? Revisited).', *Langmuir ACS J. Surf. Colloids*, vol. 36, no. 1, pp. 435–446, Jan. 2020, doi: 10.1021/acs.langmuir.9b02984.
[52] G. McHale, 'Cassie and Wenzel: Were They Really So Wrong?', *Langmuir*, vol. 23, no. 15, pp. 8200–8205, Jul. 2007, doi: 10.1021/la7011167.
[53] L. Gao and T. J. McCarthy, 'How Wenzel and Cassie Were Wrong', *Langmuir*, vol. 23, no. 7, pp. 3762–3765, Mar. 2007, doi: 10.1021/la062634a.
[54] C. D. Volpe, D. Maniglio, M. Brugnara, S. Siboni, and M. Morra, 'The solid surface free energy calculation: I. In defense of the multicomponent approach', *J. Colloid Interface Sci.*, vol. 271, no. 2, pp. 434–453, 2004, doi: https://doi.org/10.1016/j.jcis.2003.09.049.
[55] S. Siboni, C. D. Volpe, D. Maniglio, and M. Brugnara, 'The solid surface free energy calculation: II. The limits of the Zisman and of the "equation-of-state" approaches', *J. Colloid Interface Sci.*, vol. 271, no. 2, pp. 454–472, 2004, doi: https://doi.org/10.1016/j.jcis.2003.09.050.
[56] D. Y. Kwok and A. W. Neumann, 'Contact angle measurement and contact angle interpretation', *Adv. Colloid Interface Sci.*, vol. 81, no. 3, pp. 167–249, 1999, doi: https://doi.org/10.1016/S0001-8686(98)00087-6.

[57] D. Y. Kwok, D. Li, and A. W. Neumann, 'Evaluation of the Lifshitz-van der Waals/Acid-Base Approach To Determine Interfacial Tensions', *Langmuir*, vol. 10, no. 4, pp. 1323–1328, Apr. 1994, doi: 10.1021/la00016a057.
[58] D. K. Owens and R. C. Wendt, 'Estimation of the surface free energy of polymers', *J. Appl. Polym. Sci.*, vol. 13, no. 8, pp. 1741–1747, 1969, doi: https://doi.org/10.1002/app.1969.070130815.
[59] D. H. Kaelble, 'Dispersion-Polar Surface Tension Properties of Organic Solids', *J. Adhes.*, vol. 2, no. 2, pp. 66–81, 1970, doi: 10.1080/0021846708544582.
[60] W. Rabel, 'Einige Aspekte der Benetzungstheorie und ihre Anwendung auf die Untersuchung und Veränderung der Oberflächeneigenschaften von Polymeren', *Farbe Lack*, vol. 77, no. 10, pp. 997–1005, 1971.
[61] S. Wu and K. J. Brzozowski, 'Surface free energy and polarity of organic pigments', *J. Colloid Interface Sci.*, vol. 37, no. 4, pp. 686–690, 1971, doi: https://doi.org/10.1016/0021-9797(71)90347-X.
[62] S. Wu, 'Polar and Nonpolar Interactions in Adhesion', *J. Adhes.*, vol. 5, no. 1, pp. 39–55, 1973, doi: 10.1080/00218467308078437.
[63] F. Thomsen, 'Practical Contact Angle Measurement, Krüss Technical Note TN315e'. Krüss Scientific, Dec. 2008. Accessed: Feb. 19, 2021. [Online]. Available: https://warwick.ac.uk/fac/cross_fac/sciencecity/programmes/internal/themes/am2/booking/dropshapeanalyser/practical_contact_angle_measurement_5.pdf
[64] D. R. Absolom, F. V. Lamberti, Z. Policova, W. Zingg, C. J. van Oss, and A. W. Neumann, 'Surface thermodynamics of bacterial adhesion', *Appl. Environ. Microbiol.*, vol. 46, no. 1, pp. 90–97, Jul. 1983, doi: 10.1128/AEM.46.1.90-97.1983.
[65] A. Vilinska and K. Rao, 'Surface thermodynamics and extended DLVO theory of Leptospirillum ferrooxidans cells' adhesion on sulfide minerals', *Miner. Metall. Process.*, vol. 28, pp. 151–158, 2011, doi: 10.1007/BF03402248.
[66] D. F. Parsons, R. B. Walsh, and V. S. J. Craig, 'Surface forces: Surface roughness in theory and experiment', *J. Chem. Phys.*, vol. 140, no. 16, p. 164701, 2014, doi: 10.1063/1.4871412.
[67] M. Götzinger and W. Peukert, 'Particle Adhesion Force Distributions on Rough Surfaces', *Langmuir*, vol. 20, no. 13, pp. 5298–5303, Jun. 2004, doi: 10.1021/la049914f.
[68] M. Hermansson, 'The DLVO theory in microbial adhesion', *Colloids Surf. B Biointerfaces*, vol. 14, no. 1, pp. 105–119, 1999, doi: https://doi.org/10.1016/S0927-7765(99)00029-6.
[69] S. Bayoudh, A. Othmane, L. Mora, and H. B. Ouada, 'Assessing bacterial adhesion using DLVO and XDLVO theories and the jet impingement technique', *Colloids Surf. B Biointerfaces*, vol. 73, no. 1, pp. 1–9, 2009, doi: https://doi.org/10.1016/j.colsurfb.2009.04.030.
[70] N. V. Churaev, 'The DLVO theory in Russian colloid science', *Adv. Colloid Interface Sci.*, vol. 83, no. 1, pp. 19–32, 1999, doi: https://doi.org/10.1016/S0001-8686(98)00067-0.
[71] P. C. Hiemenz and R. B. Perry, 'Principles of Colloid and Surface Chemistry, Second Edition', *J. Chem. Educ.*, vol. 64, no. 12, p. A328, Dec. 1987, doi: 10.1021/ed064pA328.3.
[72] R. Bos, H. C. van der Mei, and H. J. Busscher, 'Physico-chemistry of initial microbial adhesive interactions – its mechanisms and methods for study', *FEMS Microbiol. Rev.*, vol. 23, no. 2, pp. 179–230, Apr. 1999, doi: 10.1111/j.1574-6976.1999.tb00396.x.
[73] G. Malescio, 'Intermolecular potentials — past, present, future', *Nat. Mater.*, vol. 2, no. 8, pp. 501–503, Aug. 2003, doi: 10.1038/nmat949.
[74] Larryisgood, *A Diagram of the electrical double layer that forms at the surface of a charged particle*. 2011. Accessed: Jun. 22, 2021. [Online]. Available: https://commons.wikimedia.org/wiki/File:Double_Layer.png
[75] J. N. Israelachvili, '21 - Interactions of Biological Membranes and Structures', in *Intermolecular and Surface Forces (Third Edition)*, Third Edition., J. N. Israelachvili, Ed. San Diego: Academic Press, 2011, pp. 577–616. doi: 10.1016/B978-0-12-375182-9.10021-1.
[76] J. N. Israelachvili, 'Chapter 13 - Van der Waals Forces between Particles and Surfaces', in *Intermolecular and Surface Forces (Third Edition)*, Third Edition., J. N. Israelachvili, Ed.

San Diego: Academic Press, 2011, pp. 253–289. doi: 10.1016/B978-0-12-375182-9.10013-2.

[77] Y. Rabinovich, J. J. Adler, A. Ata, R. Singh, and B. Moudgil, 'Adhesion between nanoscale rough surfaces. I. Role of asperity geometry', *J. Colloid Interface Sci.*, vol. 232, pp. 10–16, 2000.

[78] Y. Cheng, G. Feng, and C. I. Moraru, 'Micro- and Nanotopography Sensitive Bacterial Attachment Mechanisms: A Review.', *Front. Microbiol.*, vol. 10, p. 191, 2019, doi: 10.3389/fmicb.2019.00191.

[79] E. Martines, L. Csaderova, H. Morgan, A. S. G. Curtis, and M. O. Riehle, 'DLVO interaction energy between a sphere and a nano-patterned plate', *Colloids Surf. Physicochem. Eng. Asp.*, vol. 318, no. 1, pp. 45–52, 2008, doi: https://doi.org/10.1016/j.colsurfa.2007.11.035.

[80] S. Perni, E. C. Preedy, and P. Prokopovich, 'Success and failure of colloidal approaches in adhesion of microorganisms to surfaces', *Adv. Colloid Interface Sci.*, vol. 206, pp. 265–274, 2014, doi: https://doi.org/10.1016/j.cis.2013.11.008.

[81] B. V. Derjaguin, V. M. Muller, and Y. P. Toporov, 'Effect of contact deformations on the adhesion of particles', *J. Colloid Interface Sci.*, vol. 53, no. 2, pp. 314–326, 1975, doi: https://doi.org/10.1016/0021-9797(75)90018-1.

[82] R. Pelton, 'Bioactive paper provides a low-cost platform for diagnostics', *TrAC Trends Anal. Chem.*, vol. 28, no. 8, pp. 925–942, 2009, doi: https://doi.org/10.1016/j.trac.2009.05.005.

[83] S. Lindman, I. Lynch, E. Thulin, H. Nilsson, K. A. Dawson, and S. Linse, 'Systematic Investigation of the Thermodynamics of HSA Adsorption to N-iso-Propylacrylamide/N-tert-Butylacrylamide Copolymer Nanoparticles. Effects of Particle Size and Hydrophobicity', *Nano Lett.*, vol. 7, no. 4, pp. 914–920, Apr. 2007, doi: 10.1021/nl062743+.

[84] C. Wilson, R. Clegg, D. Leavesley, and M. Pearcy, 'Mediation of Biomaterial–Cell Interactions by Adsorbed Proteins: A Review', *Tissue Eng.*, vol. 11, pp. 1–18, Jan. 2005, doi: 10.1089/ten.2005.11.1.

[85] G. Singh, K. Bremmell, H. Griesser, and P. Kingshott, 'Colloid-probe AFM studies of the interaction forces of proteins adsorbed on colloidal crystals', *Soft Matter*, vol. 11, Feb. 2015, doi: 10.1039/C4SM02669A.

[86] I. Vikholm-Lundin *et al.*, 'Cysteine-tagged chimeric avidin forms high binding capacity layers directly on gold', *Sens. Actuators B Chem.*, vol. 171–172, pp. 440–448, 2012, doi: https://doi.org/10.1016/j.snb.2012.05.008.

[87] J. Korpela, E.-M. Salonen, P. Kuusela, M. Sarvas, and A. Vaheri, 'Binding of avidin to bacteria and to the outer membrane porin of Escherichia coli', *FEMS Microbiol. Lett.*, vol. 22, no. 1, pp. 3–10, Apr. 1984, doi: 10.1111/j.1574-6968.1984.tb00344.x.

[88] V. Carniello, B. W. Peterson, H. C. van der Mei, and H. J. Busscher, 'Physico-chemistry from initial bacterial adhesion to surface-programmed biofilm growth', *Adv. Colloid Interface Sci.*, vol. 261, pp. 1–14, 2018, doi: https://doi.org/10.1016/j.cis.2018.10.005.

[89] H. H. Tuson and D. B. Weibel, 'Bacteria–surface interactions', *Soft Matter*, vol. 9, no. 17, pp. 4368–4380, 2013, doi: 10.1039/C3SM27705D.

[90] Y. H. An and R. J. Friedman, 'Concise review of mechanisms of bacterial adhesion to biomaterial surfaces.', *J. Biomed. Mater. Res.*, vol. 43, no. 3, pp. 338–348, Fall 1998, doi: 10.1002/(sici)1097-4636(199823)43:3<338::aid-jbm16>3.0.co;2-b.

[91] E. J. Stewart, M. Ganesan, J. G. Younger, and M. J. Solomon, 'Artificial biofilms establish the role of matrix interactions in staphylococcal biofilm assembly and disassembly.', *Sci. Rep.*, vol. 5, p. 13081, Aug. 2015, doi: 10.1038/srep13081.

[92] R. A. Snyder, C. K. Ellison, G. B. Severin, G. B. Whitfield, C. M. Waters, and Y. V. Brun, 'Surface sensing stimulates cellular differentiation in Caulobacter crescentus', *Proc. Natl. Acad. Sci.*, vol. 117, no. 30, pp. 17984–17991, 2020, doi: 10.1073/pnas.1920291117.

[93] U. Hofer, 'Touching base on bacterial surface sensing', *Nat. Rev. Microbiol.*, vol. 16, no. 1, pp. 3–3, Jan. 2018, doi: 10.1038/nrmicro.2017.150.

[94] D. G. Allison and P. Gilbert, 'Modification by surface association of antimicrobial susceptibility of bacterial populations', *J. Ind. Microbiol.*, vol. 15, no. 4, pp. 311–317, Oct. 1995, doi: 10.1007/BF01569985.

[95] E. Preedy, S. Perni, D. Nipiĉ, K. Bohinc, and P. Prokopovich, 'Surface Roughness Mediated Adhesion Forces between Borosilicate Glass and Gram-Positive Bacteria', *Langmuir*, vol. 30, no. 31, pp. 9466–9476, Aug. 2014, doi: 10.1021/la501711t.

[96] K. Hori and S. Matsumoto, 'Bacterial adhesion: From mechanism to control', *Biochem. Eng. J.*, vol. 48, no. 3, pp. 424–434, 2010, doi: https://doi.org/10.1016/j.bej.2009.11.014.

[97] D. R. Korber, A. Choi, G. M. Wolfaardt, S. C. Ingham, and D. E. Caldwell, 'Substratum topography influences susceptibility of Salmonella enteritidis biofilms to trisodium phosphate', *Appl. Environ. Microbiol.*, vol. 63, no. 9, pp. 3352–3358, Sep. 1997, doi: 10.1128/AEM.63.9.3352-3358.1997.

[98] M. Otto, 'Staphylococcal Infections: Mechanisms of Biofilm Maturation and Detachment as Critical Determinants of Pathogenicity', *Annu. Rev. Med.*, vol. 64, no. 1, pp. 175–188, Jan. 2013, doi: 10.1146/annurev-med-042711-140023.

[99] J. W. Costerton, P. S. Stewart, and E. P. Greenberg, 'Bacterial biofilms: a common cause of persistent infections.', *Science*, vol. 284, no. 5418, pp. 1318–1322, May 1999, doi: 10.1126/science.284.5418.1318.

[100] M. H. Lin *et al.*, 'Elucidating the Crucial Role of Poly N-Acetylglucosamine from Staphylococcus aureus in Cellular Adhesion and Pathogenesis', *PLOS ONE*, vol. 10, no. 4, p. e0124216, Apr. 2015, doi: 10.1371/journal.pone.0124216.

[101] J. Yan and B. L. Bassler, 'Surviving as a Community: Antibiotic Tolerance and Persistence in Bacterial Biofilms.', *Cell Host Microbe*, vol. 26, no. 1, pp. 15–21, Jul. 2019, doi: 10.1016/j.chom.2019.06.002.

[102] T. J. Foster, J. A. Geoghegan, V. K. Ganesh, and M. Höök, 'Adhesion, invasion and evasion: the many functions of the surface proteins of Staphylococcus aureus.', *Nat. Rev. Microbiol.*, vol. 12, no. 1, pp. 49–62, Jan. 2014, doi: 10.1038/nrmicro3161.

[103] S. Ostvar and B. Wood, 'Multiscale Model Describing Bacterial Adhesion and Detachment', *Langmuir*, vol. 32, Apr. 2016, doi: 10.1021/acs.langmuir.6b00882.

[104] J. K. Oh *et al.*, 'The influence of surface chemistry on the kinetics and thermodynamics of bacterial adhesion', *Sci. Rep.*, vol. 8, no. 1, p. 17247, Nov. 2018, doi: 10.1038/s41598-018-35343-1.

[105] K. W. Kolewe, J. Zhu, N. R. Mako, S. S. Nonnenmann, and J. D. Schiffman, 'Bacterial Adhesion Is Affected by the Thickness and Stiffness of Poly(ethylene glycol) Hydrogels', *ACS Appl. Mater. Interfaces*, vol. 10, no. 3, pp. 2275–2281, Jan. 2018, doi: 10.1021/acsami.7b12145.

[106] K. W. Kolewe, S. R. Peyton, and J. D. Schiffman, 'Fewer Bacteria Adhere to Softer Hydrogels.', *ACS Appl. Mater. Interfaces*, vol. 7, no. 35, pp. 19562–19569, Sep. 2015, doi: 10.1021/acsami.5b04269.

[107] F. Song, M. E. Brasch, H. Wang, J. H. Henderson, K. Sauer, and D. Ren, 'How Bacteria Respond to Material Stiffness during Attachment: A Role of Escherichia coli Flagellar Motility.', *ACS Appl. Mater. Interfaces*, vol. 9, no. 27, pp. 22176–22184, Jul. 2017, doi: 10.1021/acsami.7b04757.

[108] K. Bazaka, M. Jacob, V. K. Truong, R. Crawford, and E. Ivanova, 'The Effect of Polyterpenol Thin Film Surfaces on Bacterial Viability and Adhesion', *Polymers*, vol. 3, Dec. 2011, doi: 10.3390/polym3010388.

[109] V. K. Truong *et al.*, 'Effect of ultrafine-grained titanium surfaces on adhesion of bacteria.', *Appl. Microbiol. Biotechnol.*, vol. 83, no. 5, pp. 925–937, Jul. 2009, doi: 10.1007/s00253-009-1944-5.

[110] V. K. Truong *et al.*, 'Bacterial Attachment Response on Titanium Surfaces with Nanometric Topographic Features', in *Progress in Colloid and Polymer Science*, vol. 137, 2010, pp. 41–45. doi: 10.1007/978-3-642-13461-6_9.

[111] M. N. Bellon-Fontaine *et al.*, 'A comparison of thermodynamic approaches to predict the adhesion of dairy microorganisms to solid substrata.', *Cell Biophys.*, vol. 17, no. 1, pp. 93–106, Aug. 1990, doi: 10.1007/BF02989805.

[112] K. A. Whitehead, J. Colligon, and J. Verran, 'Retention of microbial cells in substratum surface features of micrometer and sub-micrometer dimensions.', *Colloids Surf. B Biointerfaces*, vol. 41, no. 2–3, pp. 129–138, Mar. 2005, doi: 10.1016/j.colsurfb.2004.11.010.

[113] M. Quirynen and C. M. L. Bollen, 'The influence of surface roughness and surface-free energy on supra- and subgingival plaque formation in man', *J. Clin. Periodontol.*, vol. 22, no. 1, pp. 1–14, Jan. 1995, doi: 10.1111/j.1600-051X.1995.tb01765.x.
[114] M.-N. Bellon-Fontaine, J. Rault, and C. J. van Oss, 'Microbial adhesion to solvents: a novel method to determine the electron-donor/electron-acceptor or Lewis acid-base properties of microbial cells', *Colloids Surf. B Biointerfaces*, vol. 7, no. 1, pp. 47–53, Jul. 1996, doi: 10.1016/0927-7765(96)01272-6.
[115] F. Alam and K. Balani, 'Adhesion force of staphylococcus aureus on various biomaterial surfaces.', *J. Mech. Behav. Biomed. Mater.*, vol. 65, pp. 872–880, Jan. 2017, doi: 10.1016/j.jmbbm.2016.10.009.
[116] K. Shahramian *et al.*, 'Sol–gel derived bioactive coating on zirconia: Effect on flexural strength and cell proliferation', *J. Biomed. Mater. Res. B Appl. Biomater.*, vol. 105, no. 8, pp. 2401–2407, 2017, doi: https://doi.org/10.1002/jbm.b.33780.
[117] K. Shahramian *et al.*, 'Zirconia implants with improved attachment to the gingival tissue', *J. Periodontol.*, vol. 91, no. 9, pp. 1213–1224, 2020, doi: https://doi.org/10.1002/JPER.19-0323.
[118] J. Li *et al.*, 'The observed difference of macrophage phenotype on different surface roughness of mineralized collagen', *Regen. Biomater.*, vol. 7, no. 2, pp. 203–211, Mar. 2020, doi: 10.1093/rb/rbz053.
[119] K. M. Hotchkiss, G. B. Reddy, S. L. Hyzy, Z. Schwartz, B. D. Boyan, and R. Olivares-Navarrete, 'Titanium surface characteristics, including topography and wettability, alter macrophage activation', *Acta Biomater.*, vol. 31, pp. 425–434, Feb. 2016, doi: 10.1016/j.actbio.2015.12.003.
[120] X. Dai *et al.*, 'Attenuating Immune Response of Macrophage by Enhancing Hydrophilicity of Ti Surface', *J. Nanomater.*, vol. 2015, p. 712810, May 2015, doi: 10.1155/2015/712810.
[121] B. M. Gumbiner, 'Cell adhesion: the molecular basis of tissue architecture and morphogenesis.', *Cell*, vol. 84, no. 3, pp. 345–357, Feb. 1996, doi: 10.1016/s0092-8674(00)81279-9.
[122] L. Bacáková, E. Filová, F. Rypácek, V. Svorcík, and V. Starý, 'Cell adhesion on artificial materials for tissue engineering.', *Physiol. Res.*, vol. 53 Suppl 1, pp. S35-45, 2004.
[123] J. R. Gershlak *et al.*, 'Crossing kingdoms: Using decellularized plants as perfusable tissue engineering scaffolds', *Biomaterials*, vol. 125, pp. 13–22, 2017, doi: https://doi.org/10.1016/j.biomaterials.2017.02.011.
[124] W. O. Fenn, 'THE THEORETICAL RESPONSE OF LIVING CELLS TO CONTACT WITH SOLID BODIES', *J. Gen. Physiol.*, vol. 4, no. 4, pp. 373–385, Mar. 1922, doi: 10.1085/jgp.4.4.373.
[125] J. Solon, I. Levental, K. Sengupta, P. C. Georges, and P. A. Janmey, 'Fibroblast adaptation and stiffness matching to soft elastic substrates.', *Biophys. J.*, vol. 93, no. 12, pp. 4453–4461, Dec. 2007, doi: 10.1529/biophysj.106.101386.
[126] G. Abagnale *et al.*, 'Surface topography enhances differentiation of mesenchymal stem cells towards osteogenic and adipogenic lineages', *Biomaterials*, vol. 61, pp. 316–326, 2015, doi: https://doi.org/10.1016/j.biomaterials.2015.05.030.
[127] V. F. Achterberg *et al.*, 'The nano-scale mechanical properties of the extracellular matrix regulate dermal fibroblast function.', *J. Invest. Dermatol.*, vol. 134, no. 7, pp. 1862–1872, Jul. 2014, doi: 10.1038/jid.2014.90.
[128] D. E. Discher, P. Janmey, and Y.-L. Wang, 'Tissue cells feel and respond to the stiffness of their substrate.', *Science*, vol. 310, no. 5751, pp. 1139–1143, Nov. 2005, doi: 10.1126/science.1116995.
[129] Y.-S. Lai, W.-C. Chen, C.-H. Huang, C.-K. Cheng, K.-K. Chan, and T.-K. Chang, 'The Effect of Graft Strength on Knee Laxity and Graft In-Situ Forces after Posterior Cruciate Ligament Reconstruction', *PLOS ONE*, vol. 10, p. e0127293, 2015, doi: 10.1371/journal.pone.0127293.
[130] X. Le, G. E. J. Poinern, N. Ali, C. M. Berry, and D. Fawcett, 'Engineering a Biocompatible Scaffold with Either Micrometre or Nanometre Scale Surface Topography for Promoting Protein Adsorption and Cellular Response', *Int. J. Biomater.*, vol. 2013, p. 782549, Feb. 2013, doi: 10.1155/2013/782549.

[131] G. Altankov, K. Richau, and Th. Groth, 'The role of surface zeta potential and substratum chemistry for regulation of dermal fibroblasts interaction', *Mater. Werkst.*, vol. 34, no. 12, pp. 1120–1128, 2003, doi: https://doi.org/10.1002/mawe.200300699.
[132] R. Green and M. R. Abidian, 'Conducting Polymers for Neural Prosthetic and Neural Interface Applications', *Adv. Mater. Deerfield Beach Fla*, vol. 27, no. 46, pp. 7620–7637, Dec. 2015, doi: 10.1002/adma.201501810.
[133] C. Sung, W. Jeon, K. S. Nam, Y. Kim, H. Butt, and S. Park, 'Multimaterial and multifunctional neural interfaces: from surface-type and implantable electrodes to fiber-based devices', *J. Mater. Chem. B*, vol. 8, no. 31, pp. 6624–6666, 2020, doi: 10.1039/D0TB00872A.
[134] N. Li *et al.*, 'Three-dimensional graphene foam as a biocompatible and conductive scaffold for neural stem cells', *Sci. Rep.*, vol. 3, no. 1, p. 1604, Apr. 2013, doi: 10.1038/srep01604.
[135] M. Farokhi *et al.*, 'Conductive Biomaterials as Substrates for Neural Stem Cells Differentiation towards Neuronal Lineage Cells', *Macromol. Biosci.*, vol. 21, no. 1, p. 2000123, Jan. 2021, doi: 10.1002/mabi.202000123.
[136] M. Rouabhia, H. Park, S. Meng, H. Derbali, and Z. Zhang, 'Electrical Stimulation Promotes Wound Healing by Enhancing Dermal Fibroblast Activity and Promoting Myofibroblast Transdifferentiation', *PLOS ONE*, vol. 8, no. 8, p. e71660, Aug. 2013, doi: 10.1371/journal.pone.0071660.
[137] W. Hu *et al.*, 'Enhancing proliferation and migration of fibroblast cells by electric stimulation based on triboelectric nanogenerator', *Nano Energy*, vol. 57, pp. 600–607, Mar. 2019, doi: 10.1016/j.nanoen.2018.12.077.
[138] S. Li *et al.*, 'Electrical Stimulation Activates Fibroblasts through the Elevation of Intracellular Free Ca2+: Potential Mechanism of Pelvic Electrical Stimulation Therapy', *BioMed Res. Int.*, vol. 2019, p. 7387803, Apr. 2019, doi: 10.1155/2019/7387803.
[139] E. Kim, J.-Y. Kim, and H. Choi, 'An SU-8-based microprobe with a nanostructured surface enhances neuronal cell attachment and growth', *Micro Nano Syst. Lett.*, vol. 5, no. 1, p. 28, Dec. 2017, doi: 10.1186/s40486-017-0062-x.
[140] Y. Zhang, S. Wang, and P. Yang, 'Effects of Graphene-Based Materials on the Behavior of Neural Stem Cells', *J. Nanomater.*, vol. 2020, p. 2519105, Jul. 2020, doi: 10.1155/2020/2519105.
[141] Z. Li *et al.*, 'Influence of surface roughness on neural differentiation of human induced pluripotent stem cells.', *Clin. Hemorheol. Microcirc.*, vol. 64, no. 3, pp. 355–366, 2016, doi: 10.3233/CH-168121.
[142] E. A. Dubiel, Y. Martin, and P. Vermette, 'Bridging the Gap Between Physicochemistry and Interpretation Prevalent in Cell–Surface Interactions', *Chem. Rev.*, vol. 111, no. 4, pp. 2900–2936, Apr. 2011, doi: 10.1021/cr9002598.
[143] E. A. Vogler, 'Thermodynamics of short-term cell adhesion in vitro', *Biophys. J.*, vol. 53, no. 5, pp. 759–769, May 1988, doi: 10.1016/S0006-3495(88)83156-4.
[144] M. Tavakolian *et al.*, 'Highly Absorbent Antibacterial and Biofilm-Disrupting Hydrogels from Cellulose for Wound Dressing Applications', *ACS Appl. Mater. Interfaces*, vol. 12, no. 36, pp. 39991–40001, Sep. 2020, doi: 10.1021/acsami.0c08784.
[145] D. Șen Karaman *et al.*, 'Mesoporous silica nanoparticles facilitating the dissolution of poorly soluble drugs in orodispersible films', *Eur. J. Pharm. Sci.*, vol. 122, pp. 152–159, 2018, doi: https://doi.org/10.1016/j.ejps.2018.06.027.
[146] M. P. Rode *et al.*, 'Carrageenan hydrogel as a scaffold for skin-derived multipotent stromal cells delivery', *J. Biomater. Appl.*, vol. 33, no. 3, pp. 422–434, 2018, doi: 10.1177/0885328218795569.
[147] E. A. Vogler, 'Structure and reactivity of water at biomaterial surfaces', *Adv. Colloid Interface Sci.*, vol. 74, no. 1, pp. 69–117, 1998, doi: https://doi.org/10.1016/S0001-8686(97)00040-7.
[148] D. Costa, P.-A. Garrain, and M. Baaden, 'Understanding small biomolecule-biomaterial interactions: A review of fundamental theoretical and experimental approaches for biomolecule interactions with inorganic surfaces', *J. Biomed. Mater. Res. A*, vol. 101A, no. 4, pp. 1210–1222, 2013, doi: https://doi.org/10.1002/jbm.a.34416.

[149] C. Gao, S. Peng, P. Feng, and C. Shuai, 'Bone biomaterials and interactions with stem cells', *Bone Res.*, vol. 5, no. 1, p. 17059, Dec. 2017, doi: 10.1038/boneres.2017.59.
[150] K. Shahramian, A. Abdulmajeed, I. Kangasniemi, E. Söderling, and T. Närhi, 'TiO2 Coating and UV Photofunctionalization Enhance Blood Coagulation on Zirconia Surfaces', *BioMed Res. Int.*, vol. 2019, p. 8078230, Apr. 2019, doi: 10.1155/2019/8078230.
[151] J. R. Jones, D. S. Brauer, L. Hupa, and D. C. Greenspan, 'Bioglass and Bioactive Glasses and Their Impact on Healthcare', *Int. J. Appl. Glass Sci.*, vol. 7, no. 4, pp. 423–434, 2016, doi: https://doi.org/10.1111/ijag.12252.
[152] K. Prasad *et al.*, 'Metallic Biomaterials: Current Challenges and Opportunities', *Mater. Basel Switz.*, vol. 10, no. 8, p. 884, Jul. 2017, doi: 10.3390/ma10080884.
[153] A. Wadood, 'Brief Overview on Nitinol as Biomaterial', *Adv. Mater. Sci. Eng.*, vol. 2016, p. 4173138, Nov. 2016, doi: 10.1155/2016/4173138.
[154] L. Petrini and F. Migliavacca, 'Biomedical Applications of Shape Memory Alloys', *J. Metall.*, vol. 2011, Apr. 2011, doi: 10.1155/2011/501483.
[155] L. Yahia, '1 - Introduction to shape-memory polymers for biomedical applications', in *Shape Memory Polymers for Biomedical Applications*, L. Yahia, Ed. Woodhead Publishing, 2015, pp. 3–8. doi: 10.1016/B978-0-85709-698-2.00001-5.
[156] N. S. Moghaddam, R. Skoracki, M. Miller, M. Elahinia, and D. Dean, 'Three Dimensional Printing of Stiffness-tuned, Nitinol Skeletal Fixation Hardware with an Example of Mandibular Segmental Defect Repair', *Second CIRP Conf. Biomanufacturing*, vol. 49, pp. 45–50, Jan. 2016, doi: 10.1016/j.procir.2015.07.027.
[157] N. Angelova and D. Hunkeler, 'Rationalizing the design of polymeric biomaterials', *Trends Biotechnol.*, vol. 17, no. 10, pp. 409–421, 1999, doi: https://doi.org/10.1016/S0167-7799(99)01356-6.
[158] A. Metcalfe, A.-C. Desfaits, I. Salazkin, L. Yahia, W. M. Sokolowski, and J. Raymond, 'Cold hibernated elastic memory foams for endovascular interventions', *Biomaterials*, vol. 24, no. 3, pp. 491–497, Feb. 2003, doi: 10.1016/S0142-9612(02)00362-9.
[159] J. Xu and J. Song, '10 - Polylactic acid (PLA)-based shape-memory materials for biomedical applications', in *Shape Memory Polymers for Biomedical Applications*, L. Yahia, Ed. Woodhead Publishing, 2015, pp. 197–217. doi: 10.1016/B978-0-85709-698-2.00010-6.
[160] N. Yi and M. R. Abidian, '10 - Conducting polymers and their biomedical applications', in *Biosynthetic Polymers for Medical Applications*, L. Poole-Warren, P. Martens, and R. Green, Eds. Woodhead Publishing, 2016, pp. 243–276. doi: 10.1016/B978-1-78242-105-4.00010-9.
[161] T. Nezakati, A. Seifalian, A. Tan, and A. M. Seifalian, 'Conductive Polymers: Opportunities and Challenges in Biomedical Applications', *Chem. Rev.*, vol. 118, no. 14, pp. 6766–6843, Jul. 2018, doi: 10.1021/acs.chemrev.6b00275.
[162] S. D. Dutta, D. K. Patel, and K.-T. Lim, 'Functional cellulose-based hydrogels as extracellular matrices for tissue engineering', *J. Biol. Eng.*, vol. 13, no. 1, p. 55, Jun. 2019, doi: 10.1186/s13036-019-0177-0.
[163] R. Kummala *et al.*, 'Human Dermal Fibroblast Viability and Adhesion on Cellulose Nanomaterial Coatings: Influence of Surface Characteristics', *Biomacromolecules*, vol. 21, no. 4, pp. 1560–1567, Apr. 2020, doi: 10.1021/acs.biomac.0c00107.
[164] E. G. Popa *et al.*, 'Evaluation of the in vitro and in vivo biocompatibility of carrageenan-based hydrogels.', *J. Biomed. Mater. Res. A*, vol. 102, no. 11, pp. 4087–4097, Nov. 2014, doi: 10.1002/jbm.a.35081.
[165] K. Ng *et al.*, 'Paper-based cell culture platform and its emerging biomedical applications', *Mater. Today*, vol. 20, no. 1, pp. 32–44, 2017, doi: https://doi.org/10.1016/j.mattod.2016.07.001.
[166] K. Markstedt, A. Mantas, I. Tournier, H. Martínez Ávila, D. Hägg, and P. Gatenholm, '3D Bioprinting Human Chondrocytes with Nanocellulose–Alginate Bioink for Cartilage Tissue Engineering Applications', *Biomacromolecules*, vol. 16, no. 5, pp. 1489–1496, May 2015, doi: 10.1021/acs.biomac.5b00188.

[167] X. Wang, Q. Wang, and C. Xu, 'Nanocellulose-Based Inks for 3D Bioprinting: Key Aspects in Research Development and Challenging Perspectives in Applications—A Mini Review', *Bioengineering*, vol. 7, no. 2, 2020, doi: 10.3390/bioengineering7020040.
[168] M. Kapałczyńska *et al.*, '2D and 3D cell cultures - a comparison of different types of cancer cell cultures', *Arch. Med. Sci. AMS*, vol. 14, no. 4, pp. 910–919, Jun. 2018, doi: 10.5114/aoms.2016.63743.
[169] J. Hoarau-Véchot, A. Rafii, C. Touboul, and J. Pasquier, 'Halfway between 2D and Animal Models: Are 3D Cultures the Ideal Tool to Study Cancer-Microenvironment Interactions?', *Int. J. Mol. Sci.*, vol. 19, no. 1, Jan. 2018, doi: 10.3390/ijms19010181.
[170] C. Xu *et al.*, '3D printing of nanocellulose hydrogel scaffolds with tunable mechanical strength towards wound healing application', *J. Mater. Chem. B*, vol. 6, no. 43, pp. 7066–7075, 2018, doi: 10.1039/C8TB01757C.
[171] H. Golmohammadi, E. Morales-Narváez, T. Naghdi, and A. Merkoçi, 'Nanocellulose in Sensing and Biosensing', *Chem. Mater.*, vol. 29, no. 13, pp. 5426–5446, Jul. 2017, doi: 10.1021/acs.chemmater.7b01170.
[172] J.-Y. Kim, Y. J. Yun, J. Jeong, C.-Y. Kim, K.-R. Müller, and S.-W. Lee, 'Leaf-inspired homeostatic cellulose biosensors', *Sci. Adv.*, vol. 7, no. 16, p. eabe7432, Apr. 2021, doi: 10.1126/sciadv.abe7432.
[173] A. Määttänen, D. Fors, S. Wang, D. Valtakari, P. Ihalainen, and J. Peltonen, 'Paper-based planar reaction arrays for printed diagnostics', *Sens. Actuators B Chem.*, vol. 160, no. 1, pp. 1404–1412, 2011, doi: https://doi.org/10.1016/j.snb.2011.09.086.
[174] A. Määttänen, A. Fallarero, J. Kujala, P. Ihalainen, P. Vuorela, and J. Peltonen, 'Printed paper-based arrays as substrates for biofilm formation', *AMB Express*, vol. 4, no. 1, p. 32, Jun. 2014, doi: 10.1186/s13568-014-0032-0.
[175] H. Juvonen *et al.*, 'Biocompatibility of printed paper-based arrays for 2-D cell cultures', *Acta Biomater.*, vol. 9, no. 5, pp. 6704–6710, 2013, doi: https://doi.org/10.1016/j.actbio.2013.01.033.
[176] D. Lantigua, Y. N. Kelly, B. Unal, and G. Camci-Unal, 'Engineered Paper-Based Cell Culture Platforms.', *Adv. Healthc. Mater.*, vol. 6, no. 22, Nov. 2017, doi: 10.1002/adhm.201700619.
[177] J. Ma *et al.*, 'Paper Microfluidics for Cell Analysis', *Adv. Healthc. Mater.*, vol. 8, no. 1, p. 1801084, 2019, doi: https://doi.org/10.1002/adhm.201801084.
[178] D. Soto Veliz, H. Zhang, and M. Toivakka, 'Stacking up: a new approach for cell culture studies', *Biomater Sci*, vol. 7, no. 8, pp. 3249–3257, 2019, doi: 10.1039/C8BM01694A.
[179] A. W. Martinez, S. T. Phillips, G. M. Whitesides, and E. Carrilho, 'Diagnostics for the developing world: microfluidic paper-based analytical devices.', *Anal. Chem.*, vol. 82, no. 1, pp. 3–10, Jan. 2010, doi: 10.1021/ac9013989.
[180] T. Agarwal, M. R. Borrelli, P. Makvandi, M. Ashrafizadeh, and T. K. Maiti, 'Paper-Based Cell Culture: Paving the Pathway for Liver Tissue Model Development on a Cellulose Paper Chip', *ACS Appl. Bio Mater.*, vol. 3, no. 7, pp. 3956–3974, Jul. 2020, doi: 10.1021/acsabm.0c00558.
[181] L. Zhang, Q. Zhou, W. Song, K. Wu, Y. Zhang, and Y. Zhao, 'Dual-Functionalized Graphene Oxide Based siRNA Delivery System for Implant Surface Biomodification with Enhanced Osteogenesis', *ACS Appl. Mater. Interfaces*, vol. 9, no. 40, pp. 34722–34735, Oct. 2017, doi: 10.1021/acsami.7b12079.
[182] M. Nishi *et al.*, 'The use of biotin–avidin binding to facilitate biomodification of thermoresponsive culture surfaces', *Biomaterials*, vol. 28, no. 36, pp. 5471–5476, Dec. 2007, doi: 10.1016/j.biomaterials.2007.08.027.
[183] X. Wang, Z. Qu, J. Li, and E. Zhang, 'Comparison study on the solution-based surface biomodification of titanium: Surface characteristics and cell biocompatibility', *Surf. Coat. Technol.*, vol. 329, pp. 109–119, Nov. 2017, doi: 10.1016/j.surfcoat.2017.08.014.
[184] E. Zhang and C. Zou, 'Porous titanium and silicon-substituted hydroxyapatite biomodification prepared by a biomimetic process: Characterization and in vivo evaluation', *Acta Biomater.*, vol. 5, no. 5, pp. 1732–1741, Jun. 2009, doi: 10.1016/j.actbio.2009.01.014.

[185] K. J. Brobbey *et al.*, 'Effect of plasma coating on antibacterial activity of silver nanoparticles', *Thin Solid Films*, vol. 672, pp. 75–82, 2019, doi: https://doi.org/10.1016/j.tsf.2018.12.049.
[186] K. J. Brobbey *et al.*, 'Characterization of flame coated nanoparticle surfaces with antibacterial properties and the heat-induced embedding in thermoplastic-coated paper', *SN Appl. Sci.*, vol. 1, no. 1, p. 65, Nov. 2018, doi: 10.1007/s42452-018-0053-4.
[187] K. Khanmohammadi Chenab, B. Sohrabi, and A. Rahmanzadeh, 'Superhydrophobicity: advanced biological and biomedical applications', *Biomater Sci*, vol. 7, no. 8, pp. 3110–3137, 2019, doi: 10.1039/C9BM00558G.
[188] S. Tojkander, G. Gateva, and P. Lappalainen, 'Actin stress fibers – assembly, dynamics and biological roles', *J. Cell Sci.*, vol. 125, no. 8, p. 1855, Apr. 2012, doi: 10.1242/jcs.098087.
[189] J. Lee, M. J. Cuddihy, and N. A. Kotov, 'Three-Dimensional Cell Culture Matrices: State of the Art', *Tissue Eng. Part B Rev.*, vol. 14, no. 1, pp. 61–86, 2008, doi: 10.1089/teb.2007.0150.
[190] M. A. Pesonen, J. V. Frisk, and R. M. Österbacka, 'Voltage dependent reduction rates of graphene oxide in cell culture medium, deionized water, and an ionic liquid', *Org. Electron.*, vol. 47, pp. 66–71, 2017, doi: https://doi.org/10.1016/j.orgel.2017.04.029.
[191] A. Määttänen, P. Ihalainen, B. Törngren, E. Rosqvist, M. Pesonen, and J. Peltonen, 'Hierarchically structured self-supported latex films for flexible and semi-transparent electronics', *Appl. Surf. Sci.*, vol. 364, pp. 37–44, 2016, doi: https://doi.org/10.1016/j.apsusc.2015.12.088.
[192] A. Ferrario, M. Scaramuzza, E. Pasqualotto, A. Toni, M. Maschietto, and S. Vassanelli, 'Electrochemical impedance spectroscopy study of the cells adhesion over microelectrodes array', *2011 7th Conf. PhD Res. Microelectron. Electron. PRIME 2011 - Conf. Proc.*, 2011, doi: 10.1109/PRIME.2011.5966216.
[193] J. Kieninger, A. Weltin, H. Flamm, and G. A. Urban, 'Microsensor systems for cell metabolism – from 2D culture to organ-on-chip', *Lab Chip*, vol. 18, no. 9, pp. 1274–1291, 2018, doi: 10.1039/C7LC00942A.
[194] J. Sarfraz *et al.*, 'Photo-thermal and cytotoxic properties of inkjet-printed copper sulfide films on biocompatible latex coated substrates', *Appl. Surf. Sci.*, vol. 435, pp. 1087–1095, 2018, doi: https://doi.org/10.1016/j.apsusc.2017.11.203.
[195] P. Ihalainen *et al.*, 'Paper-supported nanostructured ultrathin gold film electrodes – Characterization and functionalization', *Appl. Surf. Sci.*, vol. 329, pp. 321–329, 2015, doi: https://doi.org/10.1016/j.apsusc.2014.12.156.
[196] J. M. Charest, J. P. Califano, S. P. Carey, and C. A. Reinhart-King, 'Fabrication of substrates with defined mechanical properties and topographical features for the study of cell migration.', *Macromol. Biosci.*, vol. 12, no. 1, pp. 12–20, Jan. 2012, doi: 10.1002/mabi.201100264.
[197] D. Falconnet, G. Csucs, H. M. Grandin, and M. Textor, 'Surface engineering approaches to micropattern surfaces for cell-based assays', *Biomaterials*, vol. 27, no. 16, pp. 3044–3063, 2006, doi: https://doi.org/10.1016/j.biomaterials.2005.12.024.
[198] B. Carlin, S. Yang, J.-X. Li, and L. Felton, '2 Pseudolatex Dispersions for Controlled Drug Delivery', 2016, pp. 11–48. doi: 10.1201/9781315369938-3.
[199] P. A. Steward, J. Hearn, and M. C. Wilkinson, 'An overview of polymer latex film formation and properties', *Adv. Colloid Interface Sci.*, vol. 86, no. 3, pp. 195–267, 2000, doi: https://doi.org/10.1016/S0001-8686(99)00037-8.
[200] J. G. Spiro, J. P. S. Farinha, and M. A. Winnik, 'Thermodynamics and Morphology of Latex Blend Films', *Macromolecules*, vol. 36, no. 20, pp. 7791–7802, Oct. 2003, doi: 10.1021/ma021579j.
[201] H. Juvonen, A. Määttänen, P. Ihalainen, T. Viitala, J. Sarfraz, and J. Peltonen, 'Enhanced protein adsorption and patterning on nanostructured latex-coated paper', *Colloids Surf. B Biointerfaces*, vol. 118, pp. 261–269, 2014, doi: https://doi.org/10.1016/j.colsurfb.2014.03.050.
[202] W. P. Lee, V. R. Gundabala, B. S. Akpa, M. L. Johns, C. Jeynes, and A. F. Routh, 'Distribution of Surfactants in Latex Films: A Rutherford Backscattering Study', *Langmuir*, vol. 22, no. 12, pp. 5314–5320, Jun. 2006, doi: 10.1021/la0601760.

[203] B. Voogt *et al.*, 'Film Formation of High Tg Latex Using Hydroplasticization: Explanations from NMR Relaxometry', *Langmuir*, vol. 35, no. 38, pp. 12418–12427, Sep. 2019, doi: 10.1021/acs.langmuir.9b01353.
[204] J. Shin, D. Lee, and P. D. Fleming, 'The Characterization of Biobased Latex Dispersions by Serum Replacement', *Appita J.*, vol. 70, p. 251~259, Sep. 2017.
[205] M. Winnik and J. Feng, 'Latex blends : an approach to zero VOC coatings', *J. Coat. Technol.*, vol. 68, pp. 39–50, 1996.
[206] A. Tzitzinou, J. L. Keddie, J. M. Geurts, A. C. I. A. Peters, and R. Satguru, 'Film Formation of Latex Blends with Bimodal Particle Size Distributions: Consideration of Particle Deformability and Continuity of the Dispersed Phase', *Macromolecules*, vol. 33, no. 7, pp. 2695–2708, Apr. 2000, doi: 10.1021/ma991372z.
[207] C. J. van Oss, 'Use of the combined Lifshitz–van der Waals and Lewis acid–base approaches in determining the apolar and polar contributions to surface and interfacial tensions and free energies', *J. Adhes. Sci. Technol.*, vol. 16, no. 6, pp. 669–677, 2002, doi: 10.1163/156856102760099870.
[208] A. K. Hiltunen, P. M. Vuorela, and A. Fallarero, 'Bisphosphonates offer protection against prosthetic joint infections caused by Staphylococcus aureus and Staphylococcus epidermidis biofilms', *J. Drug Deliv. Sci. Technol.*, vol. 40, pp. 136–141, 2017, doi: https://doi.org/10.1016/j.jddst.2017.06.002.
[209] M. E. Skogman, P. M. Vuorela, and A. Fallarero, 'Combining biofilm matrix measurements with biomass and viability assays in susceptibility assessments of antimicrobials against Staphylococcus aureus biofilms', *J. Antibiot. (Tokyo)*, vol. 65, no. 9, pp. 453–459, Sep. 2012, doi: 10.1038/ja.2012.49.
[210] A. K. Hiltunen *et al.*, 'Structural and Functional Dynamics of Staphylococcus aureus Biofilms and Biofilm Matrix Proteins on Different Clinical Materials.', *Microorganisms*, vol. 7, no. 12, Nov. 2019, doi: 10.3390/microorganisms7120584.
[211] K. Savijoki *et al.*, 'Growth Mode and Physiological State of Cells Prior to Biofilm Formation Affect Immune Evasion and Persistence of Staphylococcus aureus.', *Microorganisms*, vol. 8, no. 1, Jan. 2020, doi: 10.3390/microorganisms8010106.
[212] M. B. Lorey, K. Rossi, K. K. Eklund, T. A. Nyman, and S. Matikainen, 'Global Characterization of Protein Secretion from Human Macrophages Following Non-canonical Caspase-4/5 Inflammasome Activation.', *Mol. Cell. Proteomics MCP*, vol. 16, no. 4 suppl 1, pp. S187–S199, Apr. 2017, doi: 10.1074/mcp.M116.064840.
[213] J. Cox and M. Mann, 'MaxQuant enables high peptide identification rates, individualized p.p.b.-range mass accuracies and proteome-wide protein quantification', *Nat. Biotechnol.*, vol. 26, no. 12, pp. 1367–1372, Dec. 2008, doi: 10.1038/nbt.1511.
[214] J. Cox, M. Y. Hein, C. A. Luber, I. Paron, N. Nagaraj, and M. Mann, 'Accurate Proteome-wide Label-free Quantification by Delayed Normalization and Maximal Peptide Ratio Extraction, Termed MaxLFQ', *Mol. Cell. Proteomics*, vol. 13, no. 9, pp. 2513–2526, 2014, doi: 10.1074/mcp.M113.031591.
[215] B. Pitts, A. Willse, G. A. McFeters, M. A. Hamilton, N. Zelver, and P. S. Stewart, 'A repeatable laboratory method for testing the efficacy of biocides against toilet bowl biofilms', *J. Appl. Microbiol.*, vol. 91, no. 1, pp. 110–117, 2001, doi: https://doi.org/10.1046/j.1365-2672.2001.01342.x.
[216] D. Szklarczyk *et al.*, 'STRING v11: protein-protein association networks with increased coverage, supporting functional discovery in genome-wide experimental datasets.', *Nucleic Acids Res.*, vol. 47, no. D1, pp. D607–D613, Jan. 2019, doi: 10.1093/nar/gky1131.
[217] W. P. Lee and A. F. Routh, 'Why Do Drying Films Crack?', *Langmuir*, vol. 20, no. 23, pp. 9885–9888, Nov. 2004, doi: 10.1021/la049020v.
[218] M. Tirumkudulu and W. Russel, 'Cracking in Drying Latex Films', *Langmuir ACS J. Surf. Colloids*, vol. 21, pp. 4938–48, Jun. 2005, doi: 10.1021/la048298k.
[219] E. Dufresne *et al.*, 'Dynamics of Fracture in Drying Suspensions', *Langmuir ACS J. Surf. Colloids*, vol. 22, pp. 7144–7, Sep. 2006, doi: 10.1021/la061251+.
[220] J. M. Soria *et al.*, 'Influence of the substrate's hydrophilicity on the in vitro Schwann cells viability', *J. Biomed. Mater. Res. A*, vol. 83A, no. 2, pp. 463–470, Nov. 2007, doi: 10.1002/jbm.a.31297.

[221] L.-C. Xu and C. A. Siedlecki, 'Effects of surface wettability and contact time on protein adhesion to biomaterial surfaces', *Biomaterials*, vol. 28, no. 22, pp. 3273–3283, Aug. 2007, doi: 10.1016/j.biomaterials.2007.03.032.
[222] R. Müller, G. Gröger, K.-A. Hiller, G. Schmalz, and S. Ruhl, 'Fluorescence-based bacterial overlay method for simultaneous in situ quantification of surface-attached bacteria.', *Appl. Environ. Microbiol.*, vol. 73, no. 8, pp. 2653–2660, Apr. 2007, doi: 10.1128/AEM.02884-06.
[223] I. Yoda *et al.*, 'Effect of surface roughness of biomaterials on Staphylococcus epidermidis adhesion', *BMC Microbiol.*, vol. 14, no. 1, p. 234, Sep. 2014, doi: 10.1186/s12866-014-0234-2.
[224] J. P. O'Gara, 'ica and beyond: biofilm mechanisms and regulation in Staphylococcus epidermidis and Staphylococcus aureus', *FEMS Microbiol. Lett.*, vol. 270, no. 2, pp. 179–188, May 2007, doi: 10.1111/j.1574-6968.2007.00688.x.
[225] W. W. Navarre and O. Schneewind, 'Surface proteins of gram-positive bacteria and mechanisms of their targeting to the cell wall envelope.', *Microbiol. Mol. Biol. Rev. MMBR*, vol. 63, no. 1, pp. 174–229, Mar. 1999.
[226] W. Wang and C. J. Jeffery, 'An analysis of surface proteomics results reveals novel candidates for intracellular/surface moonlighting proteins in bacteria.', *Mol. Biosyst.*, vol. 12, no. 5, pp. 1420–1431, Apr. 2016, doi: 10.1039/c5mb00550g.
[227] L. Foulston, A. K. W. Elsholz, A. S. DeFrancesco, and R. Losick, 'The extracellular matrix of Staphylococcus aureus biofilms comprises cytoplasmic proteins that associate with the cell surface in response to decreasing pH.', *mBio*, vol. 5, no. 5, pp. e01667-01614, Sep. 2014, doi: 10.1128/mBio.01667-14.
[228] C. J. Jeffery, 'What is Protein Moonlighting and Why is it Important?', in *Moonlighting Proteins*, John Wiley & Sons, Ltd, 2017, pp. 1–19. doi: 10.1002/9781118951149.ch1.
[229] B. Henderson and A. Martin, 'Bacterial virulence in the moonlight: multitasking bacterial moonlighting proteins are virulence determinants in infectious disease.', *Infect. Immun.*, vol. 79, no. 9, pp. 3476–3491, Sep. 2011, doi: 10.1128/IAI.00179-11.
[230] C. Jeffery, 'Intracellular proteins moonlighting as bacterial adhesion factors.', *AIMS Microbiol.*, vol. 4, no. 2, pp. 362–376, 2018, doi: 10.3934/microbiol.2018.2.362.
[231] A. C. Graf *et al.*, 'Virulence Factors Produced by Staphylococcus aureus Biofilms Have a Moonlighting Function Contributing to Biofilm Integrity.', *Mol. Cell. Proteomics MCP*, vol. 18, no. 6, pp. 1036–1053, Jun. 2019, doi: 10.1074/mcp.RA118.001120.
[232] E.-Y. Lee *et al.*, 'Gram-positive bacteria produce membrane vesicles: proteomics-based characterization of Staphylococcus aureus-derived membrane vesicles.', *Proteomics*, vol. 9, no. 24, pp. 5425–5436, Dec. 2009, doi: 10.1002/pmic.200900338.
[233] M. Yáñez-Mó *et al.*, 'Biological properties of extracellular vesicles and their physiological functions', *J. Extracell. Vesicles*, vol. 4, no. 1, p. 27066, 2015, doi: 10.3402/jev.v4.27066.
[234] G. Abagnale *et al.*, 'Surface Topography Guides Morphology and Spatial Patterning of Induced Pluripotent Stem Cell Colonies', *Stem Cell Rep.*, vol. 9, no. 2, pp. 654–666, Aug. 2017, doi: 10.1016/j.stemcr.2017.06.016.
[235] F. Gentile *et al.*, 'Cells preferentially grow on rough substrates', *Biomaterials*, vol. 31, no. 28, pp. 7205–7212, 2010, doi: https://doi.org/10.1016/j.biomaterials.2010.06.016.
[236] M. C. Morán, G. Ruano, F. Cirisano, and M. Ferrari, 'Mammalian cell viability on hydrophobic and superhydrophobic fabrics', *Mater. Sci. Eng. C*, vol. 99, pp. 241–247, 2019, doi: https://doi.org/10.1016/j.msec.2019.01.088.
[237] J. P. Best, S. Javed, J. J. Richardson, K. L. Cho, M. M. J. Kamphuis, and F. Caruso, 'Stiffness-mediated adhesion of cervical cancer cells to soft hydrogel films', *Soft Matter*, vol. 9, no. 18, pp. 4580–4584, 2013, doi: 10.1039/C3SM50587A.
[238] E. Rosqvist *et al.*, 'Human dermal fibroblast proliferation controlled by surface roughness of two-component nanostructured latex polymer coatings', *Colloids Surf. B Biointerfaces*, vol. 174, pp. 136–144, 2019, doi: https://doi.org/10.1016/j.colsurfb.2018.10.064.
[239] H. Juvonen *et al.*, 'Protein and bacterial interactions with nanostructured polymer coatings', *Colloids Surf. B Biointerfaces*, vol. 136, pp. 527–535, 2015, doi: https://doi.org/10.1016/j.colsurfb.2015.09.061.

[240] P. San Martin Galindo, E. Rosqvist, S. Tolvanen, I. MIettinen, A. Fallarero, and J. Peltonen, 'In-depth exploration of the impact of surface properties and biofilm formation assays on Staphylococcus aureus biofilms', *Biomater. Submitt.*.
[241] E. Rosqvist *et al.*, 'A low-cost paper-based platform for fast and reliable screening of cellular interactions with materials', *J Mater Chem B*, vol. 8, no. 6, pp. 1146–1156, 2020, doi: 10.1039/C9TB01958H.
[242] 'Microplate Dimensions, Working Volumes and Packaging | Application Support Knowledgebase | Lab Products & Services', *PerkinElmer*. https://www.perkinelmer.com/uk/lab-products-and-services/application-support-knowledgebase/microplates/plate-dimensions.html (accessed Dec. 17, 2020).
[243] S. H. Kim and J. H. Kim, 'Lethal effect of adriamycin on the division cycle of HeLa cells.', *Cancer Res.*, vol. 32, no. 2, pp. 323–325, Feb. 1972.
[244] N.-T. Chen *et al.*, 'Probing the dynamics of doxorubicin-DNA intercalation during the initial activation of apoptosis by fluorescence lifetime imaging microscopy (FLIM).', *PloS One*, vol. 7, no. 9, p. e44947, 2012, doi: 10.1371/journal.pone.0044947.
[245] T. Sasaki, K. C. Holeyfield, and J. Uitto, 'Doxorubicin-induced inhibition of prolyl hydroxylation during collagen biosynthesis in human skin fibroblast cultures. Relevance to imparied wound healing.', *J. Clin. Invest.*, vol. 80, no. 6, pp. 1735–1741, Dec. 1987, doi: 10.1172/JCI113265.
[246] J. Shen, L. Li, T. Yang, P. S. Cohen, and G. Sun, 'Biphasic Mathematical Model of Cell-Drug Interaction That Separates Target-Specific and Off-Target Inhibition and Suggests Potent Targeted Drug Combinations for Multi-Driver Colorectal Cancer Cells.', *Cancers*, vol. 12, no. 2, Feb. 2020, doi: 10.3390/cancers12020436.
[247] A. Catheline, F. Paolucci, G. Valenti, P. Poulin, and A. Pénicaud, 'Transparent electrodes made from carbon nanotube polyelectrolytes and application to acidic environments', *J. Mater. Res.*, vol. 30, no. 13, pp. 2009–2017, 2015, doi: 10.1557/jmr.2015.166.
[248] C. K. Choi, C. Margraves, S. Jun, A. English, P. Rack, and K. Kihm, 'Opto-Electric Cellular Biosensor Using Optically Transparent Indium Tin Oxide (ITO) Electrodes', *Sensors*, vol. 8, May 2008, doi: 10.3390/s8053257.
[249] R. C. Nordberg, J. Zhang, E. H. Griffith, M. W. Frank, B. Starly, and E. G. Loboa, 'Electrical Cell-Substrate Impedance Spectroscopy Can Monitor Age-Grouped Human Adipose Stem Cell Variability During Osteogenic Differentiation', *Stem Cells Transl. Med.*, vol. 6, no. 2, pp. 502–511, Feb. 2017, doi: 10.5966/sctm.2015-0404.
[250] I. O. K'Owino and O. A. Sadik, 'Impedance Spectroscopy: A Powerful Tool for Rapid Biomolecular Screening and Cell Culture Monitoring', *Electroanalysis*, vol. 17, no. 23, pp. 2101–2113, 2005, doi: https://doi.org/10.1002/elan.200503371.
[251] Y. Wei *et al.*, 'Embedded silver PDMS electrodes for single cell electrical impedance spectroscopy', *J. Micromechanics Microengineering*, vol. 26, no. 9, p. 095006, Jul. 2016, doi: 10.1088/0960-1317/26/9/095006.
[252] G. Kang, Y. Kim, H.-S. Moon, J. Lee, T.-K. Yoo, and K. Park, 'Discrimination between the human prostate normal cell and cancer cell by using a novel electrical impedance spectroscopy controlling the cross-sectional area of a microfluidic channel.', *Biomicrofluidics*, vol. 7 4, p. 44126, 2013.
[253] M. P. Walzik *et al.*, 'A portable low-cost long-term live-cell imaging platform for biomedical research and education', *Biosens. Bioelectron.*, vol. 64, pp. 639–649, 2015, doi: https://doi.org/10.1016/j.bios.2014.09.061.
[254] PubChem, 'Doxorubicin Hydrochloride'. https://pubchem.ncbi.nlm.nih.gov/compound/443939 (accessed Dec. 18, 2020).

ISBN 978-952-12-4122-2